Materials Science & Engineering R 147 (2022) 100645

Contents lists available at ScienceDirect

Materials Science & Engineering R

journal homepage: www.elsevier.com/locate/mser

Machine-learning and high-throughput studies for high-entropy materials

E-Wen Huang [a,b,c,1,*], Wen-Jay Lee [d,e,1,**], Sudhanshu Shekhar Singh [f,1,**], Poresh Kumar [f], Chih-Yu Lee [d], Tu-Ngoc Lam [a,b,c,g], Hsu-Hsuan Chin [a,b,c], Bi-Hsuan Lin [h], Peter K. Liaw [i,**]

[a] Department of Materials Science and Engineering, National Yang Ming Chiao Tung University, Hsinchu, Taiwan, 30010, Taiwan
[b] Department of Materials Science & Engineering, National Chiao Tung University, Hsinchu City, 30010, Taiwan
[c] High Entropy Materials Center, National Tsing Hua University, Hsinchu City, 30013, Taiwan
[d] National Center for High-Performance Computing, Taichung City, 40763, Taiwan
[e] Department of Physics, National ChungHsing University, Taichung City, 40227, Taiwan
[f] Department of Materials Science and Engineering, Indian Institute of Technology, Kanpur, 208016, India
[g] Department of Physics, College of Education, Can Tho University, Can Tho City, 900000, Viet Nam
[h] National Synchrotron Radiation Research Center, Hsinchu, 30076, Taiwan
[i] Department of Materials Science & Engineering, The University of Tennessee, Knoxville, 37996-2100, USA

Abbreviations: HEMs, high-entropy materials; HT, high-throughput; ML, machine learning; HEAs, high-entropy alloys; MPEAs, multi-principal element alloys; HECs, high-entropy ceramics; HEOs, high-entropy oxides; ESO, entropy-stabilized oxide; HEAAs, high-entropy amorphous alloys; HEAACs, high-entropy amorphous alloys composites; AI, artificial intelligence; MGI, materials genome initiative; ICME, integrated computational materials engineering; VAC, virtual aluminum castings; CAE, computer-aided engineering; MD, molecular dynamics; CPFEM, crystal plasticity finite element method; FEM, finite element method; ANN, artificial neural network; NN, neural network; GB-Trees, gradient boosting trees; ND, neutron-diffraction; SQS, special quasi-random structure; CPA, coherent potential approximation; DFT, density-functional theory; GBMs, gradient boosting machines; MSE, mean squared error; RF, random forests; K, bulk modulus; G, shear modulus; VEC, valence electron concentration; CALPHAD, calculation of phase diagrams; PSPP, processing-structure-property-performance; SVM, support vector machine; KNN, k-nearest neighbor; KRR, kernel ridge regression; RFR, random forest regression; GBR, gradient boosting regression; GPR, gaussian process regression; GPs, gaussian processes; SMAs, shape-memory alloys; RNN, radius-nearest neighbors; LAEs, local atomic environments; XRD, X-ray powder diffraction; XRF, X-ray fluorescence; HCA, hierarchical cluster analysis; HTVS, HT virtual screening; GLMNET, generalized linear regression; LDA, linear discriminant; DT, decision tree; RF, random tree/forest; KPCA, kernel principal component analysis; EMTP-CPA, exact muffin-tin orbitals formalism-coherent potential approximation; VASP, vienna Ab initio simulation package; GA, genetic algorithm; GMs, generative models; CGAN, conditional generative adversarial network; VAE, variational autoencoder; CVAE, conditional variational autoencoder; AFLOW, automatic-flow; MAST, materials simulation toolkit; MC, Monte Carlo; BPNNPs, Behler-Parrinello neural network potentials; MTPs, moment tensor potentials; SNAPs, spectral neighbor analysis potentials; DLPs, deep learning potentials; GAPs, gaussian approximation potentials; LRPs, low-rank potentials; FCC, face-centered-cubic; BCC, body-centered cubic; ATAT, alloy theoretic automated toolkit; 1D, one-dimensional; 2D, two-dimensional; 3D, three-dimensional; SSRL, stanford synchrotron radiation lightsource; XND, X-ray nanodiffraction; TPS, Taiwan Photon Source; HTEM, high-throughput experimental materials; DLHub, data and learning hub for science; API, application programming interfaces; MIT, Massachusetts Institute of Technology; MDF, materials data facility; NREL, National Renewable Energy Laboratory; SS+IM, solid solution and intermetallic; MEAs, medium-entropy alloys; RMSE, root-mean-square error; OM, optical microscopy; EBSD, electron backscatter diffraction; EDS, energy dispersive X-ray spectroscopy; SEM, scanning electron microscope; CCAs, compositionally complex alloys; TEM, transmission electron microscope; EAM, embedded atom method; MEAM, modified embedded atom method; VDRIVE, VULCAN data reduction and interactive visualization software; SNS, spallation neutron source; ORNL, Oak Ridge National Laboratory; JPARC, Japan Proton Accelerator Research Complex; SMARTS, spectrometer for materials research at temperature and stress; LANSCE, Los Alamos Neutron Science Center; RAL, Rutherford Appleton Laboratory; RSI, Residual Stress Instrument; HANARO, High-Flux Advanced Neutron Application Reactor; KAERI, Korea Atomic Energy Research Institute; XNP, X-ray nanoprobe; RHEA, refractory HEA; VPSC, viscoplastic self-consistent; GBM-Locfit, gradient boosting machine local polynomial regression; GSAS, general structure analysis system; MTP, moment tensor potential; YS, yield strength; UTS, ultimate tensile strength; CTE, coefficient of thermal expansion; CHT, combinatorial and high-throughput; MCE, magnetocaloric effect; SS, solid solution; IM, intermetallic; AM, amorphous; LTVC, Lederer-Toher-Vecchio-Curtarolo; HCP, hexagonal-close-packed; MLFFNN, multi-layer feed-forward NN; SRO, short-range order; CNN, convolutional neural network; LENS™, laser engineered net shaping; MMEC, maximum magnetic entropy change; HE-BMGs, high-entropy bulk metallic glasses; DSC, differential scanning calorimeter; STE, spin-driven thermoelectric; ICSD, inorganic crystallographic structure database; MPMS, magnetic properties measurement system; PPMS, physical property measurement system; EARS, effective atomic radii for strength; SSH, solid solution hardening; CCAA, canonical correlation analysis; SHAP, shapley additive explanation; FNN, fuzzy neural network; EHEAs, eutectic HEAs; SF, stacking fault; SFE, stacking fault energy; TRIP, transformation-induced plasticity; TWIP, twinning-induced plasticity; CMWP, convolutional multiple whole profile; DOE, Department of Energy; NEUP, Nuclear Energy University Program; XPS, X-ray photoelectron spectroscopy; SKPFM, scanning Kelvin probe force microscopy; SPS, spark plasma sintering.

* Corresponding author at: Department of Materials Science and Engineering, National Yang Ming Chiao Tung University, Hsinchu, Taiwan, 30010, Taiwan.
** Corresponding authors.
E-mail addresses: ewhuang@g2.nctu.edu.tw (E.-W. Huang), wjlee@narlabs.org.tw (W.-J. Lee), sudhanss@iitk.ac.in (S.S. Singh), pliaw@utk.edu (P.K. Liaw).
[1] These authors contributed equally to the present work and are joint first authors.

https://doi.org/10.1016/j.mser.2021.100645
Received 31 May 2021; Received in revised form 22 September 2021; Accepted 11 October 2021
Available online 15 January 2022

ARTICLE INFO

Keywords:
High-entropy materials
Complex concentrated alloys
Multi-principal-element alloy system
Machine learning
High-throughput
Combinatorial approach

ABSTRACT

The combination of multiple-principal element materials, known as high-entropy materials (HEMs), expands the multi-dimensional compositional space to gigantic stoichiometry. It is impossible to afford a holistic approach to explore each possibility. With the advance of the materials genome initiative and characterization technology, a high-throughput (HT) approach is more reasonable, especially to identify the specified functions for the new HEMs development. There are three major components for the HT approach, which are the computational tools, experimental tools, and digital data. This article reviews both the materials informatics and experimental approaches for the HT methods. Applications of these tools on composition-varying samples can be used to obtain stoichiometry effectively and phase-structure-property relationships efficiently for the materials-property database establishment. They can also be used in conjunction with machine learning (ML) to improve the predictability of models. These ML tools will be an essential part of HT approaches to develop the new HEMs. The ML-developed HEMs together with ML-created other materials are positioned in this manuscript for future HEMs advancement. Comparing all the reviewed properties, the hierarchical microstructures together with the heterogeneous grain sizes show the highest potential to apply ML for new HEMs, which needs HT validations to accelerate the development. The promising potential and the database from the HEMs exploration would shed light on the future of humanity building from the scratch of Mars regolith.

1. Introduction

Since the late 1970s/early 1980s, Prof. Cantor and Prof. Yeh individually broke through the traditional boundaries of the principal-element concept and invented the high-entropy alloys (HEAs), also known as the multi-principal element alloys (MPEAs) [1] and the complex concentrated alloys [2]. With the development of advanced metallurgy, materials scientists create much greater dimensions for this new class of materials [3,4]. Besides the metallic systems, there are also high-entropy ceramics (HECs). The concept of entropy stabilization allows HECs as an ideal platform to study the role of mass and interatomic force disorder beyond what has been previously accessible. Since the conception of these ceramics, high-entropy oxides (HEOs) exhibited great capabilities for superionic mobility and thermochemical water splitting [5] as well other new opportunities [6]. For example, Musicó et al. summarized the emergent fields of HEOs, which included optical properties [7]. The luminescent high-entropy materials (HEMs) can be quite different from the traditional luminescent materials. For the luminescent HEMs, slightly different compositions may yield quite changes in properties. Therefore, from the perspective of optical properties, luminescent HEMs can be tunable for their light-emitting wavelengths, such as Chen and Wu's transparent high-entropy fluoride laser ceramics [8]. The HEMs with optical properties included (Ce,Gd,La,Nd,Pr,Sm,Y)$O_{2-\delta}$, (Ce,La,Nd,Pr,Sm,Y)$O_{2-\delta}$, (Ce,La,Pr,Sm,Y)$O_{2-\delta}$, (Ce,La,Pr,Y)$O_{2-\delta}$, (Ce,La,Pr,Sm)$O_{2-\delta}$, (Ce,La,Pr)$O_{2-\delta}$, (Ce,Pr)$O_{2-\delta}$, (Ce,Gd,La,Nd,Pr,Sm,Y)$O_{2-\delta}$, (Ce,La,Nd,Pr,Sm,Y)$O_{2-\delta}$, and (Ce,La,Pr,Sm,Y)$O_{2-\delta}$ in their crystal structures [9] and (La, Ti, Nb, W, Zr)O in amorphous-glass structure [10]. In addition, the HEMs with luminescent characteristics can be tailored by varying the elemental composition to achieve the tunability of light emission. Hence, measuring the light-emission behavior of the material, discussing the relationship between the electron-electron pair in the energy band, and considering the relationship between the material structure and composition are also an important part of studying optical properties. The HEOs show potential applications in energy storage and catalysis. Djenadic et al. indicated a crystalline single-phase oxide of $Mg_{0.2}Co_{0.2}Ni_{0.2}Cu_{0.2}Zn_{0.2}O$ as an entropy-stabilized oxide (ESO) [11]. Other "entropy-stabilized" materials include high-entropy metal diborides, high-entropy carbides, high-entropy sulfides, high-entropy fluorides, and high-entropy alumino silicides [7]. Besides inorganic materials, Zhang et al. reported three-dimensional (3D) HEA-polymer composite nanolattices, which displayed exceptional strength-recoverability advantages [12]. For the amorphous structures, several high-entropy amorphous alloys (HEAAs) and high-entropy amorphous alloys composites (HEAACs) have been found for their promising applications as magnetic materials [13–15].

Although many components forming HEMs would not certainly guarantee better performance, the exploration of the multi-components materials beyond conventional binary, ternary, and dilute alloy open new opportunities [3]. Meanwhile, there are even more metastable HEAs rising exponentially with increasing the number of complexity and potential properties [16]. Prof. Cantor demonstrated an enormous number of potential HEMs can be 1 googol as 10^{100} [3], which was greater than the number of pharmacologically relevant molecules on the order of 10^{60} [17].

Traditionally, the research on structural materials is largely rooted in the enlightened empiricism of traditional metallurgy, the advent of artificial intelligence (AI), and the emergence of robust advanced characterizations, suggesting new engineering strategies in which the mechanism-based understanding is expected to discover new HEMs. However, it is impossible to carry out an Edisonian approach via trial-and-error examination of each stoichiometry. As summarized by Schmidt et al., machine learning (ML) is successfully employed for classification, regression, clustering, and dimensionality reduction tasks [18]. ML has revealed superior abilities in playing Go [19], self-driving cars [20], image and speech recognition classification, and even our daily email filtering [18]. Therefore, it is desirable to apply ML to materials research for the Pareto efficiency and surrogate model [18] similar to ML applications in the aforementioned fields.

As a result of the maturation of ML, it has become increasingly possible to identify a corpus of central results, which serves as the basis for the discovery and analysis of HEMs. To tackle the aforementioned challenges for HEMs, the Materials Genome Initiative (MGI) [21] showed promising progress to narrow the exploring dimensions by facilitating active learning in materials science with emphasis on the targeted design [22], which also inspires on-the-fly data acquisition [23]. The approach of ML as "active learning" is that the algorithm dynamically chooses the data from which it learns so that it can perform better over the long-run statistically [24]. The "learning on-the-fly" scheme offers a superior efficiency by reducing the number of calculations [25]. There are successful "learning on-the-fly" cases, such as using the neural network potential for Al-Mg-Si alloys development [26], creating the interatomic potential for zirconium [27], parametrizing interatomic potentials [28], and accelerating HT searches for new alloys [29]. The Integrated Computational Materials Engineering (ICME) [30], such as thermodynamics databases for materials design, has demonstrated the ability to accelerate the discovery and the development of new materials, namely the corrosion-resistant alloys developed by QuesTek, LLC, the low-rhenium alloys developed by GE, and the cast aluminum cylinder heads and engine blocks developed by the virtual aluminum castings (VAC) program of Ford [31]. For the manufacturing,

the VAC program successfully combined a vast knowledge base of the cast aluminum research with readily available computer-aided engineering (CAE) tools to design, cast, heat treat, and test specific aspects of vehicle parts working together simultaneously.

Meanwhile, data is the key to ML. Hence, the HT research plays a significant role in ML. In November 2020, the Division on Engineering and Physical Sciences of the National Academy of Engineering sponsored the online workshop "High Throughput Research: Accelerating Materials Discovery, Design, Development and Deployment" to review the applications of AI and big data analytics coupled with advanced sensing, measurement, visualization, and process-control hardware. During the workshop, Prof. Flores used the concept of alloy design space to illustrate how to facilitate the HT methods to position the targeted alloy and manipulate the database in effectively shortening the distance between the target and the simulated models [32]. Miracle et al. reported a new characterization strategy, which suggests to reject the largest number of alloys with the smallest effort first and separate into computations, structure-insensitive, and structure-sensitive evaluations [33].

Research on HEMs as a dynamic topic has emerged as one of the promising directions for their engineering applications [4,34,35]. The challenges regarding the applications always imply demands, which must be new classes of advanced properties. For the specified challenge, ML [36] can accelerate the development of HEMs, such as HECs [37] and HEMs [38,39]. These approaches specified that ML can accelerate the specified materials discovery [40–42], such as phase predictions [43–45]. In Schmidt et al.'s work, ML performs better than traditional molecular dynamics (MD) for phase predictions [18]. The number of published works from January 2000 to April 2021 on "machine learning" and "machine learning + high entropy alloys" is shown in Fig. 1.

To hasten the design of HEMs, several criteria were proposed [46], such as the ML-informed prediction [47], HT design [48], and entropy descriptors [49]. Besides these mechanistic-understanding-based parameters and supervised ML, Tshitoyan et al. has recently indicated an unsupervised text mining from 3.3 million materials science literature between 1922 and 2018 in materials discovery [50]. They unveiled the previously-unrecognized properties of existing materials, which could then be repurposed [50]. Tshitoyan et al.'s methods can sort the overwhelming published text, which is difficult to analyze by traditional approaches. This unsupervised method may shed light to text mining the reported properties in the literature.

Moreover, increasingly complex HEMs engendered the emergence of methods built around the explicit consideration of multiple properties simultaneously. As a result of these new challenges, this review attempts to summarize the present capacities of ML and HT combinatorial approaches, such as thin-film materials libraries [51], diffusion database [52], and X-ray diffraction datasets [53] for HEMs discoveries and developments. For example, we compare how many papers reporting either "high entropy effects" or "ML" on specific materials. Following Tshitoyan et al.'s report [50], we select piezoelectric, superconductors, thermoelectrics, intermetallics, photovotaics, organic compounds, quantum heterostructure, and battery materials for comparison purposes, as depicted in Fig. 2.

In Fig. 2, the sizes of the circles are in proportion to the number of publications. For each material type, the darker and the lighter circles indicate the numbers of papers using ML and high entropy concepts, respectively. As shown in Table 1, for the piezoelectric research, most researchers apply ML. For the superconductors and intermetallics, there are more people applying the high entropy concepts. On the other hand, for the thermoelectrics and battery materials, there are more researchers using ML. Meanwhile, for the quantum heterostructures materials, photovotaics, and organic compounds, the number of publications with high entropy concepts is much less than that with ML.

The review is hence divided into three parts. It starts with an overview of the applications of ML for HEMs development, including AI, atomic potentials, and big-data approaches. The argument made here is that there are already many measured properties summarized in the review articles and web-based database [60], but for model fitting and simulation, it is also necessary to recap a priori assumption of theoretical calculations. For example, DeCost et al.'s reflections [61] read "*current applications of AI in materials science focus more on solving engineering and design problems*". Others also note that a major criticism of ML techniques is that "*black-box algorithms*" do not always provide "*new physical laws*" [18]. Some AI applications in materials science report the "black-box-like" optimization. To realize the full potential of AI in helping the materials community, Lipton's criteria to examine the interpretability of the ML are listed as (1) *simulatability, decomposability*, (2) *algorithmic transparency*, (3) *text explanations*, (4) *visualization*, and (5) *local explanations* [62]. Along this direction, his manuscript reviewed the selected HT examination cases for HEMs, which may not include all the five criteria for the interpretability but follow at least few. This

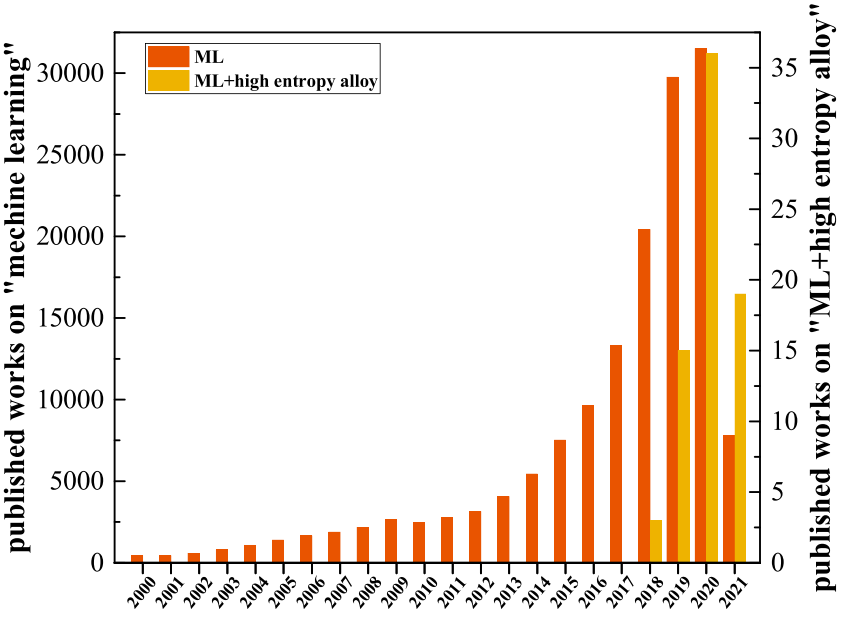

Fig. 1. Number of published works on "machine learning" and "machine learning + high-entropy alloys" (from January 2000 to April 2021).

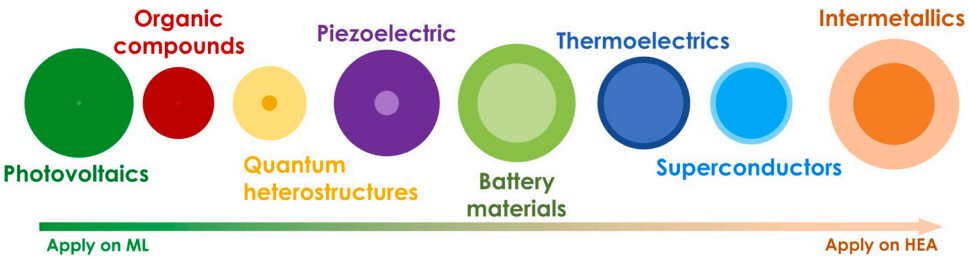

Fig. 2. The eight materials from Tshitoyan et al.'s unsupervised text mining [50] (Adapted from Fig. 1 in Tshitoyan et al.'s paper [50]). The sizes of the circles are proportional to the number of published works on "machine learning + one of the eight materials" and "high entropy + one of the eight materials" described in the darker color and lighter color, respectively (from January 2000 to April 2021).

Table 1
Summary of the piezoelectric, superconductors, thermoelectrics, intermetallics, photovotaics, organic compounds, quantum heterostructure, and battery materials with the keywords of either "machine learning" or "high entropy" searched from the Web of Science and their corresponding numbers of the references (from January 2000 to April 2021).

Materials	Numbers of the references	Keywords
Piezoelectric	126	Machine learning and Piezoelectric
	3, [54-56]	High entropy and Piezoelectric
Superconductors	37	Machine learning and Superconductors
	32	High entropy and Superconductors
Battery materials	216	Machine learning and Battery materials /Energy storage
	36	High entropy and Battery materials /Energy storage
Thermoelectrics	70	Machine learning and Thermoelectrics
	37	High entropy and Thermoelectrics
Photovoltaics	140	Machine learning and Photovoltaics
	1, [57]	High entropy and Photovoltaics
Organic compounds	26	Machine learning and Organic compounds
	1, [58]	High entropy and Organic compounds
Quantum heterostructures	24	Machine learning and Quantum heterostructures /Quantum materials
	1, [59]	High entropy and Quantum heterostructures /Quantum materials
Intermetallics	41	Machine learning and Intermetallics
	381	High entropy and Intermetallics

manuscript also summarized some potential experimental approaches for future ML and HT examinations for the HEMs combinatorial research.

Finally, recalling Raabe et al.'s report on the impact and technology readiness of sustainability measured for structural alloys [63], corrosion protection is pointed out as the high potential for impacts on the sustainability of structural metals. In this manuscript, we review the corrosion properties of HEAs, which ML and HT examinations are rarely applied yet. We put the review of the corrosion as the final part, which the authors believe would be the future directions and challenges for HEMs. This part will also be a culmination of great efforts set forth in the preceding sessions with the aim being that the metallurgists and materials scientists attempt to consider potential applications for the HEMs discoveries and developments through ML and HT methodologies.

Yet, together with the scientists' voyage, the future of humanity on Mars would not just be science movies. The resource of Mars could offer much potential for supporting the robotics' activities. Meanwhile, it will fall to design, civil, and space engineers to ensure that the trips to Mars and the buildings using Mars' elements by additive manufacturing are safe and realistic [64]. Hence, in the summary, we review the current materials and potential HEMs for the high-temperature applications and the oxidation because the materials for the vehicles to Mars and the additive manufacturing on Mars can induce high-heat-flux heating and cause high temperatures. What we learned from the HT examination and ML for the fabrications will enable the selection of the mining and additive manufacturing HEMs on Mars.

2. Machine learning

Although ML is being extensively applied to facilitate problem solving of materials research, there are considerable challenges in efficiently exploring such a vast ML domain knowledge for a metallurgist. Specifically, there are numerous ML terminologies that a non-specialist is not familiar with. In this session, before explaining various ML techniques, which are relatively new and quite complex, the review will start with the classical metallurgy topics evolving with ML to bridge the gap between the science experiments and ML review session.

According to Meredig's summary, there are five major high-impact research areas in ML for materials science, which are summarized below [65]: (1) *Training models to predict materials properties and the validation by experiments and/or physics simulation*; (2) *ML methods development for descriptors, multi-property optimization* [66], *extrapolation detection* [67], and *uncertainty quantification* [68]; (3) *High-throughput data acquisition*; (4) *ML to accelerate or simplify materials characterization which advances the current protocols and algorithms*; and (5) *Integration of physics and physics-based simulations within ML*. In the following sessions,

when ML methods are introduced, the associated impacts will be also mentioned.

Herein, two exemplary metallurgy topics evolving with ML trends and successfully developed are introduced, which are the crystal plasticity finite element method (CPFEM) and the elasticity, respectively.

For the crystal plasticity, it was written in the textbook that Taylor quantitatively described the models of crystallographic systems [69]. In 1972, Hill and Rice constructed a general time-independent constitutive model for the crystallographic shearing, which allows a general finite deformation elastic–plastic framework for analyzing single crystals [70]. In 1982, Peirce et al. numerically formulated the deformations of ductile single crystals subjected to tensile loading [71]. Peirce et al. successfully modeled an elastic-plastic relation based on Schmid's law. They considered lattice rotations for the non-uniform and localized deformations. They included self-hardening and latent hardening of the slip systems and compared the resolved shear stress vs. shear strain of the experimental points and their simulation profiles, which are both nonlinear [71]. In summary, without ML, there were already successful models quantitatively describing the nonlinear behavior of the crystal plasticity [70]. Meanwhile, the finite element method (FEM) enables modeling in smaller parts and constructs into a larger mesh of the objects and equations that models the entire system. Khan et al. clearly reviewed the history of the combining crystal plasticity with FEM as the CPFEM [72]. In 2015, without ML, Khan et al. demonstrated that how the CPFEM predicts finite plastic deformation of single crystalline metals over a wide strain rate range. Khan et al. commented that "*as the complexity of models increases, the number of parameters that need to be identified also increases, and it is usually more difficult to perform the numerical simulations*".

To deal with the increasing models, equations, and the number of parameters, Ali et al. explained why they selected the artificial neural network (ANN), which is one group of the algorithms used for ML in their CPFEM work on the AA6063-T6 aluminum alloys [73]. The idea of neural network (NN) is inspired by the biological neuron, where neurons are connected to each other in the network. Each neuron receives an input from all the neurons in the previous layer with weights and sends its output to every neuron in the next layer. The positive and negative weights reflect the excitatory and inhibitory connections, respectively. Similar to the accumulated experiences, the NN with different layers can adapt from the inputs and outputs, which is able to model the activities and predict the behaviors. Like the biological neural network learning knowledge, the ANN frameworks process the data to attain the required objective but use mathematical models instead. Moreover, beyond the training experiences, there are more sophisticated layer to layer filtration processes for the ANN.

Although the leading studies have constructed comprehensive models of the CPFEM, the key challenge is the balance between the accuracy and computational efficiency, where the computational cost-effectiveness decreases as the complexity of microstructure increases [74]. Before implementing ML, the experimental data are typically used to back-fit the constitutive model of the investigated systems. For the crystal plasticity, the microscopic material parameters in the formulas are considered to solve the constitutive model for connecting the macroscopic performances, such as the stress-strain curves, and the microscopic mechanisms, such as the textures. Ali et al. applied the typical crystal plasticity simulations, which can successfully forecast the experimental stress-strain and texture data. The results from the crystal plasticity simulations were used to train the ANN models in predicting the real material behavior. Moreover, the ANN has huge computational improvements over conventional simulation tools because the ANN models can be trained and validated. With the accumulated "experiences", the ANN models forecast the data without computationally expensive simulations. Hence, the ANN models take much less time compared to their counterparts, which are the traditional numerical simulations [73]. For the HEAs, Gao et al.'s took a step forward to apply the ANN to their CPFEM in the NiCoCrFe system [75]. Similar to Ali et al., Gao et al. also employed the CPFEM method based on their experimental data and physical mechanisms to provide the data set for training ML. Comparing with the experimental data, the CPFEM provides a huge amount of data for Gao et al.'s ANN models. Meanwhile, solving the nonlinear and multivariable problems are the major advantages of the ANN. Gao et al.'s extended the multi-level CPFEM framework coupled with an improved ANN algorithm, which is one of the successful cases of ML. From this case, the terminology of the ANN is briefly introduced. In summary, recalling Meredig's summary [65], Gao et al.'s training models with the benchmark data were validated by experiments and physics simulation. With different experimental data as the multi-property inputs, Gao et al.'s ML accelerated the high-throughput data acquisition. With the integrated physics-based simulations within ML, Gao et al. demonstrated the benefits of ML in investigating the plasticity of the NiCoCrFe HEAs [75].

Another terminology of ML, gradient boosting trees (GB-Trees) algorithm, is introduced here for the lattice elasticity study. For the HEAs, due to its complexity of the neighboring elements, the application of the Vegards' law may not be taken for granted [76]. Using *in-situ* neutron-diffraction (ND) characterizations can measure the lattice elasticity [77] while first-principles calculations can estimate the interatomic distance distributions from calculations of optimized special quasi-random structure (SQS) [78]. However, it is not trivial to measure each HEA system using ND. For the first-principles calculations, it will consume considerable computational time, especially for the complex systems. Coherent potential approximation (CPA) is another option for this research by estimating how sound waves scatter in a material, which might picture the spatial inhomogeneity of the modeling systems. However, several reports showed that CPA may not be able to model well the HEAs, such as the charge transfer between atoms. This gap can lead to deviations in quantifying the interatomic bonding [78]. Kim et al. compared the CPA, SQS, and ML models and found that both the CPA and SQS models without the atomic position relaxation can result in overestimating elastic-constant values [78]. On the other hand, Kim et al. applied the GB-Trees algorithm of MLs and found that ML models accurately forecasted the elastic properties of the HEAs and suggested the tunability of elastic properties in the HEAs [78].

Their methods are cited frequently. Here are few selected citations to recommend why Kim et al.'s ML methods have advantages. For example, Roy and Balasubramanian highlighted Kim et al.'s ML approaches because Kim et al.'s data used in ML was derived from density-functional theory (DFT) calculations, where a high quality of numerous DFT dataset enhances the phase and mechanical property predictions [79]. Moreover, using the data from the Materials Project database [80] also takes the advantage for their accuracy, which was due to the accumulated previous work. Kim et al.'s did not need to obtain the data from the scratch so that their approach demonstrated a relative economic path for data generation without time and resource on physical experiments [79]. Specifically, Chen et al.'s ML recommended Kim et al.'s ML approaches; the citation reads, "*the authors built a GB Tree–based predictive model using a separate set of nearly* 7000 *ordered, crystalline solids from the Materials Project, in which the elastic constants have already been properly labeled. It is worth mentioning that the training set and validation set do not contain any high-entropy alloys* [81]".

Now, let's take a closer look at Kim et al.'s ML method, which is the GB-Trees algorithm, one of the ML techniques. From Natekin and Knoll's tutorial, gradient boosting machines (GBMs) are known for their highly customizable to the particular needs of the application [82]. Using the GBMs, the ML procedure consecutively fits the models to provide a more accurate estimate of the response variable. In Natekin and Knoll's tutorial, the citation reads, "*The principal idea behind this algorithm is to construct the new base-learners to be maximally correlated with the negative gradient of the loss function, associated with the whole ensemble. The loss functions applied can be arbitrary, but to give a better intuition, if the error function is the classic squared-error loss, the learning procedure would result in consecutive error-fitting. In general, the choice of the loss function is up to*

the researcher, with both a rich variety of loss functions derived so far and with the possibility of implementing one's own task-specific loss" [82].

The difference from the GBM and other ML methods is that the other ML, such as the NN based on an ensemble of models is relatively a "strong" model [82]. For example, the ANN can be further combined altogether. One typical example is the ANN introduced in the earlier session for Gao et al.'s CPFEM combining a bucket of models for particular learning tasks [75]. Here, for Kim et al.'s GBM [78], their GB-Trees algorithm relies on combining a large number of relatively weak simple models to obtain a stronger ensemble prediction [82]. The GBM merges several simple models, called "weak learner", into robust committee as a strong model using additive models for improving prediction accuracy and avoiding overfitting. The weak learner is defined as the one whose performance is at least slightly better than random chance, which can be any models, but the decision tree is usually selected. In general ML algorithms, gradient descent method is used to minimize the loss function for optimizing the model parameters. However, the GBM aims to optimize or train the weak learner for predicting the residual $h_m(x)$ (defined as negative gradient of loss function $-\frac{\partial Loss}{\partial y_i^p}$, where y_i^p is the prediction value). According to the task, the different loss function can be selected, but all of them must be differentiable for GBM. For example, logarithmic loss can be used for a classification problem while mean squared error (MSE) is the most commonly used for a regression problem. The algorithm starts by initializing the weak model h_0 with a first guess. At each training iteration, a weak learner is fitted to the current residual and added to the prior model to update the residual until the variance is minimized and a robust learner is achieved, which is the so-called forward stage-wise procedure. To minimize the overfitting, the contribution of each weak learner can be narrowed by multiplying a scaling factor for better prediction.

The random forests (RF) is another important ML model assembling many relatively-weak simple models to become a stronger prediction [83]. Read from Natekin and Knoll's tutorial, "*The common ensemble techniques like random forests rely on simple averaging of models in the ensemble. The family of boosting methods is based on a different, constructive strategy of ensemble formation. The main idea of boosting is to add new models to the ensemble sequentially. At each particular iteration, a new weak, base-learner model is trained with respect to the error of the whole ensemble learnt so far*" [82].

The decision tree is the nonlinear ML concept, which was used in Kim et al.'s GB-Trees algorithm. Decision trees are hierarchical models that aim to find a target value by asking the fewer if-else questions [84]. For example, the RF regressors are a combination of many regression trees. The predictivity of RF is from the diversity of the trees/branches. Each node on a tree splits the dataset once according to whether a specific parameter or a combination of them, is above or below a threshold value [85].

Similar to Kim et al.'s GBM applications for the HEAs elasticity research, Salvador et al. discovered low-modulus Ti-Nb-Zr alloys using ML and the first-principles calculations [84]. Salvador et al. first evaluated the predictive accuracies of linear regression and RF regressors. They optimized the RF models by searching for 50 different combinations of hyperparameters based on a random search algorithm. All their models used 80 % of the data as the training set to predict the unseen 20 %, where they successfully predicted the bulk modulus (K) and shear modulus (G) for the optimized Ti-Nb-Zr alloys [84]. Both Kim et al. [78] and Salvador et al. [84] employed the data from the Materials Project [80] with the aims of training predictive models for K and G based on compositional features. From this case, the terminology of the GBM is introduced. Meanwhile, recalling Meredig's summary [65], Kim et al. extracted materials data from the Materials Project database, which fed the data-hungry ML. Kim et al.'s ML extrapolation for the elasticity was also validated by the measured results for the HEAs [78].

In summary, the ML review session starts with the aforementioned two classical metallurgy topics to introduce the ANN and GBM of MLs for CPFEM and elasticity, respectively. These two examples are described more specifically to introduce the background and the applications of MLs for better understanding of the terminology. Followings are relatively general reviews on ML for HEMs.

2.1. Machine learning for HEMs

Because the HEMs have many compositional dimensions [86,87], the materials design is a great challenge. In the past, the metallurgists may apply an Edisonian approach using a single-element substitution method to explore different compositions under a specific alloy family [88–91]. However, exhaustive trial-and-error experiments consume too much time and resources. To solve the difficulty, the parametric and computational approaches are introduced. For example, deep neural networks [92] can be trained to perform fast and automated identifications of atomic/molecular types and positions as well as atomic defects [93]. Meanwhile, the challenges for ML are the interpretability and the physical understanding gained from ML models. One critical issue is that whether ML may replace other computational approaches, such as first-principle methods [18].

A parametric approach combines empirical rules and theoretical models to guide phase formation and stability as the microstructure is highly linked with materials properties [21,91,94–102]. The used parameters are generally based on the chemistry and topology nature. For example, the mixing enthalpy, ΔH_{mix}, and the atomic-size difference (polydispersity), δ, are two most widely used. Other design parameters are the mixing entropy, ΔS_{mix}, valence electron concentration (VEC), and electronegativity difference, $\Delta\chi$. Meanwhile, the calculation of phase diagrams (CALPHAD) [103–105] based on the existing experimental database, MD simulation [99,106], and first-principal method [107–109] are commonly utilized to predict and screen the HEMs. Yet, the approaches face some challenges due to their critical limitations on the oversimplification, high computation cost, insufficient reliability, and uncertainties. Some selected examples, which show the HEMs properties predicted by ML methods, are listed in Table 2.

In recent years, ML has garnered considerable attention since it can largely accelerate materials design in various areas, e.g., organic molecules, solid states, and HEAs. As materials science has become more and more data-centric, a vast amount of data generated from simulations and experiments can be included in training ML models. "Big data" opened up the fourth paradigms of materials science, which emphasizes the unlocking knowledge by data-driven techniques, e.g., predictive analytics, clustering, and relationship mining and generation [21]. Supported by the MGI [21], materials informatics has shaped the way how materials scientists uncover the processing-structure-property-performance (PSPP) relationships [148–150].

Table 2
Summary of some HEMs properties predicted by ML together with the associated methods and corresponding references.

Property	Ref.
Vibrational free energy and entropy	[110,111]
Lattice parameters	[112–115]
Thermal expansion coefficients	[112]
Anisotropic thermal expansions	[113]
Thermal conductivities	[112,115]
Anisotropic phonon thermal conductivities	[113]
Melting temperature	[116,117]
Curie temperature	[111]
Grain boundaries	[118,119]
Elastic properties, such as bulk and shear moduli	[111–114,120–123]
Lattice distortion	[111]
Electron density of states	[124,125]
Phase prediction	[44,102,115,123,126–137]
Formation energy	[111]
Magnetic properties	[138]
Stacking fault energy	[111,139–147]
Long-and short-range order	[111]

Table 3
ML algorithms for materials science applications.

Category	Methods	Target
Regression	ANNs GBM Gaussian process Kernel ridge Support vector machines (SVMs)	Aims to build the properties (i.e., mechanical, thermodynamic, electric, chemical properties, and other properties of material) of predictive models for predicting the properties of unknown materials and can be coupled with the optimization algorithm to realize the inversed material design (exploring new recipe). An overview of different properties that was predicted by ML have been reviewed in Ref. [18].
Classification	ANN Decision tree Kernel ridge k-nearest neighbors GBM SVMs embedding (t-SNE)	Separates the data points (categorical data) into several classes, which can be used in the phase prediction or type (3d-HEA, Refractory HEA, etc.) classification for HEAs.
Clustering	Hidden Markov model Hierarchical cluster k-means Modularity t-distributed stochastic neighbor	Mapping the material-data points into vectors for measuring the distances or similarities between materials themselves [68].

In general, there are two directions of materials design: the first is the prediction as the forward model, and the second is the discovery as the inverse model. In other words, ML can automatically identify the patterns and features of the high dimensional input data via statistical models to predict specific output, e.g., microstructures and properties. By interpolation and/or extrapolation, ML can also discover novel compositions via optimization algorithms or generative models in a target-oriented fashion. The advantage of ML is its time-saving and low-cost characteristics. However, since it is an extension of existing data, data accessibility, reliability, and processing are of concern.

To be more specific, ML can be classified into three categories, i.e., regression, classification, and clustering. For the HEAs, the regression models are usually applied for the continuous target output, such as hardness while classification models are used for the discontinuous output, such as phases or structures. Table 3 recaps the ML algorithms incorporated in materials science. Based on the training input, ML can also be classified into three types, i.e., supervised learning, semi-supervised learning, and unsupervised learning.

Nowadays, studies for HEMs widely exploit supervised learning while a few take unsupervised learning for dimension reduction as feature engineering to identify the key features. Semi-supervised learning falls between supervised and unsupervised learning. In this case, the algorithm is provided with both unlabeled as well as labeled data. It has been utilized in the molecular design [151]. It is particularly useful when available data are incomplete and to learn representations [152]. Since each algorithm has its own suitability and application scope, selection of a proper algorithm is crucial for its successful implementation. Among the aforementioned terminology summarized in Table 3, ANN and GBM are already introduced earlier. The other selected representative terminologies are introduced herein and categorized as supervised learning and unsupervised learning.

2.1.1. *Supervised learning*

As shown in Fig. 3, to predict the outputs and categorize the data, supervised learning uses labeled datasets to train algorithms. Prior to the learning process, the database construction is the first step. Once the data is obtained, a priori pre-processing is to prepare the data for model developments because the raw data may contain attributes from different units and scales. When the problem descriptions and the boundary conditions are clearly defined, ML is ready for learning [153].

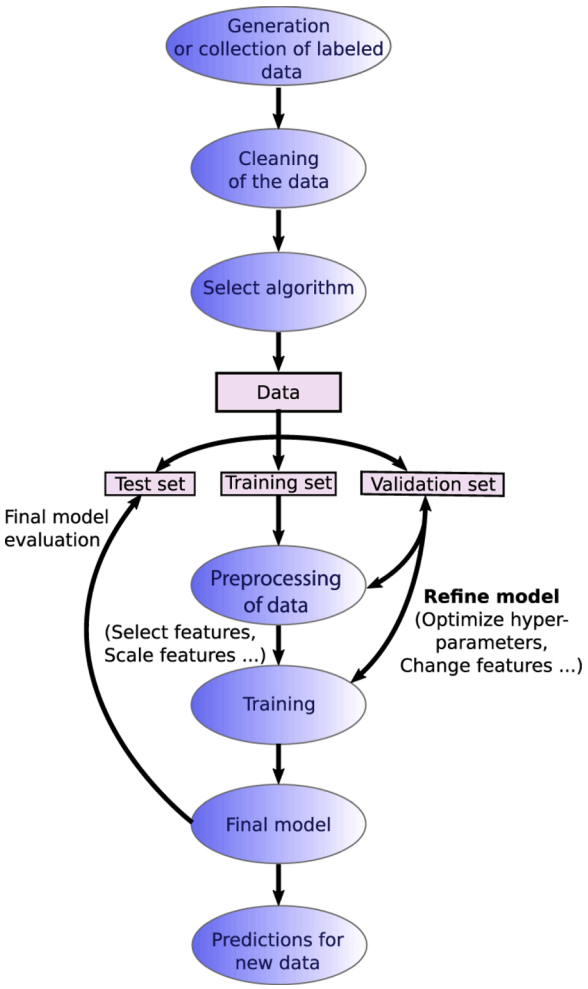

Fig. 3. Schmidt et al.'s supervised learning workflow. Adapted from [18] with permission from npj computational materials.

For the learning, regression is one of the supervised learning methods, where the labeled datasets are used to train algorithms in predicting outcomes accurately. Later, the input data will be fed into the model. The supervised ML adjusts its weights until the model can be cross validated. A support vector machine (SVM) [154] is a type of supervised learning method, and it can be used for both regression and classification tasks. Some of the common ML methods used for supervised learning include Naïve Bayes, k-nearest neighbor (KNN), decision trees, kernel ridge regression (KRR), random forest regression (RFR), gradient boosting regression (GBR), Gaussian process regression (GPR), SVM, and ANNs.

The main concept of SVM is to find a hyperplane of N-1 dimensions in an N-dimensional space which can distinctly categorize the data points. Meanwhile, the hyperplane with the maximum margin between data of different classes is chosen so that the selected hyperplane reinforces the future data points being classified correctly. The so-called support vectors are the distance between the hyperplane and the closet data points, which determines the position and orientation of the optimal hyperplane. For example, in Fig. 4, there are two groups of the data points marked as the solid and empty circles, respectively. Among the three lines, H_1, H_2, and H_3, H_3 can separate two sets of the data best as the margin is maximized. The support vectors are the lines in grey.

A linear hyperplane can be defined as the set of points that satisfy:

$$w^T x_i - b = 0 \quad (1)$$

where w is a normal vector to the hyperplane and b is the bias. If the data

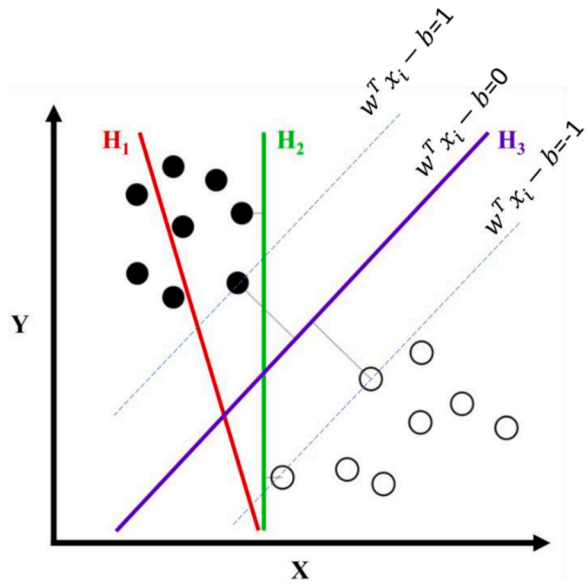

Fig. 4. H_1 cannot distinguish two sets of the data. H_2 can separate two sets of the data with a smaller margin. H_3 does separate two groups of the data with the maximum margin. (Adapted from the https://en.wikipedia.org/wiki/Support-vector_machine).

is linearly separable, we can define the margin by two parallel hyperplanes separating the two classes of data, which can be written:

$$y_i\left(w^T x_i - b\right) \geq 1 \quad \text{for} i = 1, \ldots, n \tag{2}$$

where $y_i = 1$ or -1 depending on whether the data is above or below the hyperplane, respectively. The margin can be maximized by minimizing $\|w\|$ subject to (2). The data is finally separated without misclassifications, which is so-call hard margin. If the data is not clearly separated or the margin is too small, the model would tend to overfit or be sensitive to outliers. Hence, the soft margin SVM could be helpful for better generalization. In soft margin SVM, the hinge loss function, as shown below, can be implemented to optimize the margin.

$$L(y) = \left[\frac{1}{n}\sum_{i=1}^{n} \max\left(0, 1 - y_i\left(w^T x_i - b\right)\right)\right] + \lambda\|w\|^2 \tag{3}$$

where λ is the extra regularization term to control the margin, x_i lies on the correct side of margin, y_i is the *i*-th target, and w is the normal vector to the hyperplane.

For the problems that are not linearly separable, SVM can make use of a feature transform technique called kernel tricks to solve a problem with more complex behaviors. The kernel functions implicitly map the data points into a high-dimensional feature space and make it possible to solve the problem with a nonlinear hyperplane. The most used kernels are polynomial and radial basis function. The GPR has been used to construct the foundation of ML algorithms. Gaussian processes (GPs) are natural generalizations of multivariate Gaussian random variables to infinite index sets [155]. GPR assumes that a Gaussian distribution best describes the statistical variance of the modeling data [156]. Being treated within a Bayesian framework, statistical methods can be implemented in the GP models. Hence, the GP models can validate the estimations of uncertainties in the predictions.

Liu et al. demonstrated how they apply the GPR to predict new NiTiHf shape-memory alloys (SMAs) and their performances in a high dimensional, multiple-target-property design space that considers chemistry, multi-step processing routes, and characterization methodology variations [157]. For GPR, the choice of covariance function is known as the relationship between observations. Liu et al. applied the GPR for their SMAs research because GPR can also estimate both the response and the variance in the response, which is better for extrapolation of the training data near the composition and processing domains.

Specifically, Liu et al. employed physics-informed nonlinear transformations of the process features time (t) and temperature (T), such as $\ln(t)$ and $T \times \left(1 - e^{-(T-\theta)}\right)^{-1}$ where θ is the critical temperature for a phase transformation enabling the GPR model to work well. Such physics-informed approaches are depicted from Liu et al. [157]. Liu et al. demonstrated that using GPR together with the physics-informed feature engineering enable the design of physical complex SMAs (Fig. 5).

Vasudevan et al. used the following example to explain the differences between the regression and classification for the supervised ML. "*When the property of interest (Y_i) is a numerical quantity, such as yield strength or melting point, then regression-based methods are well suited. On the other hand, when Y_i is a categorical quantity, such as space group of a crystalline material or crystal structure-type, then classification learning methods are better suited for supervised learning* [153]".

Kernel ridge regression (KRR) combines ridge regression and classification with the kernel trick. Ridge regression is used to estimate the coefficients of multi-regression models where independent variables are highly correlated and it is a biased estimation procedure that produces stable estimates of the coefficients [159]. Recalling Schmidt et al.'s "Recent advances and applications of machine learning in solid state materials science", ridge regression, a multi-dimensional least squares linear-fit problem is equivalent to solve the following minimization problem [18]:

$$\min_{\beta}\left(\|Y - X\beta\|_2^2 + \lambda\|\beta\|_2^2\right) \tag{4}$$

where X is the descriptor matrix, and Y is the outcome vector. β represents the vector of weighted coefficient. The λ parameter is the regularization penalty, which favors specific solutions with smaller coefficients. As complex regression problems can usually not be solved by a simple linear model, the kernel trick is often applied to ridge regression. A kernel first transformed the original descriptor into a higher-dimensional feature space $\phi(x)$. In this space, the kernel $k(x, y)$ is equal to the inner product $\langle\phi(x), \phi(y)\rangle$. In practice, only the kernel needs to be evaluated, avoiding an inefficient or even impossible explicit calculation of the features in the new space. After that, Schmidt et al. solved the minimization problem given by Eq. (4) in the new feature space which results in a non-linear regression in the original feature space. This is usually referred to as KRR. Fig. 6 is Shen et al.'s example

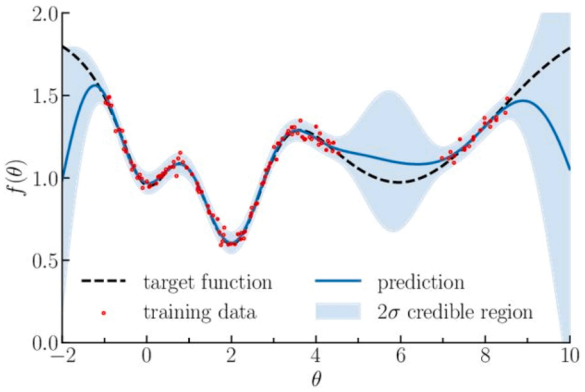

Fig. 5. Leclercq's illustration of GPR in one dimension, for the target test function (dashed line). Training data are acquired (red dots); they are subjected to a Gaussian observation noise with standard deviation $\sigma_n = 0.03$. The blue line shows the mean prediction μ(θ) of the GPR, and the shaded region of the corresponding 2σ(θ) uncertainty. GPs allow interpolating and extrapolating predictions in regions of parameter space where training data are absent [158]. Adapted from [158] with permission from American Physical Society (APS) (For interpretation of the references to colour in this figure legend, the reader is referred to the web version of this article.).

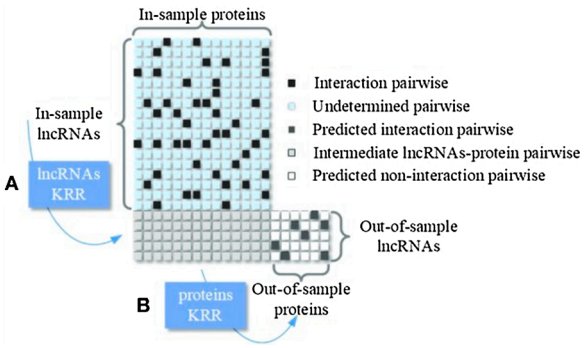

Fig. 6. Shen et al.'s illustration showing a schematic diagram of two-step KRR. (A) An intermediate prediction of LPI is conducted using an lncRNA KRR model. (B) Protein KRR is trained using the last step information for predicting new proteins. Adapted from [160] with permission from frontiers in Genetics.

showing multivariate information fusion with fast kernel learning to KRR in predicting LncRNA-Protein interactions [160].

K-nearest neighbors (KNN) [161] can be applied for both regression and classification problem. It forecasts the values of new data by measuring feature similarity. New data point is assigned to a value based on how close it resembles the points in the training set. The K in KNN indicates the number of neighbors, which the calculation will involve. A similar algorithm is radius-nearest neighbors (RNN) [162], which circles a group of neighbors according to the assigned neighbors. There are two steps in KNN: (1) *Calculating the distance between the new data point and each training data point where the commonly used distance functions are Euclidean, Manhattan and Hamming (for classification used)*. (2) *Selecting a K to involve the K closest neighbors and calculating the mean of the K neighbors*. The strength of KNN is the simplicity of its algorithm while it may be slow for large datasets compared with other regression models. Fig. 7 is Atallah et al.'s example showing intelligent feature selection with the modified K-nearest neighbor [163].

2.1.2. Unsupervised learning

The purpose of the unsupervised learning is to obtain the intrinsic relations within data. When dealing with high dimensional data, it is often useful to reduce dimensionality by projecting the data into a lower dimensional subspace to capture the essence of the data and to make the data visualized. This is called dimensionality reduction. It is a data preparation technique performed after data processing and before model training. In unsupervised learning, only input data is given to a model but no labeled output, which is tasked with a learning objective to find rankings or patterns clustering for this input. The representative methods include k-means [164,165], hierarchical cluster analysis [164], and Hidden Markov model [166]. In materials research, it enables the understanding of the similarities between materials themselves. Since each algorithm has its own suitability and application scope, the selection of a proper algorithm is crucial for its successful implementation.

K-means is a clustering method aiming to minimize the intra cluster distance as good grouping, indicating that each instance is close to the assigned cluster while apart from the nearest cluster [167] (Fig. 8).

K-means involves pre-assigned number of clusters and centroid that is the mean value of each cluster. Domain knowledge is important at the stage of determining the number of clusters. It begins with initial random guess of centroids and iteratively updates until the centroids do not change for best solutions. Given a set of data (x_1, x_2, …, x_n), each data has a d-dimension vector, k-means aims to build k clusters where

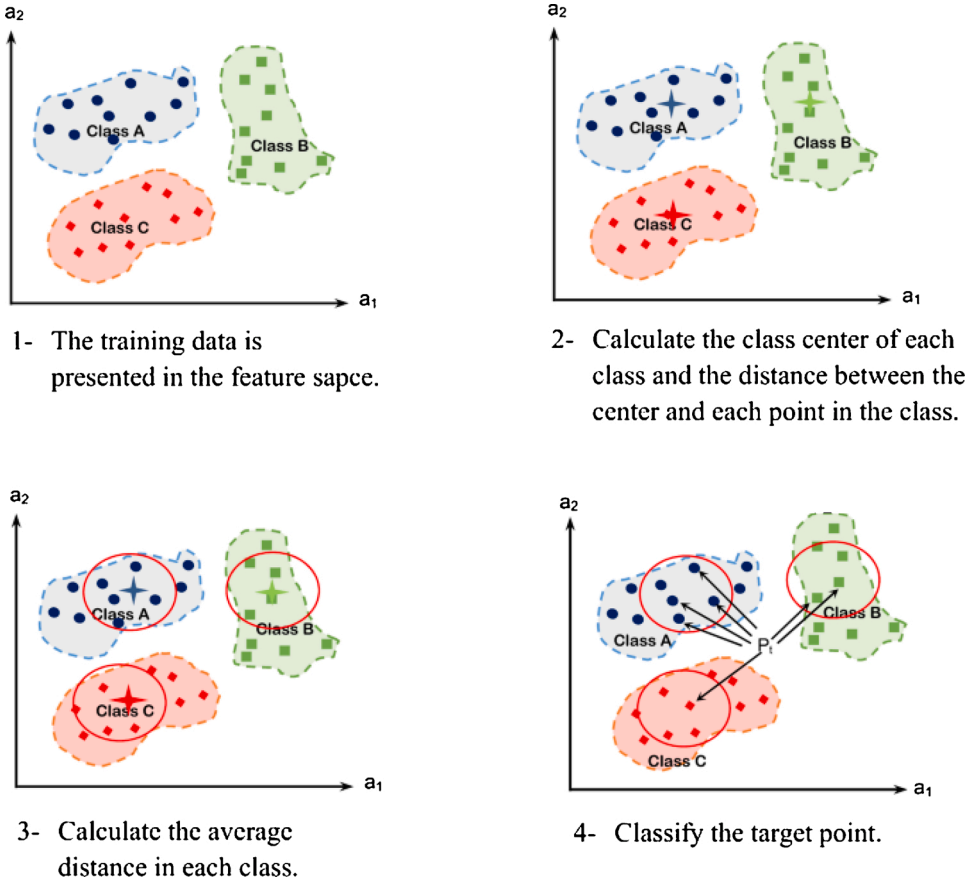

Fig. 7. Atallah et al.'s illustration showing steps of the proposed modified K-nearest neighbor [163]. Adapted from [163] with permission from Springer Nature.

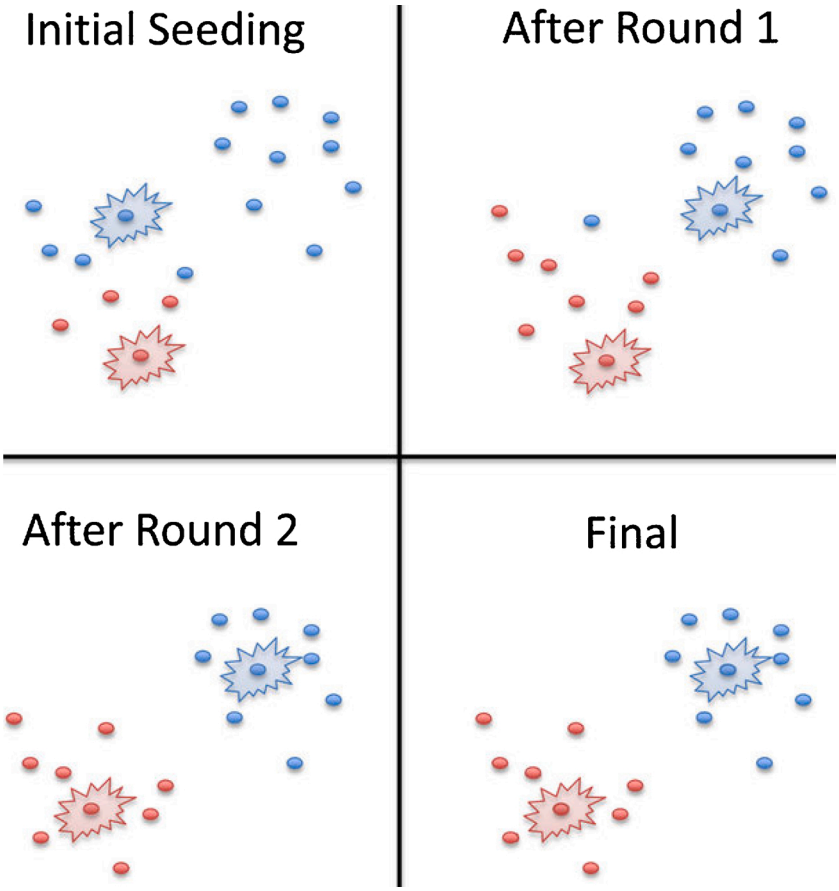

Fig. 8. Page's illustration showing K-means clustering algorithm. An example 2-cluster run is shown, with the clusters distinguished by color and the current cluster seeds marked by a starburst. In the first round, each point is assigned to its closest seed, and a new seed is chosen for each cluster based on the average of all points in that cluster. As a result, the blue cluster seed moves to the right side. In the second round, both cluster seeds drift to their correct locations, resulting in a proper division. Note that, after two rounds, the clusters have reached a steady-state, and would not change further through an infinite number of iterations. Adapted from [168] with permission from Springer Nature (For interpretation of the references to colour in this figure legend, the reader is referred to the web version of this article.).

the sum of the distances of the data to its centroid is minimized within each cluster S = (S_1, S_2, …, S_k). The objective function can be formulated:

$$J(\mu_i) = \sum_i^k \sum_{x_j \in S_i} \left\| x_j - \mu_i \right\|^2 \tag{5}$$

where x_j is referred to as the j-th data in the i-th cluster and μ_i is the centroid of the i-th cluster S_i. $\left\| x_j - \mu_i \right\|$ denotes the distance which can be either Euclidean distance or Manhattan distance. μ_i can be computed by following equation:

$$\mu_i = \frac{1}{|n_i|} \sum_{x_j \in S_i} x_j \tag{6}$$

where n_i represents the number of data points in the i-th cluster.

Hierarchical cluster is a pairwise approach that builds the cluster step by step. Through a dendrogram, the correlations among clusters can be visualized [169]. Observations are allocated to clusters by drawing a horizontal line through the dendrogram. Observations that are joined together below the line are in clusters. Fig. 9 is Fujii et al.'s example, which quantitatively predicts grain-boundary thermal conductivities from local atomic environments (LAEs) using hierarchical cluster [170].

There are two major types of hierarchical clustering algorithm: agglomerative hierarchical clustering and divisive hierarchical clustering. The former is a bottom-up strategy, assuming each object as an individual cluster and merging clusters that are close. Divisive hierarchical clustering starts with the whole dataset as a single cluster then separates the clusters step by step. Both strategies vary according to how the dissimilarity (distance) is measured, most of which are single linkage and complete linkage. Single and complete linkages were defined as the distances between the closest points and between the furthest points in the two groups, respectively. They are based on the following measurements where C_a and C_b are the two different clusters:

$$\text{Single linkage}: \quad d(C_a, C_b) = \min_{x_i \in C_a, x_j \in C_b} d(x_i, x_j) \tag{7}$$

$$\text{Complete linkage}: \quad d(C_a, C_b) = \max_{x_i \in C_a, x_j \in C_b} d(x_i, x_j) \tag{8}$$

It is obvious that different distance measurements can result in completely different results. Single linkage tends to depict chaining effect while complete linkage tends to be used in data with significant groups by comparing clusters with extreme similarity. Bortolotti et al. showed that combining X-ray powder diffraction (XRD) and X-ray fluorescence (XRF) with cluster analysis can automatically map the chemical and crystallographic surface [170]. Similarly, Torralba *et al.* performed a hierarchical cluster analysis (HCA) with complete linkage method based on their composition for determining whether some combinations of elements tend to be used in the HEAs consistently [171]. The dendrogram analysis reveals dissimilarity between different compositions of HEAs. It is found that the 9 types of clusters can apparently be divided into refractory metals and transition metals, where refractory metals have BCC phase structure and transition metals include BCC and FCC(+BCC), as shown in Fig. 10.

2.1.3. Machine learning methods for HEMs

The supervised learning is mostly mature for most ML studies in the physical sciences, which is a ML paradigm for acquiring the input (e.g., structure, composition, experiment conditions.)-output (e.g., properties, phases, structure, type, etc.) relationships from training a given set of input-output pairs and using the training model to produce optimal outputs for unseen inputs. As for the output data with continuous quantity, the regression methods, such as the KRR or GPR [172], ANNs

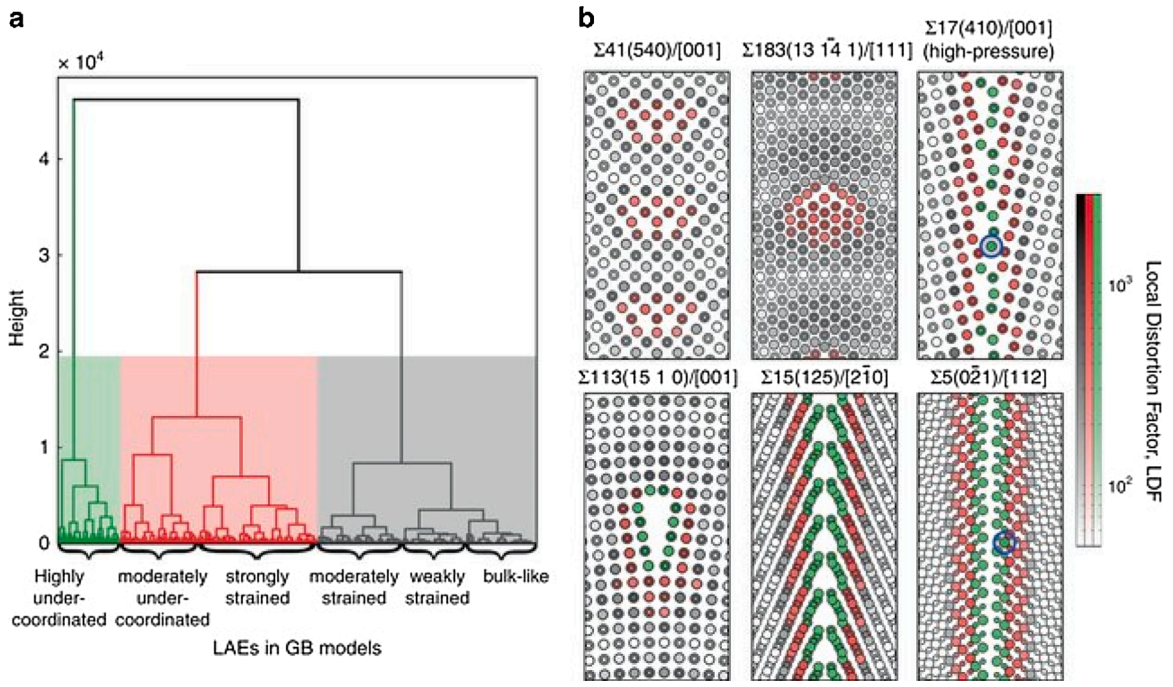

Fig. 9. Fujii et al.'s illustration showing hierarchical clustering of grain-boundary local atomic environments. (a) Hierarchical relationship between LAEs depicted in dendrogram form. The different regions represent three general groups of LAEs: (green) highly under-coordinated (bond-ruptured); (red) moderately under-coordinated or strongly strained; and (grey) moderately strained, weakly strained or bulk-like. (b) Representative distributions of the LAE groups and LDFs at six STGBs. A log scale is used to make it easier to distinguish changes in LDFs within LAE groups. Adapted from [170] with permission from Springer Nature (For interpretation of the references to colour in this figure legend, the reader is referred to the web version of this article.).

[173], and SVMs [174], are widely used. If the target is the discrete output, such as the type of material phase, ANNs, decision tree [175], k-nearest neighbors, and random-forest [176] algorithms are the commonly used classification algorithms.

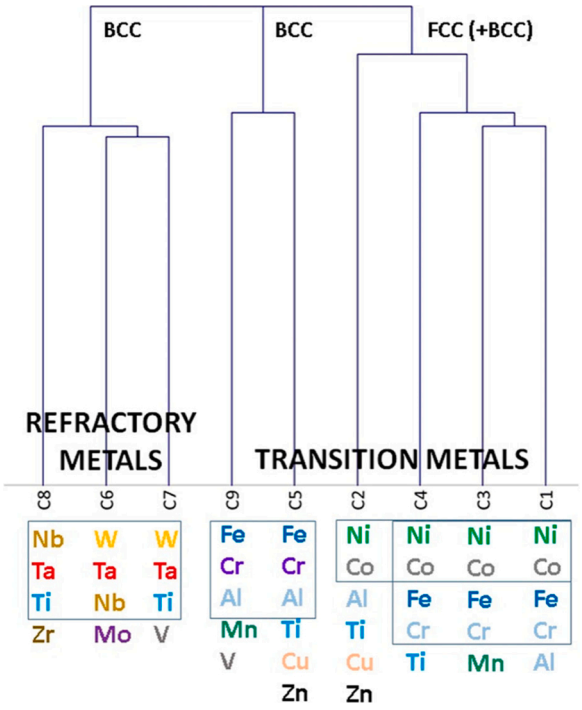

Fig. 10. Torralba et al.'s illustration showing dendrogram plot obtained from the hierarchical clustering classification on the HEAs data set, which shows the 9 types of HEA alloys [171]. Adapted from [171] with permission from Taylor & Francis.

Since the HEMs consisting of five or more principal components provide great freedom for the materials development, the design of new HEMs and the associated manufacturing processes with optimal compositions and experimental parameters become more challenging. Although computational HT virtual screening (HTVS) has emerged as a significant tool in materials science to speed up the discovery of new materials in recent years, the computation-intensive approaches of first-principles calculations is the bottleneck that limits the exploration of the chemical space and large-scale system in HEMs. Studies turned to employ ML replacing exhaustive trial-and-error experiments and calculations. Recently, many ML models have been developed for fast and accurate forward predictions of materials phases and properties of materials. The computational burden of HTVS by the ML framework efficiently explores a large chemical space.

As mentioned earlier, Schmidt et al. suggested that the ML algorithms can be divided into three main categories as supervised learning, unsupervised learning, and reinforcement learning [18]. For the supervised ML, Pedersen et al. manifested the unbiased discovery of new catalyst candidates for the carbon dioxide (CO_2) and carbon monoxide (CO) reduction reactions on CoCuGaNiZn and AgAuCuPdPt HEAs by combining DFT with ML [177]. For the unsupervised ML, Li et al. disclosed (1) intelligent corrupt data detection and re-interpolation to a big tabulated thermodynamic dataset based on an unsupervised learning algorithm and (2) parameterization via ANNs of the purged big thermodynamic dataset into a non-linear equation consisting of base functions and parameterization coefficients on the Al-xZn-2Mg-2Cu alloys (weight percent, wt. %) and $Al_{3.32}Co_{27.27}Cr_{18.18}Fe_{18.18}Ni_{27.27}Ti_{5.78}$ HEA [178].

Meanwhile, the materials inverse design of ML becomes more popular. The inverse design is a goal-oriented approach, which is significantly different from the forward development. It starts from the desired properties or functionalities and ends in the chemical space. Most existing methods of solving inverse problems are based on optimization techniques, such as the genetic algorithm (GA), simulation annealing,

Table 4
Algorithms and the associated methods for HEMs ML.

Methods	Ref.
Linear least-squares regression	[114,184,185]
Generalized linear regression (GLMNET)	[135]
Linear discriminant (LDA)	[135]
Logistic regression	[186,187]
Decision tree (DT)	[135]
Kriging or Gaussian process	[188–190]
Artificial neural network (ANN)	[44,75,127,128,133,135, 187,190–196]
Support vector machine (SVM)	[102,115,128,135,187, 193,197,198]
Decision tree	[186,187]
Random tree/ forest (RF)	[135,185–187,197,199]
k-nearest neighbors	[135,186,193,197]
Naive Bayes	[135,197]
Gradient boosting classifier	[123,185,187]
Conditional generative adversarial network (CGAN)	[134]
Kernel principal component analysis (KPCA)	[115]
Density-functional theory (DFT)	[126,129,138]
Exact muffin-tin orbitals formalism-coherent potential approximation (EMTP-CPA)	[111]
Ab initio calculations	[130,131]
Vienna *Ab initio* Simulation Package (VASP)- Special Quasi-random Structures (SQS)	[111]
Molecular dynamics (MD) simulation	[122]
Computer coupling of phase diagrams and thermochemistry (CALPHAD)	[132,137]
Feature engineering	[136]

and Bayesian optimization [39,134,179,180]. Alternatively, generative models (GMs) in ML are proved to be able to inversely design in material discovery, e.g., the conditional generative adversarial networks (CGAN) for phase and mechanical properties predictions of HEAs [134,181], GAN model for inorganic materials [182], variational autoencoder (VAE) for new crystal structures of solid-state materials [183], and conditional variational autoencoder (CVAE) for molecules [151]. Some selected methods were listed in Table 4.

2.2. HT theoretical & experimental approaches

Traditionally, new materials are developed empirically or through experimental trial-and-error approaches. Since the launch of the MGI in 2011, the MGI led the material science accelerating the data-driven paradigm [21], which boosted the emerging field of materials big data and materials informatics to help businesses discover, develop, and deploy new materials much faster. The materials informatics is a useful approach to reveal the hidden correlations among the elements of materials through big-data analysis, which thus opens new pathways for materials discovery and design. HT techniques are the crucial tools for materials informatics that enables scientists to efficiently produce the big dataset for further extracting information from the materials database. With the rapid development of high-performance computing facilities and parallel computing architectures, HT computing becomes a more efficient way to create data than experiments. Theoretical first-principles calculations and semi-empirical CALPHAD methods are both popular approaches to investigate the atomistic and thermodynamic mechanisms of the HEMs formation, so as for new HEMs design.

First-principles calculations have been widely accepted as the major approach in the atomic-scale materials design. Based on the HT approach, recent studies have led the exponential growth of the material database, which drives the development of a material database system and accelerates materials innovation [200]. For example, the automatic-flow (AFLOW) for materials discovery [201,202] is a repository that first developed the HT framework to generate phase diagrams, electronic structures, and magnetic properties from DFT calculations codes (e.g., VASP and Quantum Espresso) in 2003. All the

Table 5
Current developments of HT DFT tools.

HT-DFT tools	Supported DFT software	Program	Workflow Management
AFLOWπ	Quantum Espresso, VASP	Python 2.7	YES
AiiDA	Quantum Eepresso, GPAW, VASP, Wannier90, Wien2K	Python 2.7	YES
Atomate	VASP	Python 3	YES
MAST	VASP	Python 2.x and 3.x	YES
Fireworks	VASP, ABINIT, NwCHEM, Gaussian and ASE	Python 3.7	YES
Qmpy	VASP	Python 3	YES
PyChemia	VASP, ABINIT, Octopus, DFTB+, and Fireball	Python 3.x	NO

DFTB + is a fast and efficient versatile quantum mechanical simulation software package. FIREBALL is a local-orbital Ab *initio* tight binding implementation of MD.

available results were determined by the HT management workflow named AFLOW π [203,204]. AFLOW π is a public release software, which allows the researchers to customize their automated and robust workflows by constructing consistent datasets and screening properties. The Materials Project [203,205] is another example of the MGI. The Materials Project is an open web-based access database, which provides the DFT-calculated data of all known and predicted materials as well as analysis tools to inspire and design novel materials. The HT management module, Fireworks [204,206], is released on GitHub with comprehensive documentations supported, which can be freely downloaded. People can also modify and re-compile the source codes on the users' own facility in solving specific problems, using Fireworks [204, 206]. Other workflow-management tools, such as atomate [207,208], AiiDa (Quantum ESPRESSO base) [209,210], materials simulation toolkit (MAST) [211,212], PyChemia [213], and qmpy (OQMD) [214], are also free and open-source codes for defining, managing, and executing workflows, which enables researchers to build automated and robust workflows for creating consistent datasets. All these tools are outlined in Table 5.

Apart from quantum mechanics/DFT-based (*Ab initio*) calculations at the sub-nanoscale, scientists are also interested in dynamic *in-situ* behaviors of the HEMs above absolute zero temperature. Accordingly, MD or Monte Carlo (MC) simulations are used to investigate complicated atomistic mechanisms in nanoscale. It is discovered that MD performs well and accurately in agreement with experiments, if interatomic potentials are of "high quality". Unfortunately, there is a significant lack of interatomic potentials for the complex HEM systems. To obtain reliable interatomic potentials, ML is incorporated with HT DFT calculations. Atomic coordinates are mapped to machine-learned energies with two steps: 1. coordinates of an atom and its neighbors are transferred into descriptors, which describes the local chemical environment of an atom. 2. ML methods are applied to map the descriptors to atomic energies. ML-potentials are trained from considerable high-fidelity DFT data including energies, forces, stresses, etc., and hence they are the complicated functions of atomistic position and chemical environment compared with the conventional and empirical potentials. As ML-potentials inherit two advantages at the same time-accuracy in line with first-principles & efficiency of MD simulation in larger scale, different ML-potentials have been proposed, such as Behler-Parrinello neural network potentials (BPNNPs) [215], moment tensor potentials (MTPs) [216], spectral neighbor analysis potentials (SNAPs) [217], deep learning potentials (DLPs) [218], Gaussian approximation potentials (GAPs) [219], and low-rank potentials (LRPs) [131]. These ML-potentials impulse HEMs research into a new stage as they can perform well on many-body interactions in multi-element systems to study and understand the fundamental behaviors of HEAs at different temperatures.

Based on the thermodynamic theory, CALPHAD is a useful approach to predict the phase stability in multi-component systems, such as the

HEAs, for alloys design. Since the 1970s, the CALPHAD technology has been employed to calculate the phase diagrams for new alloy design. There are several commercial products in the market, e.g., PANDAT [220], MatCalc [221], and Thermo-Calc [222] as well as open-sources codes, such as PyCalphad [223] and ESPEI [224]. The thermodynamic models have been widely used for the HEMs design. Although most of the thermodynamic data in CALPHAD is the traditional alloys, several studies have demonstrated that an appropriate selection of binaries and few ternary alloy databases can successfully enable the design of the single-phase solid-solution HEAs, such as the CoCuFeMnNi HEA in the face-centered-cubic (FCC) structure [225], the $Cr_xMoNbTaVW$ HEAs in the body-centered cubic (BCC) structure [226], the AlCoCrNi eutectic HEAs in the FCC and B2 structure [227], and the equilibrium AlCoCrFeNi HEA [104], respectively.

The commercial software, PANDAT [220], has recently implemented the HT tools for efficiently generating thermodynamical properties of Al alloys [228] and HEAs [105]. A Python-based open-source program, named automatic execution and extraction tasks (AEET) [229], is developed for automatic and HT thermodynamic calculations via Thermo-Calc. The general infrastructure is archived [229]. Serving as virtual screening experiments, the HT thermodynamical calculation provides the guidance for the design of real experiments and comprehensive understanding of the influences of heat-treatment conditions and alloy compositions. However, the validity of the CALPHAD predictions for HEAs remains unsatisfactory in some cases, due to the complexity of HEAs and the lack of available thermodynamic and kinetic data for ternary and more complicated systems of the database, which does not ensure the complete prediction of HEAs [230,231]. Although commercial databases for HEAs, such as TCHEA4 [232] from Thermo-Calc., including 26 elements [222], and PanHEA, including 15 elements [233] from Pandat™ [220], are already available, their accuracy still requires additional verification. To improve the results obtained from the CALPHAD with existing commercial databases, previous studies integrated the basic first-principles data with experimental data in the construction of the CALPHAD thermodynamic database [231,234]. However, most of the current HT first-principles calculation data focuses on perfectly ordered stoichiometric phases at absolute zero, which is limited in incorporation with the CALPHAD calculation. Walle et al. [235] developed a set of software tools, included in the alloy theoretic automated toolkit (ATAT) [236]. Walle et al.'s working flow largely automates the process of converting *Ab initio* data into thermodynamic databases that can readily be imported into a standard thermodynamic modeling software and provides a clear path to expand the coverage of HT efforts towards non-stoichiometric phases and non-zero temperatures [235].

In the HT experiment, the technique in preparing a composition gradient in a thin-film material deposition was first conducted to achieve a onetime characterization of a batch of compositions in 1965 [237]. These new methods pave the way for efficiently build up finer and complete composition-structure-property relationships. However, it is noted that the experimental process to synthesize materials is very expensive. The synthesis and characterization techniques have been developed to prepare the compositional-graded bulk alloys, such as the diffusion couples, supergravity field, additive manufacturing, sputter deposition, and laser deposition [238,239].

Ren et al. reported the accelerated discovery of metallic glasses through iterations of ML and HT experiments, which synthesizes and screens a ternary (about 1000 alloy compositions) in a day, resulting in a 100-fold acceleration [240]. Ren et al.'s rapid parallel synthesis of the thin-film alloy deposition was divided into three combinatorial composition spreads as the libraries. Each library was deposited, and the alloys were co-deposited, using single-element targets. Ren et al.'s HT characterizations simultaneously included two-dimensional (2D) X-ray powder diffraction (XRD) patterns and X-ray fluorescence (XRF) mapping on the combinatorial libraries at the Stanford Synchrotron Radiation Lightsource (SSRL) [240]. Ren et al.'s work demonstrated the importance to bridge theory and images, including the 2D structure and functional data from the library, to speed up the materials discovery [241]. For example, with high-resolution detector, the X-ray nano-diffraction (XND) of the Taiwan Photon Source (TPS) provided spatially-resolved mapping for elements, phases, orientation, residual strain–stress, and dislocations at a resolution of 100 × 100 × 50 nm showing the lattice distortion of the HEAs [242].

Some of the HT databases are accessible through an open access repository, such as the high-throughput experimental materials (HTEM) database [243] and materials data facility (MDF) [244]. With the considerable growth of data generated by the HT approach, a Data and Learning Hub for Science (DLHub) provides a ML model repository, associated data transformation, and analysis tools in materials research, which allows researchers to run and publish ML models with flexible application programming interfaces (API) for access, descriptive metadata for building the servable, and persistent identifiers for subsequent citations [245].

While the parallel material synthesis and rapid characterization enable the HT experimental and combinatorial community, it is also not trivial to analyze the associated great amounts of high-quality measurements correlated with the composition, processing, and microstructure. It is important to standardize data formats, build data analysis, and interpretation tools for large-scale data sets. Schmidt et al. summarized several modes of measuring properties, visualizing, and interpreting data for the other materials [18]. The examples of HT measurements for the HEMs are presented in the Part 2 of this manuscript.

2.3. Big-data approach

As Vasudevan et al. commented, here are the needs to organize data across existing platforms and the searchability to find the relevance [93]. Because of the launch of the MGI, the basic infrastructures and techniques for material informatics developed rapidly, and the traditional databases evolved into a data center, which provides the data-distribution platforms or repository for online data storing, sharing, querying, visualization, and analysis. More and more data infrastructures and companies open worldwide. For the open database, the AFLOW database [201], developed by Duke University, includes over 3,405,082 material compounds with over 667,396,072 calculated properties, where the compound includes the binary, ternary, and quaternary systems, and the properties cover the band structures, Bader charges, elastic properties, and thermal properties. The Materials Project database [203], established by Massachusetts Institute of Technology (MIT), provides the structural information and properties of more than 131,613 inorganic compounds, 76,194 band structures, 14,071 elastic tensors, and 49,705 molecules, that collected a huge database from DFT.

Some of the HT databases are accessible through an open access repository, such as the HTEM database [243] and materials data facility (MDF) [244]. The MDF [244] is a data publication network for computational and experimental datasets. There are more than 500 datasets. The HTEM database [243] contains information about materials obtained from HT experiments at the National Renewable Energy Laboratory (NREL), which releases large amounts of high-quality experimental data to public. The HTEM database contains the information about synthesis conditions, chemical compositions, crystal structures, and optoelectronic (e.g., electrical conductivity and band gaps) measurements of the materials. The current public data consists of 37,093 compositions, 47,213 structures, 26,577 optical properties, and 12,849 electrical properties of thin films synthesized using combinatorial methods. Those data repositories provide material data with a standardization format and tools for easy data access, visualization, and exploration [246]. Beside the data repository mentioned above, more than 50 materials repositories have been established, which can be classified into the calculation/experimental database, open access/-commercial database, organic/inorganic database, crystal/liquid

Table 6
Publicly accessible structure and property databases for solid materials and molecules.

Method	Ref.
Automatic-flow for materials discovery (AFLOW)	[130]
Computer coupling of phase diagrams and thermochemistry (CALPHAD)	[249]
Citrination	[247]
Materials Project	[250–252]
Center for Hierarchical Materials Design (CHiMaD)	[253]
High Throughput Experimental Materials Database (HTEM DB)	[243]
National Renewable Energy Laboratory Materials Database (NRELMatDB)	[254]
NIMS Materials Database (MatNavi)	[255]
Novel Material Discovery Repository (NoMaD)	[256]
Computational Materials Data Network (CMD Network)	[257]
Polymer genome	[258]
Matmatch	[259]

crystal/glass database, and so on.

In addition, several companies start up the material-design business based on the material-informatics techniques. For example, MaterialsZone [102] supplied the platform for sharing, screening, visualizing, and managing heterogeneous data sets for rapid materials discovery and ML applications. Granta Design provides commercial data, tools, and expertise for materials design. Citrine informatics [247] and SchrÖdinger [248] established the cloud platform for new materials development with ML and the necessary expertise to develop, commercialize, and scale new materials. With a rapid increase of public and commercial material platform for solid materials and molecules, ML has become a robust methodology applied across many materials disciplines, as summarized in Table 6.

Since the HEAs were introduced by Yeh *et al.* in 2004, a huge number of articles in the Web of Science on the theme of "high-entropy alloys" have been published. Li *et al.* [260] used Keyword Graph analysis of the articles to uncover future development directions of HEAs and the most interesting topics. We follow Li *et al.*'s format and update the Keyword Graph analyzing the number of papers published from 2004 to 2020 to display the research trends of the HEMs in Fig. 11. The change of research keywords with average time in Fig. 11 reveals that the current field of HEAs has attracted increasing attention to microstructure, CALPHAD, corrosion behavior, stability, MD, laser cladding, magnetron sputtering, and films, demonstrating that the current studies are focused on the topics of microstructure, surface coating, and sputtering. Laser cladding and magnetron sputtering are both the most mature techniques for high-entropy coatings [261]. Note that the theoretical study of MD received much attention in recent years, which may attribute to the development of potential functions and parameters [106,262,263]. Due to a significant increase of ML studies for the HEAs design, HT CALPHAD was broadly used to generate training data of microstructure.

2.4. Combinational approach

In recent years, materials discovery and design have taken a huge leap since "combinatorial approach" and "materials informatics" were proposed and applied in different areas, the success of which are attributed to data generated from computational and experimental tracks. From there, the scientists have explored big digital data space via data mining, autonomous systems, and AI techniques. As theoretical methods become more precise and hardwares for high-performance computing become more powerful, large-scale and rapid computational data generation arrives. The accessibility together elevates along with the establishment of many open-source online databases, such as the Materials Project [203] or AFLOW [201]. These infrastructures systematically reposit computational measurements of materials properties calculated through DFT approach, e.g., electronic band structure and formation energy. Likewise, HT experimental data ranging from synthesis to characterization measurements also needs great curation for the community. Many efforts have been made to manage large and heterogeneous data sets, e.g., MaterialsZone [102], NIST [264] are good online systems for handling and analyzing. In a HT manner, integration of computational and experimental data is a new topic for materials science. HT semi-empirical CALPHAD approaches are powerful tools for calculating the phase diagrams for the purpose of structural design. HT ab-inito approach not only compensates the lack of available thermodynamic and kinetic data for CALPHAD calculations but also uses to screening the new stable composition with different structures and desired properties. The HT experiments enable the rapid synthesis and characterizations for validation. On the one hand, combinatorial HT

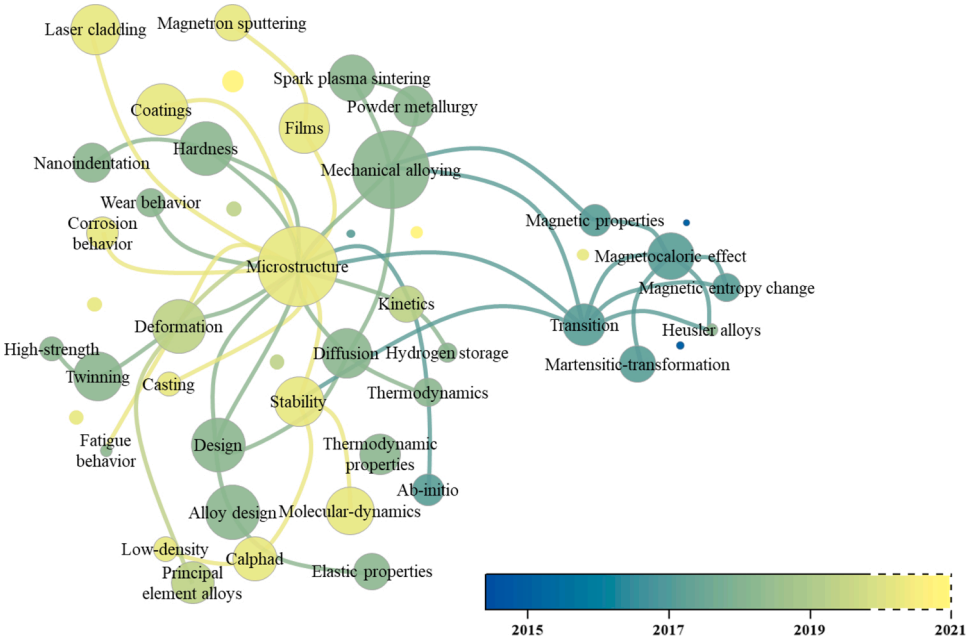

Fig. 11. Changes of research keywords with the average time, reflecting future development directions of HEAs. The search keyword is the "high-entropy alloys" and the total number of articles is 5000 from 2004 to 2020 in the Web of Science. The figure is the extension of Li *et al.*'s statistics [260].

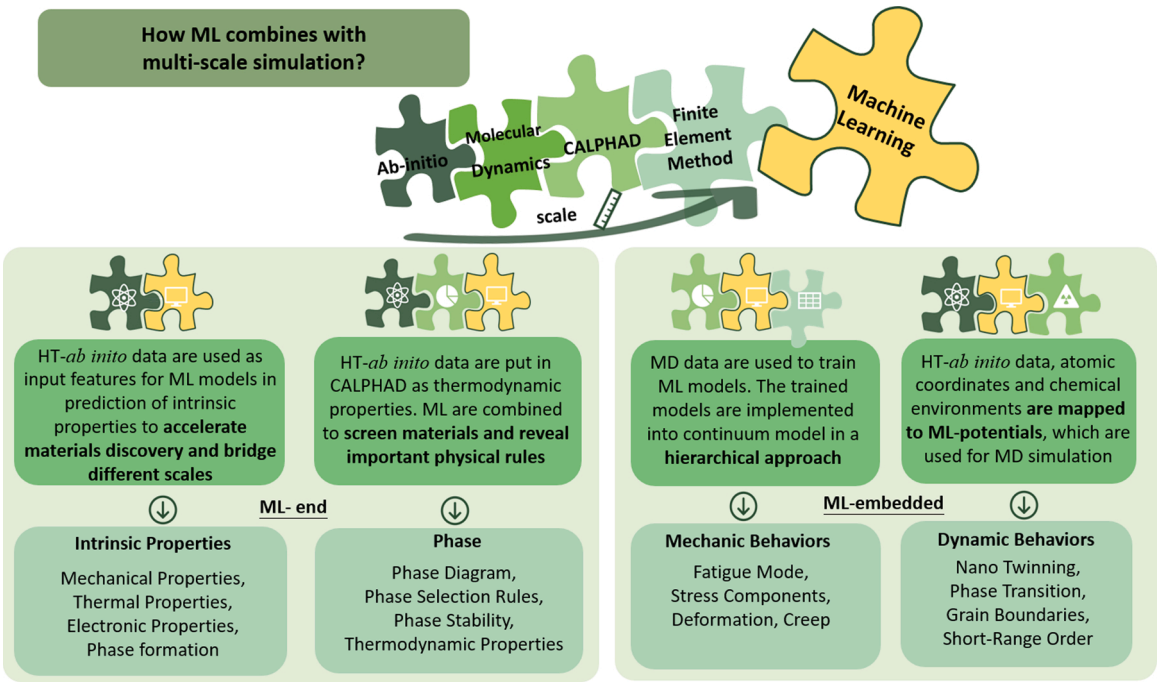

Fig. 12. ML assists the materials exploration and bridges the gap of multiscale simulation.

experiments can validate theoretical predictions based on modeling, particularly in a wide compositional range. Meanwhile, experimental data generated from libraries can then be used to augment or optimize the theoretical models. In summary, effect coupling of experimental and theoretical approaches not only accelerate materials discovery but also bring two domains into a higher level of study.

Apart from experimental and theoretical information, data generated from multi-scale simulations in terms of different applications can also be incorporated with ML, as shown in Fig. 12. As for the ML at the end manner (left block), this method utilizes existing resources (data) in either inverse discovery of novel materials or forward prediction of properties and structure, saving much time and cost. Meanwhile, the physical rules of prediction results can be unveiled from the weighting of various input features. ML can also be embedded in these combinatorial approaches, as shown in the right block of Fig. 12. To investigate mechanical behaviors of structural components such as fatigue mode and stress components, computational results of MD or MC simulations are used to train ML models. Subsequently, the output of training models is implemented into FEM to substitute constitutive relations used in the conventional continuum models. This hierarchical approach shows the potential of ML in connecting nano mechanics with structural mechanics [265]. To gain in-depth analysis of dynamic behaviors for nano-structure, ML is also available for bridging *Ab initio* calculations with MD simulations by mapping atomistic coordinates and chemical environments to ML-potentials. Nano twinning, grain boundaries, and phase transition of materials under specific temperatures are then identified accurately and efficiently via the combinatorial approaches.

2.5. Summary

Materials design continues to progress in order to save cost and time as well to enhance performance simultaneously. The scientists are making efforts in tailoring composition, process, and structures with the aim of the improved properties and performances of materials. Fig. 13 illustrates the innovation for new materials discovery.

Traditionally, experimental approaches are based on physical intuitions and/or expensive trial-and-error strategies. Theoretical methods offer the way to understand the most fundamental and important information of materials. HT approaches are the platforms that provide a rapid and systematical synthesis, characterization, and calculations for materials screening. However, the drawbacks of HT approaches are limited by the user-selected library (compositions) and experts' intuitions, which could miss out on high-performing materials. Data-driven science as materials-informatics technique is possibly implemented by data mining, ML, and mathematical optimization using the existing database and HT data, resulting in a new pathway to understand the materials and enable the innovation of materials design. In other words, HT screening with machine-learned predictors may filter out preferable materials as well disclose the fundamental physical and thermodynamic rules. In addition, global optimization and generative models as deep learning models can be utilized to build new hypothetical crystal structures and compositions for HTVS that go beyond the existing structural and compositional motifs. The greatest value is its powerfulness for systematically extracting physical relationships, mechanisms, and principles [61] such as PSPP relations. Hence, the combinatorial HT approaches correlated with materials informatics have the potential to speed up the development schedule and boost the innovation of the HEMs, as well as to reduce the cost for competitive materials discovery. However, there are still some challenges herein mainly based on the original collected data, such as accuracy, representation, and heterogeneity. As long as we have reliable data of high quality, materials informatics is a powerful wheel promoting the development of materials science.

Again, since the HEMs provide a huge space of great tunability for design, materials informatics can assist with daunting tasks to untangle unanswered questions and explore unexploited domains. There are growing data repositories established in recent years for the HEMs. Most of the HEMs data are the data of phase diagrams and material hardness whereas the other properties are introduced below.

3. ML and HT studies for HEMs

Chen et al. reported several successful cases using ML for the HEAs in which ML can make scientists better [65]. For example, to design the multiphase HEMs, Krishna et al. employed the ML approach with a data set of 636 alloys and predicted the HEAs with a mixture of the solid

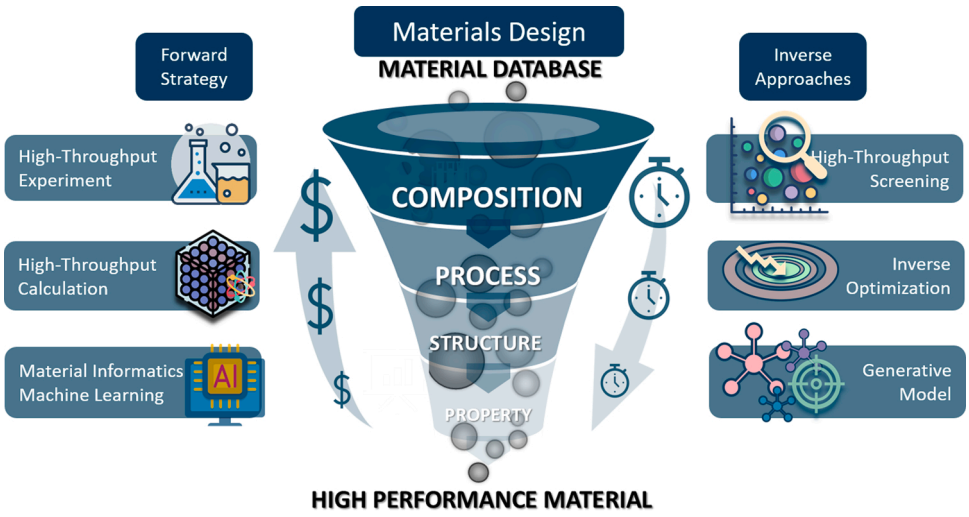

Fig. 13. Towards ML and material informatics to enhance combinatorial HT calculations and experiments for material discovery and innovation.

solution and intermetallic (SS + IM) [187]. Krishna et al.'s ML algorithms comprised logistic regression, decision tree, SVM classifier, random forest, gradient boosting classifier, and ANN. ANN has shown the best accuracy of more than 80 % of the test data. Their predictions were verified, and ANN is a more accurate prediction in their HEMs system [187]. For medium-entropy alloys (MEAs), Li et al. combined HT simulation with ML to obtain MEAs with high strength and low cost [190]. Roy et al. employed a gradient boost regressor ML method to predict Young's modulus of low-, medium- and high-entropy alloys with root-mean-square error (RMSE) of 87.76 %, revealing that T_m and ΔH_{mix} are the most important descriptors [123].

Besides these successful cases, due to the complexity of the HEMs, Miracle *et al.* proposed new strategies to accelerate the discovery and development of HEMs [33]. Miracle *et al.*'s strategies start with the calculated phase diagrams to quickly screen the alloy candidates, which can save more resources as the Stage Zero. Comparing with the required time to examine the candidate materials via a computational approach, Miracle *et al.* then suggested to investigate the structure-insensitive properties as the Stage One for the first experimental step. Miracle *et al.*'s final evaluation is to measure the properties that depend on both compositions and microstructures [33]. Along this vein, in this session, we review the structure-insensitive properties of the HEMs. Since the HT and combinatorial experiments are well established for functional materials, the second part of this session is the review of the functional properties of the HEMs. Finally, we review the other properties of the HEMs which depend on both compositions and microstructures. With Tshitoyan *et al.*'s unsupervised word embeddings capture methods [50], the previously unrecognized correlations of these composition-microstructure-dependent data may be unveiled for new applications.

To promote ML-based optimization, the validation of the ML results by experiment or physics-based simulation is important for the interpretability, thus, HT data acquisition capabilities are critical [65]. DeCost *et al.* concluded that critical bottlenecks for adaptive science and autonomous control of experimental systems are (i) a widespread absence of API to interact with laboratory equipment, (ii) lack of a unified language for experimental workflow protocols, and (iii) lack of standardized and open data formats to facilitate accessibility and interoperability [61]. Therefore, in this session, we will review the selected examples showing the complimentary and validated results using HT methods.

Zhao summarized the HT experimental tools for the materials genome, which focused on the experimental tools for HT and high spatial resolution measurements of the materials properties such as phase, elastic modulus, thermal conductivity, specific heat capacity, and thermal expansion [266], which can be applied for the HEMs. Specifically, it is important to generate and apply the "libraries" from both experiment and theoretical tools [93]. In terms of HT screening of the experiments, a screening facility typically holds a library of stock and assay plates. For example, Li and Flores employed a HT direct laser deposition processing method to construct $Al_xCoCrFeNi$ HEA microstructural library, which $x = 0.51 \sim 1.25$ [267]. The samples are graded in composition and quench rate ranging from 26 ~ 6400 K/s. Li and Flores found that the microstructural feature sizes followed a power law relationship with the quench rate. Their study demonstrated that laser processing coupled with microstructural library was an effective method for HEA developments [267].

Haase *et al.* reported a methodology that combines thermodynamic modeling with 3D printing of elemental powder blends for HT investigation of the Co-Cr-Fe-Mn-Ni HEAs system [268]. For bulk sample production, Haase *et al.*'s laser metal deposition of an elemental powder blend allows high flexibility in varying the chemical composition while the microstructural, texture, and mechanical properties of the processed materials were characterized, using optical microscopy (OM), electron backscatter diffraction (EBSD), energy dispersive X-ray spectroscopy (EDS) analysis, XRD, and hardness and compression testing [268]. Similarly, Moorehead et al. also presented the HT synthesis using additive manufacturing [269]. Moreover, Moorehead et al. designed HEAs sample arrays for *in-situ* alloying of elemental powders, where scanning electron microscope (SEM), EDS, and XRD were performed while the samples were remained on build plate to construct the library. Besides their HT synthesis and characterization, Moorehead et al. utilized CALPHAD calculations via PanDat™ as the HT modeling to predict the equilibrium phases of each printed alloy composition at 300 °C. Moorehead *et al.* found a discrepancy between the simulated and printed HEAs, such as certain Ta-rich and Nb-poor compositions due to the slow diffusivity of refractory metals at this temperature [269].

Moorehead *et al.* applied similar HT additive manufacture synthesis, characterization, and CALPHAD procedures to map the compositional array of the Cr-Fe-Mn-Ni alloys to build the library for the irradiation investigations [270]. Moorehead et al. reported that radiation-induced hardening was observed in the compositionally complex alloys (CCAs), which was comparable to neutron irradiation [270].

Besides the applications of the aforementioned additive manufacturing for the HT synthesis, Xu *et al.* carried out *in-situ* HT synthesis of FeCoNiCrCuAlx in a transmission electron microscope (TEM). The dynamic melting process of FeCoNiCrCu with Al was recorded, and the composition of FeCoNiCrCuAlx was examined by EDS.

Xu et al.'s *in-situ* HT method in the TEM avoid the drawbacks of the conventional arc-melting and casting, where the repetitious melting processes can cause the evaporation of some low-melting-temperature elements at the high temperature environment [271].

3.1. HT studies on the structure-insensitive properties of HEMs

The structure-insensitive properties reviewed in this session mainly focus on the moduli and thermal expansion. Several *in-situ* instruments are presented because these advanced methods obtain multi-scale properties of the HEAs simultaneously from the bulk to the lattice-level properties [272].

As mentioned earlier, Kim et al. investigated the relationship between the elastic properties and lattice distortion using a combined experimental and computational approach based on *in-situ* neutron-diffraction characterizations and first-principles calculations [78]. Kim et al. selected the single-phase FCC $Al_{0.3}$CoCrFeNi HEA because the constituent elements have large size differences. Kim et al.'s calculated elastic constant values are within 5% of the ND measurements and indicated that the lattice distortion results in the reduced stiffness. Kim et al. implemented ML modeling, which was trained on a large dataset of inorganic structures, to predict the elastic moduli of HEAs. Their ML models also demonstrated the dependence of bulk and shear moduli on several material features, such as (a) cohesive energy, (b) group number, (c) density, (d) radius, and (e) electronegativity, which act as guides for tuning elastic properties in the HEAs [78]. Similarly, Yen et al. applied the Lennard-Jones potential, the embedded atom method (EAM) potential, and the modified embedded atom method (MEAM) to investigate the lattice distortion effect on Young's modulus E (hkl) and Poisson's ratio ν (hkl, θ) along [100,110,111] loading directions for the FeCrNi MEA and CoNiCrFeMn HEA comparing with the pure Ni and other FCC metallic systems as the references [273]. Yen et al. used the *in-situ* ND data [77] as the inputs and recursively fitted their simulation and complimentary neutron results. Yen et al. unveiled that the effect of electron density inconsistency is more dominant than the effect of lattice distortion associated with the atomic size difference. The anisotropy of the CoNiCrFeMn HEA from their simulation and *in-situ* ND measurements is self-consistent [77].

In both Kim et al.'s [78] and Yen et al.'s [77] cases, the advanced photon source indicated an important capability to illuminate multiple diffractions at the lattice levels for *in-situ* measurements on the bulk samples, which reveals much more mechanisms than just phase characterizations. In particular, the main advantage of the *in-situ* neutron environment is the possibility of investigating the evolution of microstructures since identical specimens are monitored the entire time and are subjected to the changes of the control parameters. Moreover, most of the ND instruments are equipped with strobing software, such as the VULCAN Data Reduction and Interactive Visualization software (VDRIVE) [274] of VULCAN at the Spallation Neutron Source (SNS) of Oak Ridge National Laboratory (ORNL), which may reduce the data at the end of each test and is much more useful. The strobing system is a continuously running software utilizing event-based data acquisition where each neutron carries a time stamp. In this case, diffraction data can be collected continuously and binned later according to the desired time scale for the HEMs [77,275,276]. TAKUMI [277] is another materials engineering diffractometer located in Japan at the Japan Proton Accelerator Research Complex (JPARC) that is capable of various *in-situ* environments, including elevated-temperature measurements. The *in-situ* loading setup of TAKUMI enables the measurements of the fatigue behavior in the HEAs [278,279] while low-temperature *in-situ* loading setup of TAKUMI captures the serration behavior of the CrMnFeCoNi HEA [280]. The Spectrometer for Materials Research at Temperature and Stress (SMARTS) at the Los Alamos Neutron Science Center (LANSCE) [281] in the US and ENGIN-X [282] of the ISIS at the Rutherford Appleton Laboratory (RAL) in the UK also have the same features of the measurements [283–285]. For a reactor-based neutron diffractometer, the Residual Stress Instrument (RSI) installed at the High-Flux Advanced Neutron Application Reactor (HANARO) of the Korea Atomic Energy Research Institute (KAERI) also conducted the temperature-dependent mechanical-behavior evolutions of the HEMs [286]. Similarly, synchrotron X-rays can also illuminate the microstructure with high penetration. For example, the *in-situ* loading measurements capturing the deformation-induced phase transformation [287–291]. Following is an example of the heating setup of one of the synchrotron X-rays in the TPS [292] where the temporally coherent X-ray diffraction (TPS-09A) [293] can heat the samples up to almost 1200 K to examine the lattice thermal expansions and the phase stability [294] while the TPS 21A XND and the TPS 23A X-ray nanoprobe (XNP) provide spatially-resolved mapping for the HEMs to distinguish local lattice distortion associated with element distributions [242], as shown in Fig. 14. More examples of the neutron and synchrotron X-ray measurements for their potential HT examinations can be found in Calder et al.'s summary [295]. Lee et al.'s recent report manifested the temperature dependence of elastic and plastic deformation behavior of a NbTaTiV refractory HEA (RHEA) using *in-situ* ND [296].

Moreover, beyond the structure-insensitive properties, s mentioned earlier, Gao et al. applied ML to their CPFEM in the NiCoCrFe system based on their *in-situ* ND experimental data and physical mechanisms to provide the data set [75]. Similarly, Dai et al. recently demonstrated the micromechanical behaviors of a polycrystalline metal by ANNs from the *in-situ* diffraction data. Dai et al.'s ANN model was trained based on the datasets generated by the physics-based viscoplastic self-consistent (VPSC) model, which captures the loading path-dependent micromechanical behavior of the copper polycrystals with arbitrary texture, even beyond the bounds of the generated dataset [297].

3.1.1. Studies for the moduli of the HEMs

Vegard's law is an approximate rule, which empirically estimates the crystal lattice constant of an alloy based on a linear relation for the concentrations of the constituent elements [76]. From Vegard's law of the simple mixtures, the lattice constants determined by the relative atomic sizes are the reference points to calculate the moduli of the crystals.

Although DFT is known to estimate the cohesive energies, volume per atom, and bulk moduli, due to the complex of the HEMs, the determination of the suitable modeling size and associated moduli is not trivial. Moreover, the HEMs may contain some late transition metals, such as Ag, Au, Cd, Ga, Tl, Pb, and Bi. These elements may influence the calculations of DFT with the description of the d-electron correlation, dispersion, relativistic effects, and spin-orbit coupling for HT DFT calculations [301]. By applying HT calculations, Jong et al. demonstrated a statistical learning framework to estimate the elastic moduli of k-nary inorganic polycrystalline compounds of diverse chemistries and structures [301]. Jong et al.'s datasets are diverse, and they constructed descriptors that generalized over the chemistry and crystal structure, incorporating multivariate local regression within a gradient boosting framework [301]. Jong et al.'s moduli predictions showed that there is a discrepancy between the gradient boosting machine local polynomial regression (GBM-Locfit) and DFT. Jong et al. disclosed that there were DFT methods-related errors, which added noise to the underlying physical phenomenon.

To verify the predictions, it is important to compare with the measured temperature dependence of elastic constants. For the HEMs, Laplanche et al. summarized the elastic moduli [302] of the Cantor alloys [34] and their associated subsystems of CrFeCoNi, CrCoNi, CrFeNi, FeCoNi, MnCoNi, MnFeNi, and CoNi in Figs. 15 and 16. The thermal-expansion coefficients of these HEAs and their subsystems were presented in Fig. 19 [302,303]. Laplanche et al.'s temperature-dependent thermal-expansion coefficients and elastic moduli, which are mainly from the measurements on the bulk samples, are useful for quantifying fundamental aspects of the HEAs for structural analyses [302,304].

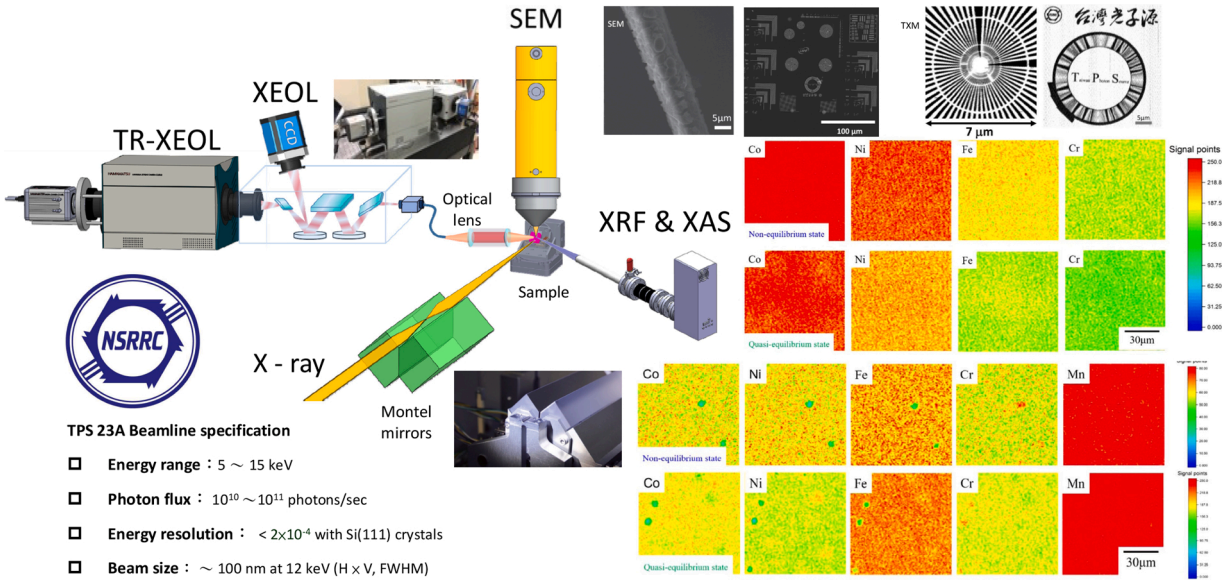

Fig. 14. Spatially-resolved mapping for the HEMs to distinguish the local lattice distortion associated with the element distributions [298–300].

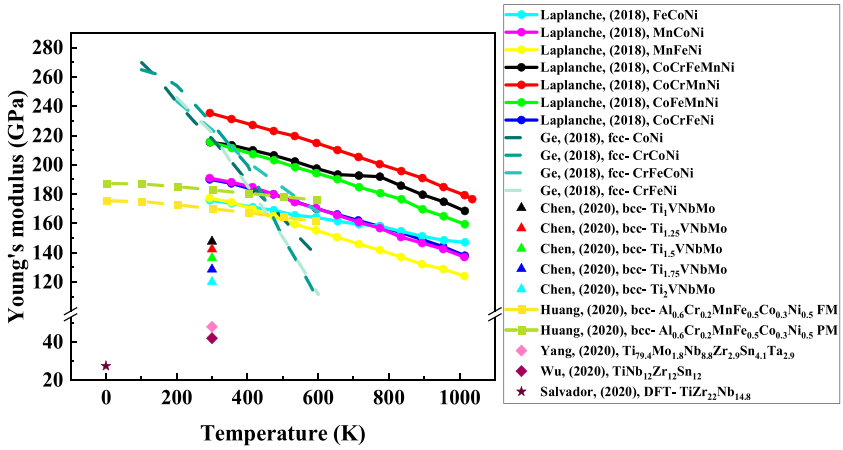

Fig. 15. Temperature dependencies of the Young's moduli. (Data taken from experiments [302,304–307] and DFT calculation [84]) of the HEAs.

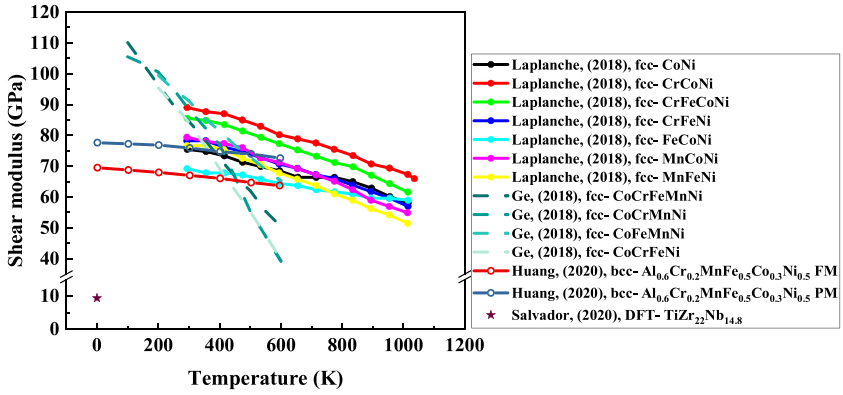

Fig. 16. Temperature dependencies of the shear moduli of HEAs. (Data taken from experiments [302,304,307] and DFT calculation [84].

There is a clear gap between the Ti-based HEAs and the others in Figs. 15 and 16. For the biomedical applications, Yang et al. employed the XGBoost model and GA to search for BCC β-Ti alloys with low Young's modulus in the Ti-Mo-Nb-Zr-Sn-Ta system. They found that the $Ti_{79.4}Mo_{1.8}Nb_{8.8}Zr_{2.9}Sn_{4.1}Ta_{2.9}$ has the lowest Young's modulus of 48 GPa in prediction and 46 GPa in experimental validation [305]. Wu et al. trained a NN model to explore new alloys meeting the criteria for bio-compatibility, low modulus, and low cost for the development of orthopedic and prosthetic implants. The new and affordable cost Ti alloys (Ti-12Nb-12Zr-12Sn) were found and validated by experiment,

which had the bone-like Young's modulus (42.4 GPa), high tensile strength (900 MPa), acceptable ductility, and biocompatibility [306]. Salvador et al. also attempted to discover low modulus of Ti-Nb-Zr system with ML. Materials Project database was fed to the linear models, random forest regressors, and ANNs models to evaluate the prediction reliability. According to the analysis results, the Ti-22Zr-14.8Nb is the most promising candidate in the biomedical field, which exhibits a low elastic modulus of 30.8 GPa, shear modulus of 10.6 GPa, Young's modulus of 3.79 GPa, and elevated beta-phase stability [84]. These three Ti-based alloys shown here are to demonstrate the contrast between the HEMs for the structural and biomedical applications, but not from the simulation and experimental methods.

Besides the bulk moduli evolution subjected to environmental temperatures, the orientation-dependent (*h k l*) moduli of the Cantor Alloys can be obtained by *in-situ* ND measurements [307]. Huang et al. heated the selected HEA in the load frame to 200 °C, 400 °C, and 600 °C using an induction-coil heating system of the VULCAN diffractometer at the ORNL [307]. The results were shown in Fig. 17. The upper limit was selected as 600 °C because it was below the effective high temperature to avoid vacancy formation [242] and creep [286] during the measurements. The diffracted neutrons were refined, using the general structure analysis system (GSAS) software based on the Rietveld method [308]. The data acquisition streamlines the coordination between the mechanical load control and neutron-data collection. The event-based data-reduction software, VDRIVE, was built specifically for this data structure and experiment scheme [274]. The collected data was chopped in 5 min [309]. With the event-based data acquisition of the materials-engineering diffractometer, such as VULCAN [309] of SNS, multiple diffraction peaks were collected simultaneously under applied loads for their hkl-dependent moduli measurements, as shown in Fig. 17. There is a discrepancy between the lattice moduli of different orders of the (*h k l*). For example, E_{111} as the modulus of (*1 1 1*) plane and E_{222} as the modulus of (*2 2 2*) have different trends subjected to temperature. The evolutions of the lattice spaces, d_{111}, as for the diffraction peak of (*1 1 1*), and d_{200}, as for the diffraction peak of (*2 0 0*) have different tendencies [307]. These features indicated the effects of stacking faults in the Cantor alloys, which resulted in different responses of the lattices subjected to the environmental temperature changes.

Moreover, the *in-situ* diffraction measurements could be applied to obtain the tensors of the crystal materials [283]. The model fitting coupled with the bulk properties and diffraction data enabled crystal-plasticity-based investigations [310]. For example, to obtain the stiffness tensors (C_{ij}), the generalized Hooke's law from the compliance tensors (S_{ij}), which is the second-order tensor expression for the elastic compliance, M^e can be derived for homogeneous and isotropic materials in the FCC structure, as shown in the Eqs. (9)–(11).

$$C_{11} = (S_{11}+S_{12})/(S_{11}-S_{12})(S_{11}+2S_{12}) = \left(\frac{1}{E}-\frac{\nu}{E}\right)\Big/\left(\frac{1}{E}+\frac{\nu}{E}\right)\left(\frac{1}{E}-\frac{2\nu}{E}\right) \tag{9}$$

$$C_{12} = -S_{12}/(S_{11}-S_{12})(S_{11}+2S_{12}) = \frac{\nu}{E}\Big/\left(\frac{1}{E}+\frac{\nu}{E}\right)\left(\frac{1}{E}-\frac{2\nu}{E}\right) \tag{10}$$

$$C_{44} = 1/S_{44} = G \tag{11}$$

where E is the Young's modulus, G is the shear modulus, and ν is the Poisson's ratio.

For the temperature-dependent stiffness tensors C_{ij} for C_{11}, C_{12}, and C_{44}, the aforementioned Laplanche et al.'s empirical fitting results obtained from the thermal coefficients [303] can be used in the Eqs. (12)–(14):

$$G = 85 - 16\Big/\left(e^{488/T}-1\right) \tag{12}$$

$$E = 214 - 35\Big/\left(e^{416/T}-1\right) \tag{13}$$

$$\nu = -1 + \frac{E}{2G} \tag{14}$$

For the model fitting, Wu et al.'s room-temperature data [276] was used in Fig. 18. For the tensors at other temperatures, Huang et al.'s data [77] shown in Fig. 17 was used together with other data [311,312]. The data taken from *in-situ* ND measurements can yield the *hkl*-dependent moduli (E_{hkl}), as shown in Fig. 17. By the application of the following directional cosines (*l*, *m*, and *n*) from lattice planes with respect to the three orthogonal axes, the stiffness tensors (C_{ij}) for C_{11}, C_{12}, and C_{44} can also be derived:

$$E_{hkl} = s_{11} - 2\left[(s_{11}-s_{12}) - \frac{s_{44}}{2}\right] \times \left(l^2m^2 + m^2n^2 + n^2l^2\right) \tag{15}$$

The fitted bulk stress–strain and predicted lattice-strain curves were archived [313]. In Fig. 18, the temperature-dependent stiffness tensors, C_{11}, C_{12}, and C_{44}, derived from the coefficients of thermal expansions [303] were described in the black, red, and blue dashed lines, respectively. Recalling Shu-min et al.'s maximum entropy approach for simulating the elastic properties of HEAs [314], the effect of the local environment and lattice distortion on the HEAs can contribute to the elastic properties. The tensors derived from the ND data [77] were validated by Yen et al.'s model fittings [273]. Specifically, Yen et al. identified that the effect of electron density inconsistency is more dominant than the effect of lattice distortion associated with the atomic-size difference. The electronic configuration in the HEAs environment plays a greater role in the elastic anisotropy than that in the differences among the atomic radii [273].

MehdiJafary-Zadeh et al. developed a ML interatomic potential based on an efficient "learning-on-the-fly" scheme for the CoFeNi, which was moment tensor potential (MTP), to unravel the effects of local lattice distortion on the elastic properties of MPEAs [122]. Using this potential, MehdiJafary-Zadeh et al. performed MD simulations to calculate the

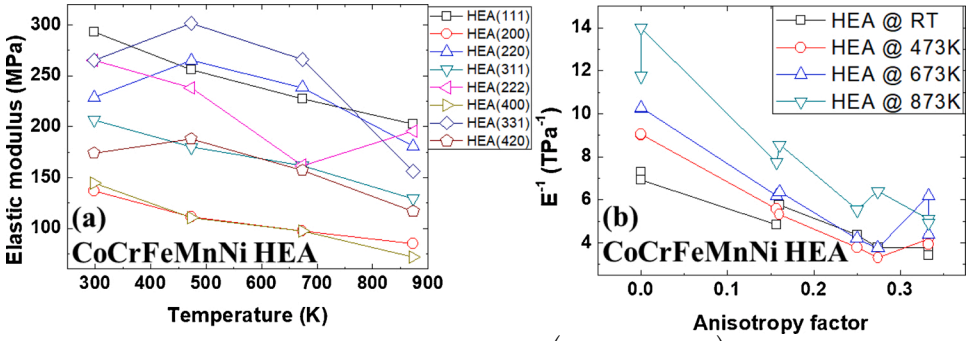

Fig. 17. (a) The hkl-dependent moduli of the HEAs; (b) The associated anisotropy factor $\left(A_{hkl} = \frac{h^2k^2+k^2l^2+h^2l^2}{(h^2+k^2+l^2)}\right)$. (Adapted from [77] with permission from Elsevier).

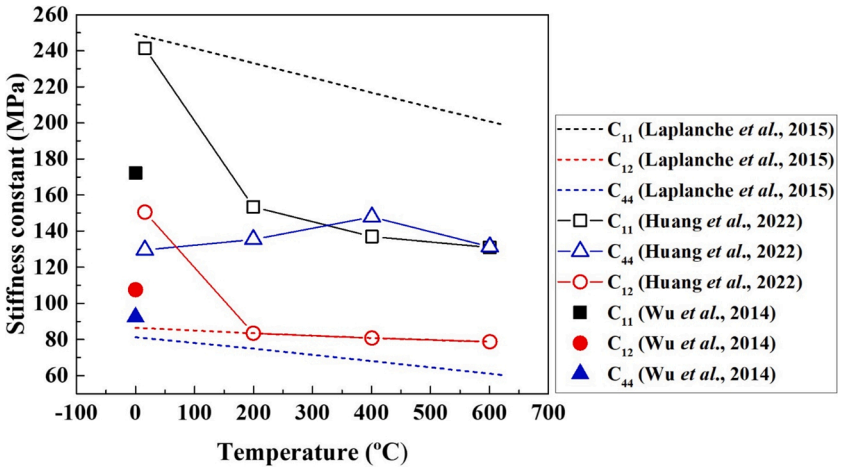

Fig. 18. Temperature-dependent stiffness tensors (((C_{11}, C_{12}, and C_{44}). Neutron-derived results were shown in the empty symbols. Data taken from [276] were represented by the solid symbols; data derived from [303] were represented by the dashed lines; data derived from [77]. C_{11} (■), C_{12} (●), and C_{44} (▲) data derived from E_{hkl} taken from ND [276]. The stiffness tensors resulting from thermal expansion were C_{11} (black dashed line), C_{12} (red dashed line), and C_{44} (blue dashed line). The stiffness tensors (C_{ij}) for C_{11}, C_{12}, and C_{44}, presented as the empty squares (□), circles (○), and triangles (△), respectively, were taken from Huang et al.'s data [313]. As reported, there was neither significant vacancy formation [242] nor creep [286] during heating up to 873 K. (Adapted from [313] with permission from Elsevier) (For interpretation of the references to colour in this figure legend, the reader is referred to the web version of this article.).

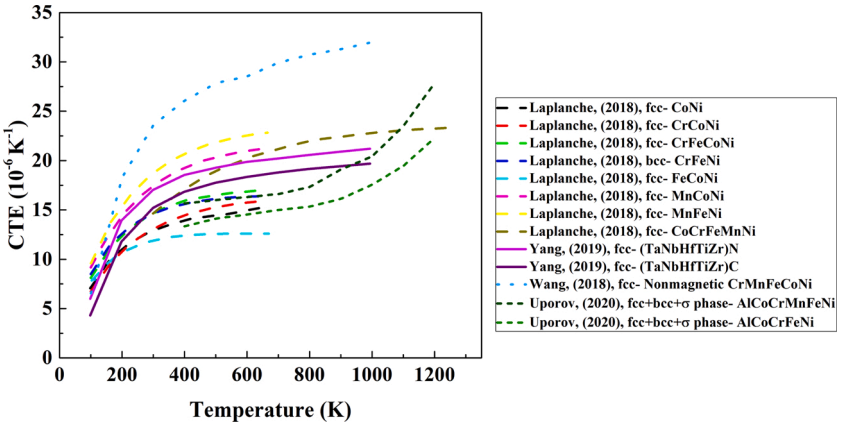

Fig. 19. Temperature dependencies of the thermal expansion coefficients in the HEAs. (Data taken from [302,321,322]).

elastic moduli of single- and polycrystalline CoFeNi [122]. Dai et al. [113] employed DLP to predict the temperature dependence of thermal (lattice constants, anisotropic thermal expansions, and anisotropic phonon thermal conductivities), and elastic properties (elastic constant, bulk, shear, and Young's moduli) for high-entropy $(Ti_{0.2}Zr_{0.2}Hf_{0.2}Nb_{0.2}Ta_{0.2})B_2$ from 0 °C to 2500 °C. They found that the obtained data from their predictions were well consistent with those from the experiments at room temperature. Besides, the lattice distortion was not severe by characterizing the displacements of atoms from ideal positions.

Above all, Gorsse et al. [315] summarized the mechanical properties of 370 HEAs and CCAs reported in the period from 2004 to 2016. Their data sheets comprised alloy composition, type of microstructures, density, hardness, type of tests to measure the room-temperature mechanical properties, yield strength (YS), elongation, ultimate tensile strength (UTS), and Young's modulus from Miracle and Senkov's [1], Gorsse et al.'s [316], and Senkov et al.'s [317] publications, respectively. Specifically, they reported 27 RHEAs, the yield stress and elongation were given as a function of temperature [315]. Recently, Shukla et al. utilized the friction stir gradient alloying as a HT screening technique for the HEAs. The Young's modulus value is one of the retrieved properties in their $Fe_{40}Mn_{20}Co_{20}Cr_{15}Si_5$ HEA system [318].

3.1.2. Studies on the thermal expansion of the HEMs

Thermal expansion is another important structure-insensitive property [33], especially for the materials subjected to temperature fluctuations. Thermal expansion originates from the potential energy on the mean separation of atoms. Specifically, the elastic properties of crystals relate to atomic-vibrational spectra, according to the Debye's model, which can be used to calculate the lattice specific heat [319]. Grüneisen performed one step further to correlate the specific heat with the volume expansivity [320]. As the reinforcement phases usually have a lower coefficient of thermal expansion (CTE) than the matrix, thermal stresses may develop during solidification and processing and thus affect the strength. To calculate thermal stress at a given temperature, a knowledge of CTEs and elastic constants were required [302]. The CTE (α) was defined below [302].

$$\alpha = \alpha_{HT}\left(1 - e^{-T/\Theta_D}\right) \tag{16}$$

where α_{HT} is the value of CTE in the high-temperature limit, and Θ_D is the Debye temperature.

Because thermal expansion is one of the fundamental properties of the materials, many models in terms of the state functions have been applied to predict the thermal expansion. There are several ML predictions of thermal expansion for the concrete [323], inorganic glasses [324], and even the negative thermal expansion materials [325].

However, due to the complicated configurations of the HEMs, the temperature-dependent thermal expansions are not intuitive [46,326]. For example, from Santodonato et al's work, they found the deviation

from high-entropy configurations in the atomic distributions of the $Al_{1.3}$CoCrCuFeNi model system [327]. It is even more intricate to obtain the temperature-dependent thermal expansions in the HEMs at higher temperature due to the ease of the vacancy formation entropy at higher temperature. As shown in Fig. 19, Huang et al. followed Simmons and Balluffi's concept [328] and compared the differences between the lengths subjected to high temperatures from time zero to the time reaching quasi-equilibrium state [242]. The dilation of the bulk specimen, $\Delta L/L$, and the change in the lattice parameter, $\Delta a/a$ were defined as follows

$$3(\Delta a/a) = p(T) + r(T) + x(T) \tag{17}$$

$$3(\Delta L/L) = q(T) + s(T) + y(T) \tag{18}$$

where $p(T)$ and $q(T)$ are the ideal thermal expansion without thermally generated defects, $x(T)$ and $y(T)$ are expansion arising directly from the formation of defects, and $r(T)$ and $s(T)$ are the thermal expansion of the crystal due to the presence of lattice defects that alter the lattice frequency distribution and thus internal energy.

At time zero, the major contributions to the thermal expansion are the $p(T)$ and $q(T)$ without thermally generated defects. At the time when the samples reach quasi-equilibrium, expansion arising directly from formation of defects and the thermal expansion of the crystal due to the presence of lattice defects altering the lattice frequency distribution and internal energy all influence the thermal expansion of the HEMs [242]. In Fig. 20(a), $\Delta L/L$ and $\Delta a/a$ of the CoCrFeMnNi are shown as a function of temperature. The bulk expansion, $\Delta L/L$, subjected to quasi-equilibrium and non-equilibrium states were shown in the red dashed line and green dashed line, respectively. The results of $\Delta a/a$ (the solid black line) were calculated, using the second-order polynomial fitting, following the methodology of Bichile and Kulkarni [329,330] in formulating the second-order polynomial fit for thermal expansion coefficient estimations [330]. It can be observed that $\Delta L/L$ increases with increasing temperature, and the second-order polynomial curve closely matches the results up to a temperature of approximately 1000 K but deviates at temperatures higher than 1000 K.

The evolutions of vacancy formation as a function of the homologous temperature (T/T_m) in the HEAs and the reference Cu alloys subjected to heating were shown in Fig. 20(b) where T_m is the melting temperature of materials. The observable onset temperature of vacancy formation in the pure Cu is approximately 0.74 T_m. However, the observable onset temperature of vacancy formation in the CoCrFeNi and CoCrFeMnNi HEAs is approximately 0.6 T_m, suggesting that vacancy formation is easier in the HEAs. The consequence of the vacancy formation subjected to heating may induce severe lattice distortion, as mapped by the TPS 21A XND and the TPS 23A XNP from their spatially-resolved mapping for both the CoCrFeNi and the CoCrFeMnNi HEAs [242].

Hence, for the high-temperature thermal expansion of the HEMs, ML is needed to solve the complexity as formulated in Eqs. (17) and (18). Using ML, Buranich et al. applied the complex of analytical algorithms (linear, random forest, and gradient boosting regression) to calculate the thermal and mechanical properties of TiNbHfTaW, CrNbHfTaW, and VNbHfTaW HEAs, which are refractory metals-based HEAs [185]. For the other HEMs, Dai et al. performed theoretical predictions on the thermal and mechanical properties in the high entropy $(Zr_{0.2}Hf_{0.2}Ti_{0.2}Nb_{0.2}Ta_{0.2})C$ by a deep learning potential [112]. Dai et al. verified their predictions by comparing the measured lattice parameters and elastic constants in the mono-phase carbides TMC (TM = Ti, Zr, Hf, Nb, and Ta) at room temperature. Their predictions included the lattice constants (ranging from 4.57 Å to 4.67 Å), thermal expansion coefficients (ranging from 7.85×10^{-6} K^{-1} to 10.58×10^{-6} K^{-1}), phonon thermal conductivities (ranging from 2.02 W m^{-1} K^{-1} to 0.95 W m^{-1} K^{-1}), and elastic properties of high entropy $(Zr_{0.2}Hf_{0.2}Ti_{0.2}Nb_{0.2}Ta_{0.2})C$ in temperature ranging from 0 °C to 2400 °C by MD simulations [112]. Later on, Dai et al. developed their theoretical predictions on the thermal and elastic properties in the high entropy $(Ti_{0.2}Zr_{0.2}Hf_{0.2}Nb_{0.2}Ta_{0.2})B_2$ using MD simulations [113].

3.2. HT studies on functional properties of the HEMs

Before 2004, there were some reports on the HEAs showing their functional properties, where the earlier studies were chronically summarized [331]. Nowadays, Zhao concluded that most multi-functional materials were used in the thin film format [266]. For example, Li et al. fabricated the combinatorial thin-film libraries and the electrical-resistance measurement and its correlation with the glass-forming ability were done using the automatic four-point probes method [332]. Flores's group evaluated the microstructure and mechanical property variations in the Al_xCoCrFeNi HEAs fabricated by an HT laser deposition method [32]. These examples demonstrated that the thin-film-based combinatorial materials science approaches are extremely important for the discovery, research, and development of the HEMs.

Above all, the HT, combinatorial experiments are designed to quickly evaluate the materials properties. This approach uses materials libraries with composition gradients and rapid experimental techniques that can be automated, parallelized, and miniaturized. Such techniques are well established for functional materials. For example, Green et al. manifested that HT and combinatorial methodologies can characterize the electronic, magnetic, optical, and energy-related materials by the

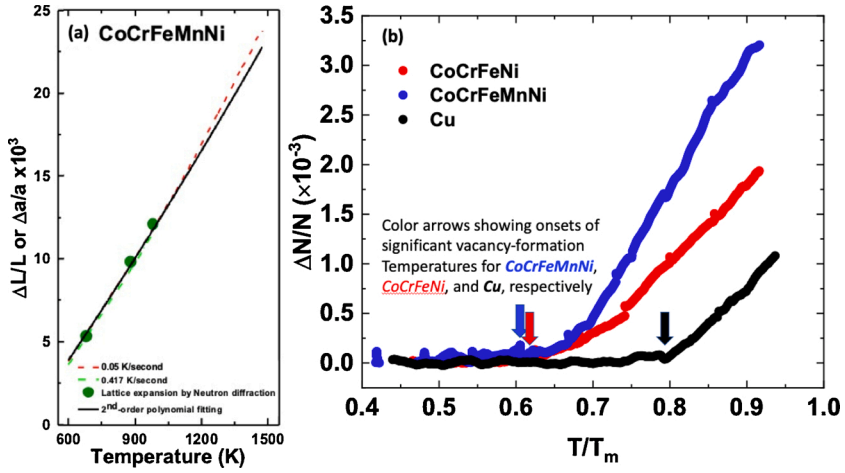

Fig. 20. (a) Measured strain versus temperature in the quasi-equilibrium and non-equilibrium states for the CoCrFeMnNi HEA. (b) X_v–homologous temperature (T/T_m) curves of Cu, CoCrFeNi, and CoCrFeMnNi in the quasi-equilibrium state. (Adapted from [242] with permission from Springer Nature).

synthesis of a "library" sample that contains the materials with the controlled variations of compositions [333]. Potyrailo and Takeuchi summarized novel measurement instrumentation, which was critical for characterization in combinatorial materials science as rapid and localized measurement schemes, resulting in massive data sets [334] for the combinatorial and high-throughput experimentation [335].

Meanwhile, there has been growing interest in developing high-entropy functional materials. Comparisons of functional properties between the HEMs and conventional low- and medium-entropy materials using computational modeling and tuning the composition of existing functional materials through substitutional or interstitial mixing were archived [336–339]. Gao et al. recapped the designing future of high-performance functional materials, such as the magnetic HEMs, which may possess an enhanced magnetocaloric effect (MCE) and potential thermoelectric materials [336].

Even for the functional properties, investigating the microstructures of the HEMs is still not trivial as it is highly associated with the desired properties. Therefore, in this session, we review the descriptors and the functional properties of the HEMs, such as the magnetic, electrical conductivity, superconductivity, thermoelectric, and magnetocaloric properties, which will be useful for the multi-functional HT examinations.

3.2.1. ML studies on phase predictions of the HEMs

From Liu et al.'s work, the magnetic properties of the $AlCoCuFeNi_x$ HEAs are dependent on the composition and phase structure. Other functional properties also highly depend on the combination of the composition and phase structure [266]. Hence, in this session, ML for phase prediction of the HEMs is reviewed.

Generally, there are four categories in configurational phases, i.e., solid solution (SS), intermetallic (IM), mixed SS and IM (SS + IM), and amorphous (AM) phases. Much research primarily aimed to discover the single-phase SS that has promising mechanical properties, such as increasing hardness and strength [340,341].

Troparevsky et al. proposed a model as the criteria to predict the formation of single-phase HEAs, which used HT computation of the enthalpies of formation of binary compounds based on DFT [126]. Lederer et al.'s HT *Ab-initio* approach, named as *Lederer-ToherVecchio-Curtarolo* (LTVC), can scan through many thousands of systems available in the AFLOW consortium repository [130]. Lederer et al's LTVC is corroborated by MC simulations for estimating the transition temperature of a SS. *Ab-initio* energies were incorporated into a mean-field statistical mechanical model where an order parameter followed the evolution of disorder [130]. Meanwhile, Lederer et al. found that there are cases in disagreement with the experiments or CALPHAD when the vibrational formation entropy or insufficient training data for cluster expansion was neglected in their HT *Ab-initio* approach. Lederer et al. concluded that sluggish kinetics was the bottleneck in achieving the equilibrium state, especially in measuring many transition temperatures precisely.

For the predictions of specific phases, such as the BCC and FCC, Pei et al. performed a support vector machine model to predict the stable HEAs from the composition space of 16 metallic elements, which was one order larger than the number of available experimental data [129]. There are 322 as-cast samples with a cross validation accuracy over 90 % after training and testing. Pei et al. anticipated there have 369 FCC and 267 BCC equiatomic HEAs. Eleven RHEAs agreed with recent experiments, and the 20 quinary ones with the highest melting temperatures are validated through first-principles calculations [129]. Pei et al.'s model was complementary to the calculation of phase diagrams and *Ab-initio* methods [129]. Li et al. built a SVM model with 322 as-cast HEAs and a cross validation accuracy over 90 % to forecast the FCC and BCC phases formation [129]. Among them, several RHEAs were screened out based on a high ratio of melting temperature to density. 11 of them complied with recent experiments and the 20 quinary HEAs were validated through first-principles calculations. Kostiuchenko and his teammates developed a novel ML-potential involving relaxation effects, called as low-rank potentials. In combination with MC simulations, the potentials are proved to reach high accuracy as cluster expansion techniques in studying the phase stability in the prototypical NbMoTaW HEA. Local relaxation effects were found to significantly stabilize single-phase formation of NbMoTaW to room temperature [131]. Meanwhile, Songa et al. proposed a method that combines electronegativity different, CALPHAD and ML to screen the high yield strength region in Co-Cr-Fe-Ni-Mo multi-component. SVMs model with trained data of CALPHAD calculations was established to predict the phase decomposition temperature for obtaining single-phase HEAs. Because the yield strength is positively related to the electronegativity difference, the compositions of HEAs with the phase decomposition temperature of 900 K and the maximum electronegativity are screened from the large amounts of high-throughput ML calculations. Moreover, Songa et al.'s results are validated by the experiments [342].

Since the IM was found to enhance functional applications via precipitate hardening, comprehensive studies on the IM have been conducted [89,343]. Islam et al.'s ML for phase selection in the HEAs employed a neural network in the ML framework to identify data patterns from an experimental dataset [127]. Islam et al. analyzed the correlations between the five features that lead to the phase selection in a dataset of 118 data of the HEAs and trained a NN model to classify the resulting phases based on the input features. They found a very high accuracy (> 99 %) in learning of the full dataset as well the most important factor is the VEC and the least important one is the mixing entropy. In addition, it is known that the amorphous phase exhibits great corrosion resistivity, and its crystalline structure and atomic-size distribution have been discussed through parametric studies [95,344].

On the other hand, eutectic or dual-phase HEAs were proposed as promising new classes of the HEAs owning high ductility-strength combination with the concept of combining soft FCC with hard BCC phases [1,345–347]. Therefore, efficiently predicting phases or structures, such as BCC, FCC, and hexagonal-close-packed (HCP) structures as well establishing links with compositions, is a pivotal step for screening a huge amount of the HEAs before further detailed characterization, and the implementation of ML can significantly achieve the goal. For example, Qu et al. [102] employed a SVM to build phase-predictive models (FCC, BCC, HCP, IM, or other phases) with both composition and thermodynamic parameters datasets (ΔH_{mix}, δ, $\Delta\chi$, and VEC). A dataset with 1348 data points has been established, which covers most of the HEAs families. The accuracies of both models were similar and above 85 %, and the gap were mainly caused by the IM-phase prediction. To be more specific, thermodynamic parameters have less effect on different SS-phases prediction. On the other hand, following Islam and Huang's work [127] with only 118 data points, Huang et al. [128] involved three different ML algorithms, namely, Fine and Weight KNN, SVM and ANN [unsupervised SOM method and supervised multi-layer feed-forward NN (MLFFNN)], to differentiate SS, IM, and SS + IM phases using 401 datasets. It was suggested that all the five input elemental features converted from compositions were mostly independent, among which δ and VEC were more crucial than the others. Due to the blurry boundary between the SS and SS + IM phases, direct ternary classifications could not reach high accuracy as MLFFNN displayed 74.3 % of highest accuracy among all models. For the local atomic behavior, which influences the HEMs, Kostiuchenko et al. employed ML potentials based on *Ab initio* data combined with MC simulations to investigate the phase stability, phase transitions, and chemical short-range order (SRO) in the BCC NbMoTaW HEA.

For the ML guided appraisal and exploration of phase design, Zhou et al. used one-dimensional (1D) convolutional neural network (CNN) and ANN [44]. Later, there are more and more investigations about complex phase predictions. For instance, Dixit and coworkers [133] implemented an ANN and unprecedentedly included processing routes, e.g., arc melting, injection-casting, and sputtering as an input feature apart from the conventional thermodynamic parameters. Given the total

input features, the proposed model can forecast all the coexisting phases, i.e., FCC, BCC, FCC1 + FCC2, BCC1 + BCC2, B2, Laves, C14 and Laves + Sigma, with 87.08 % accuracy. Lee et al.'s recent work [134] refined the NN into a deep learning-based phase predictor. To optimize hyper-parameters in the architecture, Bayesian optimization was applied, and a CGAN generates data to overcome the shortage of data. After adding augmented data, the performance of the model was largely elevated, reaching 93.17 % of accuracy. In addition, the deep learning-based NN permits the interpretability of design parameters. This work built a comprehensive guidance in the HEAs design, and most importantly, demonstrated the capability of generating similar and novel compositions via generative models.

As a framework of phase prediction via ML is gradually consolidated, research tends to uncover the relationships between microstructures and thermodynamic properties to reach higher predictability and interpretability. Some studies created novel thermodynamic parameters or physical parameters for training while others focused on feature engineering with rational selection of materials descriptors. There are several materials descriptors correlated with the HEMs. For example, Yang and Zhang proposed the parameters Ω and δ to anticipate the phase formation for the HEAs [98]. Yang and Zhang defined $\Omega \equiv {(T_m \times \Delta S_{mix})}/{|\Delta H_{mix}|}$ where ΔS_{mix} is the entropy of mixing, T_m is the mean melting temperature averaging from the principal elements, and ΔH_{mix} is the enthalpy of mixing. Yang and Zhang defined $\delta = \sqrt{\sum_{i=1}^{n} c_i\left(1 - r_i/\bar{r}\right)^2}$ where c_i is the atomic percentage of the i^{th} component, $\bar{r}$ is the average atomic radius, and r_i is the atomic radius, respectively [98]. Yang and Zhang indicated that the HEAs were stabilized as solid solution when $\Omega \geq 1.1$ and $\delta \leq 6.6\%$ [98]. Xie et al.'s MD simulation in the AlCoCrCuFeNi HEA thin film growth results [99] were in good agreement with Yang and Zhang's solid-solution formation rules [98]. VEC is another important parameter to predict the phase stability of the HEMs [132]. Guo et al. found that the stability of FCC and BCC HEAs was highly correlated with the VEC, that Chen et al. employed the VEC to design the HEAs with strength-ductility balance [348].

With these materials features and descriptors, Zhang et al. [115] employed feature selection and feature-variable transformation based on Kernel Principal Component Analysis (KPCA) in a four-phase prediction. It was found that the SVM model with four feature variables in KPCA led to the highest accuracy of 97.43 % for the classification of SS, AM, SS + IM, and IM. The investigation unprecedently included formation-enthalpies parameters extended from the Miedema theory [349], such as the mixing enthalpy of amorphous phase (H_{AM}), formation enthalpy of intermetallic compound phase (H_{IM}), and elastic energy of alloy (H_E). Pei et al. trained the ML model with 93 % accuracy for the single-phase prediction (FCC, BCC, and HCP groups) of the HEAs. The most important features such as melting point, molar volume, and bulk modulus were identified [47]. And a new thermodynamics-based rule was developed to predict solid–solution alloys although it was slightly less accurate (73 %). Zhang et al. [350] utilized a GA to rationally select a good combination of ML models and materials descriptors subsets from 14 empirical descriptors plus 56 self-defined descriptors, attaining an accuracy of 88.7 % in the SS/non-SS classification and an accuracy of 91.3 % in the BCC/FCC/Dual phase identification. Furthermore, they reported that the initial dataset of high classification uncertainties can improve their ML model, which demonstrated a successful active-learning approach. Kaufmann et al. employed a random forest model coupling with 108 compositional and 244 thermodynamic features to forecast the formation ability of SS including single- or multi-phase SS [199]. 13 most related features were extracted from the total of 352 features. The training data contained 134 equiatomic compositions from DFT calculations. The model predicted well the validation set for binary and ternary systems obtained from the CALPHA. However, the score for validation set of DFT-based LTVC was relatively low, attributed to the lack of training data for the ternary, quaternary, and quinary compositions. Notably, the uncertainty of the model can be known by the votes of each decision tree and the fractions of votes of each class. Recently, Machaka demonstrated a systemic framework of phase prediction, which was constructed by incorporating the six feature selection methods, features ensembles, and eight top-most identified classifiers. Machaka successfully forecasted five alloy systems for their phase transitions and phase stabilization [135]. Roy et al. applied a gradient boost regressor ML method and concluded that the mean melting point (T_m) and electronegativity difference as the most important descriptors have the strongest contributions to the phase formation in the low-, medium- and high-entropy alloys [123]. Dai et al. tried multiple algorithms and different features to achieve high accuracy for phase prediction with limited training dataset [136]. With feature engineering, over ten thousand descriptors could be constructed from 9 original features by four fundamental functions of $|x|^{1/2}$, x^2, x^3, $\log(1 + |x|)$ and by multiplying any 2 or 3 features. 9 most related features were selected for best representing the dataset. Interestingly, the constructed non-linear descriptors associated with logistic regression as a linear algorithm boosted the prediction performance of materials research.

3.2.2. Studies on magnetic and magnetocaloric properties of the HEMs

ML and HT examinations have been applied for the research of magnetic materials for years, as reviewed by Vasudevan et al. [93]. One of the highlights in Vasudevan et al's review is the generation and application of libraries from both experimental and theoretical tools. Frey et al.'s HT search discovered the magnetic and topological order in transition metal oxides where they calculated more than 27,000 unique magnetic orderings for more than 3000 transition metal oxides in the Materials Project database [351]. Choudhary et al.'s HT search for magnetic topological materials using spin-orbit spillage and ML [352]. Choudhary et al. also experimentally synthesized and characterized a few candidate materials, which supported their theoretical predictions [352]. Meanwhile, Ren et al. accelerated the discovery of metallic glass through the iteration of ML and HT experiments where they trained a ML model on previously reported observations and parameters from physiochemical theories. Ren et al. made their ML model become synthesis method-dependent to guide HT experiments in finding a new system of metallic glasses in the Co-V-Zr ternary [240]. Geng et al. demonstrated bulk combinatorial synthesis and HT characterization for the rapid assessment of magnetic materials, using the Laser Engineered Net Shaping (LENS™) methods [353].

There are several important characteristics for magnetic materials, namely, the coercivity and the energy product designated as BH_{max}. Soft magnets have low coercive fields and narrow hysteresis loops while hard magnets have higher coercive fields. Larger maximum energy products (BH_{max}, unit J/m^3) are desirable for hard magnets. The remanent induction, B_R, is the induction that remains when the field H is removed. The coercive field, H_c, is the field required to fully magnetize and demagnetize the materials.

For the HEMs, Gao et al. summarized the literatures reporting the magnetic properties, where the study of the magnetic properties of the HEAs aiming to reach high saturation magnetization (M_s) and low coercivity (H_c) [336]. Meanwhile, Gao et al. also pointed out that many functional materials have been studied, which satisfied the HEA definitions [336]. Table 7 summarizes the magnetic properties of the HEAs.

In Fig. 21, the measured magnetic properties of the selected HEAs (Table 7) are overlaid on a map of saturation magnetization versus coercivity for major conventional soft and semihard magnetic materials. It can be seen from Fig. 21 that compared to the traditional soft magnets, the HEAs have lower saturation magnetization and higher coercivity.

Using ML, Rickman et al. outlined several computational strategies to identify useful HEAs, including the HEAs for the magnetic applications [355]. Rickman et al. found that the SRO influenced the physical properties of the HEAs. More specifically, SRO dictated the magnetic

Table 7
Measured saturation magnetization (M_s, T) versus coercivity (H_c, A/m) for the HEAs reported in the literature [336,338,339].

Alloy	Structure	H_c (A/m)	M_s (T)
CoFeNi	FCC	121	1.606
CoFeNi	FCC	1,069	1.356
CoFeNi	FCC	189	1.671
CoCrFeNi	FCC	46	0.200
CoCrFeNi	FCC	1,252	0.144
CoFeMnNi	FCC	119	0.188
$Al_{0.25}CoCrFeNi$	FCC	356	0.151
$Al_{0.25}CoFeNi$	FCC	216	1.287
$Al_{0.25}CoFeMn_{0.25}Ni$	FCC	268	0.999
CoCrFeMnNi	FCC	13,980	0.951
CoCrFeMnNi	FCC	~0	0.328
CoCrFeMnNi	FCC	10,804	0.014
CoCrFeNiTi	FCC	11,900	0.220
CoCrFeNiTi	FCC	9,661	0.013
CoCrCuFeNi	FCC	13,210	0.559
$CoFeNiSi_{0.25}$	FCC	352	1.216
$CoFeNi(AlSi)_{0.1}$	FCC	1,089	1.287
$CoFeNi(AlSi)_{0.2}$	FCC	1,401	1.130
AlCoCrFeNi	BCC	4,138	0.546
$Al_{1.25}CoCrFeNi$	BCC	2,912	0.656
$Al_2CoCrFeNi$	BCC	188	0.267
$AlCoCrFeNb_{0.1}Ni$	BCC	4,615	0.422
$Al_{0.5}CoCrFeNi$	FCC + BCC	756	0.143
$Al_{0.75}CoCrFeNi$	FCC + BCC	363	0.087
$CoFeNi(AlCu)_{0.8}$	FCC + BCC	362	0.714
$CoFeNi(AlMn)_{0.5}$	FCC + BCC	730	0.482
$CoFeNi(AlMn)_{0.75}$	FCC + BCC	445	1.148
$CoFeNi(AlCu)_{0.8}Ga_{0.02}$	FCC + BCC	381	0.717
$CoFeNi(AlCu)_{0.8}Ga_{0.04}$	FCC + BCC	383	0.722
$CoFeNi(AlCu)_{0.8}Ga_{0.06}$	FCC + BCC	464	0.733
$CoFeNi(AlCu)_{0.8}Ga_{0.08}$	FCC + BCC	686	0.749
$Al_{0.5}CoFeNi$	FCC + BCC	343	0.992
$Al_{0.75}CoFeNi$	FCC + BCC	308	0.985
AlCoFeNi	FCC + BCC	224	0.846
$CoFeNi(AlSi)_{0.3}$	FCC + BCC	19,336	0.900
$CoFeNi(AlSi)_{0.4}$	FCC + BCC	17,963	0.904
$CoFeNi(AlSi)_{0.5}$	FCC + BCC	1,937	0.865
$CoFeNi(AlSi)_{0.8}$	FCC + BCC	5952	0.423
AlCoCrCuFeNi	FCC + BCC	3581	0.339
AlCoCrCuFeNi	FCC + BCC	1,194	0.143
CoFeGaMnNi	FCC + BCC	915	0.763
$CoFeNiSi_{0.5}$	FCC + Ni3Si	408	0.816
$CoFeNiSi_{0.75}$	FCC + Ni3Si	4,532	0.671
CrFeNiTi	FCC1 + FCC2 + σ	13,284	0.118
CrFeNiTi	FCC1 + FCC3 + σ	12,161	0.008
CrFeMnNiTi	FCC1 + FCC4 + σ	17,971	0.020
CrFeMnNiTi	FCC1 + FCC5 + σ	10,430	0.004
CoFeMnNiSn	L21 + BCC	3,431	0.797
AlCoFeMnNi	BCC + B2	629	1.260
$Fe_{40}Co_{35}Ni_5Al_5Cr_5Si_{10}$	BCC + B2	80	1.145
$AlCoCrFeNb_{0.25}Ni$	BCC1 + BCC2 + Laves	7,480	0.298
$AlCoCrFeNb_{0.5}Ni$	BCC1 + BCC3 + Laves	6,764	0.154
$AlCoCrFeNb_{0.75}Ni$	BCC1 + BCC4 + Laves	7,480	0.091
$Co_{26.7}Fe_{26.7}Ni_{26.6}Si_9B_{11}$	Amorphous	2	1.070
$B_{15}Co_{25}Fe_{25}Ni_{25}Si_{10}$	Amorphous	2	0.840
$B_{17.5}Co_{25}Fe_{25}Ni_{25}Si_{7.5}$	Amorphous	1	0.870
$B_{8.7}Co_{28.5}Fe_{26.7}Ni_{28.5}P_3Si_{4.6}$	Amorphous	4	1.070
FeNiGaMnSi	BCC	232	0.431
CoCrFeNiCu	FCC	2,627	0.291

properties, electronic transport, and deformation mechanics of the HEMs [355].

For the combinatorial assessment of the HEMs, Borkar et al. examined the composition-microstructure-microhardness-magnetic property relationships, using the laser-deposited compositionally-graded $Al_xCrCuFeNi_2$ where $0 < x < 1.5$ [356]. Specifically, for the FeMnCoCrAl HEA system, Marshal et al. developed thin-film libraries for the combinatorial evaluation of the phase formation and magnetic properties [138]. Marshal et al. systematically investigated using the conventional XRD and spatially-resolved atom probe tomography as characterization techniques as well as DFT [138]. Marshal et al. found that the BCC structure was formed with an addition of Al, exhibiting a soft ferromagnetic behavior. Further increase in the non-ferromagnetic Al content beyond 8 wt. % decreased the overall Ms because of the substitution of ferromagnetic species by the paramagnetic Al, which also induced lattice distortions. Marshal et al.'s measured the trend of the Al concentration-induced reduction in magnetization, which was in agreement with their DFT predictions [138].

Compared with the traditional commercial magnetic materials, the magnetic properties of HEAs are mostly located between semi-hard magnetic and soft magnetic regions. As Gao et al. pointed out that the magnetic HEMs may possess an enhanced MCE as potential thermoelectric materials [336].

With the assistance of ML, there are several new materials with better magnetocaloric. Holleis et al. demonstrated the ML-guided design of single-molecule magnets for magnetocaloric applications [357]. Castro et al. showed the ML-guided discovery of the gigantic MCE in HoB_2 near the hydrogen-liquefaction temperature [358]. Zhang and Xu reported that they tuned the MCE, represented by the maximum magnetic entropy change (MMEC), in manganites from compositions and structural parameters via ML [359]. Zhang and Xu screened more than 70 lattices, cubic, pseudocubic, orthorhombic, and rhombohedral, with the MMEC ranging from 0.65 J-kg^{-1} K^{-1} to 8.00 J-kg^{-1} K^{-1} under a field change of 5 T [359].

For the HEMs, Perrin et al. reported the role of compositional tuning of the distributed exchange on the magnetocaloric properties in the HEAs [360]. Yuan et al. demonstrated the rare-earth HEAs with giant MCE [361]. Law et al. enhanced the MCE by the magneto-structural phase transition [362]. Following is an example of the high-entropy bulk metallic glasses (HE-BMGs), which maximize large magnetic entropy changes (ΔS_M). Huo et al. developed the HE-BMGs for their wider ΔS_M peak, and thus, larger refrigerant capacity [363]. Huo et al. demonstrated that the HE-BMGs are the potential candidates for magnetic refrigerants working in a helium and hydrogen-liquefaction temperature range [363]. To characterize the MCE, the ΔS_M can be estimated as below.

$$\Delta S_M(T,H) = \int_{H_{\min}}^{H_{\max}} \left(\frac{\partial M}{\partial T}\right)_H dH \tag{19}$$

where H_{min} and H_{max} represent the initial and final values of the magnetic field, respectively. Huo et al. set $H_{min} = 0$ and $H_{max} = 5$ T [363]. The peak magnetic entropy changes $\left(\Delta S_M^{pk}\right)$ in the HE-BMGs are shown in Fig. 22.

3.2.3. Studies on thermal, electrical, thermoelectric conductivities and superconductivity

Thermal, electrical, thermoelectric conductivities, and superconductivity are the important functional properties. Hence, there are many new materials systems developed by coupling the ML and HT methods. The electrical resistivity of alloys is principally controlled by electron-electron interactions, magnetic effects, and phonon at temperatures in the range of 4 ~ 300 K, and solely by phonon at temperatures in 300 ~ 400 K. The phonon contribution to thermal conductivity actually is comparable with the electronic contribution [368]. For thermal conductivity, Juneja et al. predicted the lattice thermal conductivity by coupling the HT property map and ML [369]. Chen et al. built a ML-based model using a benchmark data set of experimentally measured 100 inorganic materials [370]. Chen et al. considered 61 features, which belonged to the three distinct categories, i.e., elemental, structural, and pertaining to valence electrons. Chen et al. found that the key features governing the thermal-transport behaviors in non-metals are the specific bulk modulus and bond length [370]. For the semiconductors, Carrete et al. revealed an unprecedented discovery of low-thermal-conductivity half-Heusler semiconductors via HT materials modeling [371] in the AFLOWLIB.org database [60,202]. For the high-temperature solid

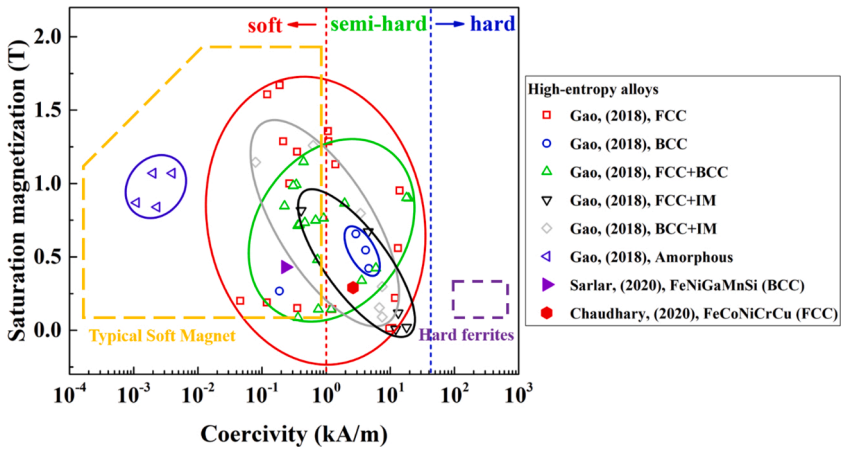

Fig. 21. Measured saturation magnetization versus coercivity in the HEAs with the structures of FCC, BCC, FCC + BCC, FCC + IM, BCC + IM, and AM, compared with major conventional soft (marked in the dashed yellow lines) and hard magnetic materials (marked in the dashed purple lines). (Adapted from [354] with permission from MDPI) (For interpretation of the references to colour in this figure legend, the reader is referred to the web version of this article.).

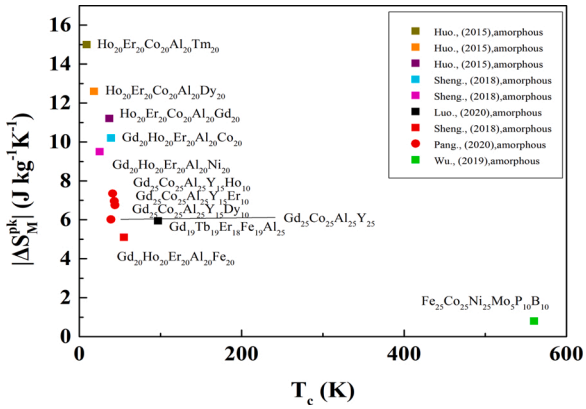

Fig. 22. Peak magnetic-entropy change, ΔS_M^{pk} (J. kg^{-1}. K^{-1}), of the HE-BMGs (Data taken from [363–367]).

phases, Roekeghem et al. used finite-temperature phonon calculations and ML methods to estimate the mechanical stability of approximately 400 semiconducting oxides and fluorides with cubic perovskite structures at different temperatures [372]. Roekeghem et al. also screened for materials exhibiting negative thermal expansion [372].

Schütt et al. demonstrated a ML approach for fast prediction of the electronic properties [373]. Schütt et al. employed local spin-density approximation calculations as a training set. Schütt et al. focused on predicting the value of the density of electronic states at the Fermi energy. Schütt et al. found that conventional representations of the input data, such as the Coulomb matrix, is not suitable for the training of learning machines in the case of periodic solids [373]. To understand the behavior of dielectric insulators experiencing extreme electric fields, Kim et al. used advanced statistical or ML schemes to obtain predictive phenomenological models of dielectric breakdown and found analytical relationships between the breakdown field and material properties, such as band gap and phonon-cutoff frequency [374]. For the electrical conductivity, Chen et al. developed a small set of ML algorithms [375], which was used to investigate the electrical properties of the materials for future applications, such as for neuromorphic computing [376]. Islam et al. showed that emerging non-volatile memory devices that exhibit gradual changes in resistivity are a key enabler of in-memory computing, which is a type of neuromorphic computing [376].

For the thermal and electrical conductivity, Oliynyk et al. trained a ML model to discover the Heusler compounds. Compared to the other approaches, Oliynyk et al.'s HT ML-driven synthesis made faster and more reliable predictions of the occurrence of Heusler vs. non-Heusler compounds for an arbitrary combination of elements with no structural input on over 400,000 candidates [377]. Gaultois et al. employed ML to guide an experimentally new compound ($Er_{12}Co_5Bi/Gd_{12}Co_5Bi$) for thermoelectric materials, which possessed low thermal and high electrical conductivities, but modest Seebeck coefficient [377]. Notably, the rare-earth family compound is quite distinct from the known thermoelectrics, but exhibits similar structures with the known thermoelectrics. In addition, a positive temperature dependence of the thermal diffusivity is found for these compounds, which was rarely obtained before.

The Wiedemann-Franz law examine the thermal and electrical conductivities by comparing the ratio of the electronic contribution of the thermal conductivity to the electrical conductivity of a metal as a function of temperature, as presented in the following Equation.

$$\kappa = \kappa_e + \kappa_{ph} = L\sigma T = \left(L_e + L_{ph}\right)\sigma T \tag{20}$$

where T is the temperature, κ is the thermal conductivity, L_e is the Lorenz number, and σ is the electrical conductivity.

A four-point probe method is used to measure the electrical resistance. Huxtable et al. demonstrated the thermal conductivity imaging at a micrometre-scale resolution for combinatorial studies of materials [378]. Thermal diffusivity is determined by means of the laser-flash method [379]. Meanwhile, the differential scanning calorimeter (DSC) is used to measure the variation of heat capacity with temperature. Thus, the thermal conductivity (κ) is calculated, as shown below.

$$\kappa(T) = \alpha(T) \times S(T) \times \rho(T) \tag{21}$$

where T is the temperature; $\kappa(T)$ is thermal conductivity, $\alpha(T)$ is thermal diffusion coefficient, $S(T)$ is the specific heat, and $\rho(T)$ is the density.

Fig. 23 depicts the thermal conductivity and electrical resistivity for different materials, and the dashed line indicates that the HEAs also follow the Wiedemann–Franz law. Due to the obvious diffuse reflection effect, the HEAs have lower thermal conductivity and electrical conductivity than the traditional alloys [380].

To apply the HEMs for the applications of thermoelectric technologies, Wei et al. recapped the thermodynamic routes showing the ultra-low thermal conductivity and high thermoelectric performance [383]. In search of thermoelectric materials with high conversion efficiency, the dimensionless TE figure-of-merit, zT, has been used to estimate the performance, defined as follows.

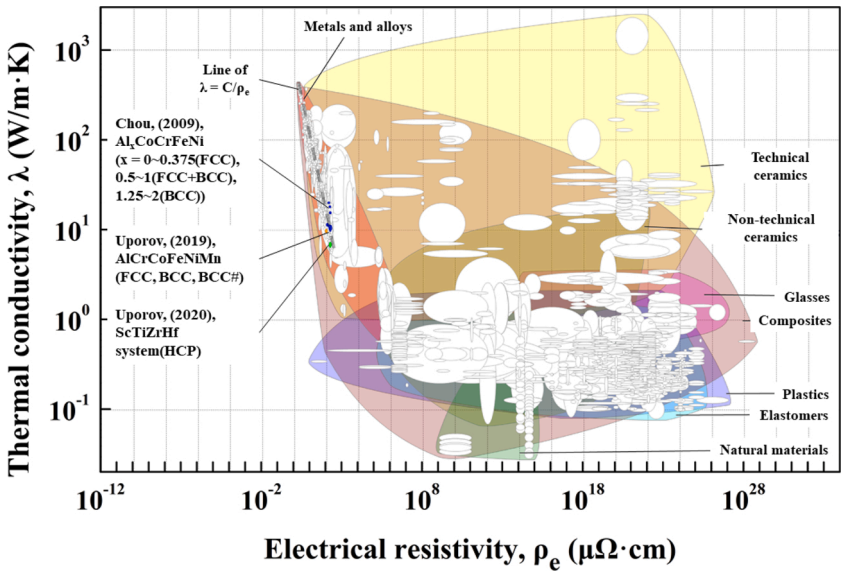

Fig. 23. Thermal conductivity and electrical resistivity for various materials, the dash line representing the Wiedemann-Franz relationship (Data taken from [322,368,381,382]). The data is from the CES EduPack 2018, Granta Design, Limited, Cambridge, UK, 2018. (The data taken from ML is from [377]).

$$\kappa_z T = \frac{S^2\sigma}{k_{total}} T \tag{22}$$

where S is the Seebeck coefficient, σ is the electrical conductivity, and k_{total} is the total thermal conductivity. The temperature dependencies of the Seebeck coefficients from the selected HEMs are shown in Fig. 24. The results show that by increasing the manganese (Mn) content, there is a higher Seebeck coefficient and lower electrical conductivity through the cocktail effect in the HEMs. Due to the reason that conventional TE device suffer from high cost for fabrication, spin-driven thermoelectric (STE) phenomena provides an alternative solution to this problem. Unfortunately, the understanding of the fundamental mechanism and the material parameters is still lacking. Iwasaki et al. employed the combination method of ML and HT experiments to develop a better STE material. The obtained $Fe_{0.665}Pt_{0.27}Sm_{0.065}$ achieved 11.12 μV/K [384].

From Yuan et al.'s review on the advances in the HT superconductivity research, the HT computation, synthesis, characterization, and the emerging field of ML for materials were presented [387]. For example, Stanev et al. developed several ML schemes to model the critical temperature (T_c) of the 12,000 + known superconductors available via the SuperCon database and investigate the chemical/structural properties of materials [388]. Stanev et al. divided superconductivity materials into two classes based on their T_c values, above and below 10 K. Stanev et al. used materials data from the AFLOW Online Repositories [60,202] and searched for the entire Inorganic Crystallographic Structure Database (ICSD) for new potential superconductors, in which Stanev et al. identified > 30 non-cuprate and non-iron-based oxides as candidate materials [388]. Matsumoto *et al.* used the random forest regression model to establish a T_c prediction model for searching superconductors with higher T_c [389]. The versatility of the model enables to predict well the Mg-B-Ti system and Fe-Te-Se system despite the lack of Fe-based superconductors in the training data. The Ca-B-C system with the highest T_c (36 K) was forecasted by the model. It is suggested that a higher T_c superconductor could be found in a quaternary or a five-element system as the training model including cuprate and Fe-based superconductors.

To investigate the superconductivity property of the HEMs, Marik et al. prepared a single-phase polycrystalline $Nb_{21}Re_{16}Zr_{20}Hf_{23}Ti_{20}$ HEA material [390]. Quasi-static (DC) magnetization, ac susceptibility, electrical, and specific heat measurements were performed, using a Magnetic Properties Measurement System (MPMS) and Physical Property Measurement System (PPMS). The effective Fermi temperature (T_F) is obtained by the following Equation.

$$k_B T_F = \frac{\hbar^2}{2}(3\pi^2)^{2/3}\frac{n^{2/3}}{m^*} \tag{23}$$

where k_B is the Boltzmann constant, T_F is the Fermi temperature, $\hbar$ is the Dirac constant, n is the quasiparticle number density per unit volume, and m^* is the effective mass of quasiparticles [391].

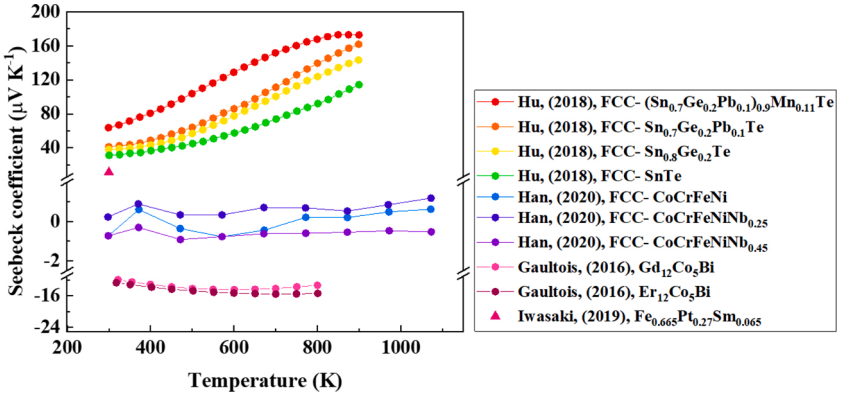

Fig. 24. Temperature dependencies of the Seebeck coefficients in the HEAs. (Data taken from [385,386]).

Fig. 25 depicts the superconducting transition temperature (T_c) vs. the effective Fermi temperature (T_F). The $Nb_{21}Re_{16}Zr_{20}Hf_{23}Ti_{20}$ HEA is shown as a solid red star with T_F of 10,091 K. The results suggest that the $Nb_{21}Re_{16}Zr_{20}Hf_{23}Ti_{20}$ HEA belongs to a type-II superconductor, which exhibits an intermediate phase of the mixed ordinary and superconducting properties at intermediate temperatures [392]. Compared to the other systems, the superconducting transition critical temperature of HEAs is relatively low. The superconductivity of the HEMs may appear only subjected to extreme environments. Most HEMs with superconductivity have transition elements, such as Re and Ta. The critical temperatures of these systems are below 10 K as non-traditional superconductors [390,391,393].

3.3. HT studies on properties depending on both compositions and microstructures

Referring to Miracle and Senkov's conclusion on the HEAs and related concepts of MPEAs [1], the structural properties of HEMs depend on both compositions and microstructures [33]. Moreover, the structural properties have dramatic scaling effects [396]. Since the microstructures and length scales are major barriers for the HT examinations on the structural properties, mainly the mechanical behaviors of the HEMs, it is not as trivial as the applications of the HT examinations on the functional HEMs. Therefore, in this section, we introduced a few examples of the HT studies on the mechanical properties in the HEMs. Major efforts are to summarize the mechanical behaviors and the associated microstructures of the HEMs.

3.3.1. ML and HT studies on mechanical properties of the HEMs

Although many efforts have been primarily dedicated to the phase selection with an informatics-based approach, several researchers have applied ML and HT techniques to mechanical-properties predictions, particularly hardness and YS. For example, Coury et al. reported an "Effective Atomic Radii for Strength" (EARS) methodology, together with different semi-empirical and first-principle models, and they predicted the extent of SS strengthening to design new $Cr_{45}Ni_{27.5}Co_{27.5}$ HEAs owning a YS over 50 % greater associated with equivalent ductility than the strong HEA ($Cr_{33.3}Ni_{33.3}Co_{33.3}$) from the CrMnFeNiCo family [48]. Meanwhile, Cheng et al. propose a machine model to extract important features, which influence SS strengthening of the HEAs. Cheng et al. propose a new model with feature of electronegativity difference that fit the hardness data better than the other models which were mainly based on the mismatches of the atomic sizes and the differences between the moduli. Cheng et al. introduced the mixing enthalpy to improve the predictions of the single-phase HEAs hardness in an error rate of 13.8 % [397]. Moreover, Coury et al. developed a HT nanoidentation for yield-stress estimations of single-phase HEAs within an approximately error of 10 %, which was successfully applied to a compositionally-graded region of a diffusion multiple [238]. Coury et al.'s experimental and complimentary simulation results indicated that the strength was maximized when the atomic-size mismatch was maximized in their systems, including $Cr_{19}Mn_{20}Fe_{16}Co_{23}Ni_{23}$, $Cr_{27}Mn_4Fe_2Co_{34}Ni_{33}$, $Cr_1Mn_{24}Fe_{26}Co_{24}Ni_{25}$, $Cr_1Mn_2Fe_1Co_{47}Ni_{49}$, $Cr_{33.3}Fe_{10}Co_{28.3}Ni_{28.3}$, $Cr_{25}Co_{37.5}Ni_{37.5}$, $Cr_{33.3}Co_{33.3}Ni_{33.3}$, $Cr_{33.3}Fe_{10}Co_{28.3}Ni_{28.3}$, $Cr_{33.3}Mn_{10}Co_{28.3}Ni_{28.3}$, $Cr_{45}Co_{27.5}Ni_{27.5}$, $Cr_{20}Mn_{20}Fe_{20}Co_{20}Ni_{20}$, $Mn_{25}Fe_{25}Co_{25}Ni_{25}$, and $Cr_{33.3}Co_{33.3}Ni_{33.3}$, $Co_{50}Ni_{50}$ [238].

To design light and strong HEAs, Menou et al. [132] conducted the computational method by a multi-objective optimization genetic algorithm combining a data-mining method using (1) phase calculations through the CALPHAD method to estimate the probability of forming a single SS, (2) physical models to predict the solid solution hardening (SSH) contribution and crystal structures of multi-concentrated alloys, and (3) a mixture rule for the density estimation to design HEAs with high specific strengths. The method led to the design of 3155 compositions, which simultaneously had a higher probability to form a BCC single solid solution structure, a higher SSH, and a lower density, so-called Pareto-optimal. A new HEA of $Al_{35}Cr_{35}Mn_8Mo_5Ti_{17}$ was selected and fabricated, reaching an actual composition of $Al_{31}Cr_{37}Mn_7Mo_6Ti_{19}$. The measurement result of the HEAs is one of the hardest (658 HV) metallic alloys ever recorded for such a low density (5.5 g/cm^3). Moreover, they also proposed the same strategy to explore the strong and stable FCC HEA [188]. More than 2000 compositions are produced with the optimization strategy. The optimized FCC alloy, $Al_{10}Co_{17}Fe_{34}Mo_5Ni_{34}$, is selected to fabricate by vacuum arc melting for validation. The experiment results disclosed that the Vickers hardness of 1.78 GPa, a yield stress of 215 MPa, and an ultimate tensile strength of 665 MPa in the annealed state are superior to the existing FCC HEAs with comparable density. Menou et al.'s data-driven method can be further implemented for including more criteria, such as the elastic modulus, cost, and melting temperature, etc.

Similarly, Xiong and coworkers [398] proposed a two-objective regression model predicting hardness and compressive yield stress, the correlation coefficient of which were both higher than 0.905. These studies demonstrated the predictability of ML on different mechanical properties. Followed by Rickman's previous endeavors in materials data analytics in conjunction with a visualization strategy, known as parallel coordinates [399], they successfully screened and generated virtual HEAs having high hardness in excess of 1000 HV via the combination of the canonical correlation analysis (CCAA) and GA optimization strategy with a CCAA-recommended fitness function [39]. The fitness function governed GA in finding candidates that are 5-element alloys from 16 elements and 16 M compositions per element, in certain regions. Finally, the model was validated by seven candidates synthesized and characterized, compared with the predictive hardness. In 2020, Rickman et al. reviewed several novel ML applications for HEAs on top of his previous work [400]. Within the cuckoo search, another nature-inspired

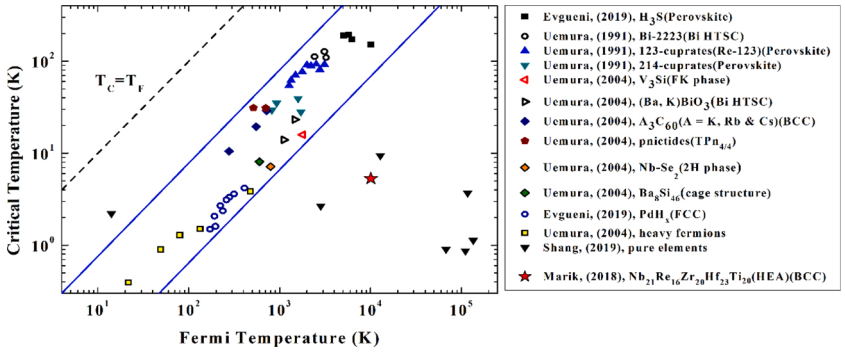

Fig. 25. The superconducting transition temperature, T_c, vs. the effective Fermi temperature, T_F, where the $Nb_{21}Re_{16}Zr_{20}Hf_{23}Ti_{20}$ HEA is shown as a solid red star. Other data points plotted between the blue solid lines are different families of unconventional superconductors. (Data taken from [390,391,393–395]) (For interpretation of the references to colour in this figure legend, the reader is referred to the web version of this article.).

algorithm was proposed to deal with optimization problems. It was coupled with MD to maximize the ultimate tensile strength in the Al-Cr-Co-Fe-Ni quinary alloy system, and the improvement on this algorithm accelerating convergence was also discussed. Bhandari et al. [401] established the ANN model for the prediction of the Vickers hardness of RHEAs. Through the features selection, the predicted hardness of 695 HV from the ANN model was consistent with the experiment of 601 HV for $C_{0.1}Cr_3Mo_{11.9}Nb_{20}Re_{15}Ta_{30}W_{20}$, which is less than 15 % error. Since the training sets include little dataset (128 samples) and several elements (17 elements), the prediction error is diverged and ranged from 0.99 % ~ 49.2 %. As the volume fraction and size of precipitate play dominant roles in precipitation strengthening, Zheng et al. [402] developed the ANN model to hasten the exploration of ultra-strong nanoprecipitated HEAs. The volume fraction of the γ′ phase was selected as the primary target in ANN model, while the YS played an assistance factor. Note that the training data only include the nickel-based superalloys. The predicted volume fractions are in good agreement with target values for the testing database of HEAs. In this work, a novel $Ni_{32}Co_{28}Fe_{28}Cr_3Al_3Ti_6$ (wt. %) aged HEA with volume fractions of 50.4 % and yielding strength of 1.03 GPa was obtained by ML HT screening among 102,213 compositions. Prestrain aging was further performed to enhance the YS, UTS, and elongation to 1.31 GPa, 1.65 GPa, and 15 %, respectively.

Besides exploring new compositions with better mechanical properties, the efforts are also put forth in reasoning the relationships among the discovery of the property, structure, and composition. Wen et al. [180] demonstrated a systematic framework combining ML and design of experiments to find the HEAs with high hardness in the Al-Co-Cr-Cu-Fe-Ni system. They first trained a surrogate model learning the property-composition relationships and predicted nearly two-million pseudo compositions in a virtual space. As a utility function was used to guide the search for high hardness, some alloys would be selected to synthesize and add to the dataset. After seven iterations, the active learning with experiments led to several HEAs with hardness 10 % higher than the maximum value (775 HV) in the original training data. They even found that the two alloys with the highest hardness have more Al and little Cu. When combined with Ni, Al tends to form a BCC ordered phase (B2). Therefore, when the Al content increases, the solid solution would transform from the FCC to BCC, and to B2 phase. Chang et al. [21] utilized simulation annealing to search for the Al-Co-Cr-Fe-Mn-Ni HEA with high hardness. These efforts reveal the importance of Co, Cr, and Al for future HEMs design. Al is considered as the main contribution to the hardness. These optimization methods accelerate the HEMs discovery and help scientists gain insights from the results, which is the key of materials informatics-explainable and interpretable ML models. Xiong et al. employed random forest classifier to classify the phases as well random forest regression model to predict the hardness and UTS in the HEAs [403]. The 5 most related features are identified from the 30 selected features for the predictions of phase, hardness, and YTS in the HEAs. Shapley additive explanation (SHAP) method is adopted to calculate the contribution of features, which quantitatively gives a contribution value of features to the mechanical properties. Thereby it provides a straightforward assessment in the design of HEAs. Roy et al. [79] reviewed the pipeline construction of ML and data-driven exploration of the HEAs with emphasis on feature selection and role of feature descriptors. Physical quantities such as melting temperature and Young's modulus are suitable for predicting the mechanical properties while chemical composition and environmental factors are included in the oxidation resistance and corrosion rates prediction. Kimenko et al. [404] applied ML approach to forecast the YS of the Al-Cr-Nb-Ti-V-Zr system at various temperatures. The models showed satisfactory accuracy prediction, particularly with small size of training dataset. To uncover the relationship between elements and solidification interval characteristics, Qiao et al. [405] applied a fuzzy neural network (FNN) model to design novel HEAs in the Fe-Cr-Ni-Al system. Finding that the elemental fractions of Cr and Al are more sensitive to mechanical performance, compositions with the narrowest solidification interval (calculated from CALPHAD) were predicted by FNN model and prepared by experiment. The $FeCrNiAl_{0.8}$ exhibits high fracture strength and plastic strain of 2839 MPa and 41 %, respectively, with high work hardening capacity. The strategy provides an alternative way to design the advanced HEAs with superior mechanical properties. Li et al. integrated the atomic simulation (MD), the physical model (Hall-Petch relationship), and the machine learning model (ANN) as an active learning process to find the optimal grain size of CrCoFeNi HEAs with heterogeneous grain structures for high strength [405]. ML uncovers the grain size of 38.4 nm at a large grain size of 165 nm in the CrCoFeNi HEAs possessing a highest yield strength. The results agree well with those obtained by MD simulation. The design workflow can be further applied to explore the other materials with the desired performance. More recently, Li et al. [406] employed MD with SNAPs to simulate the refractory NbMoTaW with respect to single crystal and polycrystalline HEAs. They found that the edge dislocations were more important in the HEAs than in the individual pure BCC metal, and Nb segregation to grain boundaries enhanced the observed SRO. Nb enrichment stabilizes the grain boundaries and leads to higher strength. Thereby, tailoring grain boundary composition and SRO is critical to designing the HEAs with great mechanical properties. Fig. 26 describes the grain size effects on the YS and UTS. There is a clear gap between the ML-designed HEA with heterogeneous grain structures [407] and the HEAs mainly with mono-dispersed grain size [408–412], which is marked as the symbol of ⋆. Such a difference demonstrates that with the applications of the hierarchical structure and heterogeneous grain structure, the ML approach will open more possibility for the microstructure design of the HEMs.

In summary, ML has shown the ability to effectively predict the compositions and phase constitutions of the HEAs. While reducing the endless number of compositions in the design of HEAs to mere hundreds, big data analysis can further improve the process by observing the statistical distributions and trends to obtain an insight of which element playing a critical role in the phase constitution. As a result, the process of designing HEAs can be accelerated systematically. Moreover, for the complicated structures, such as simultaneously tailoring both the hierarchical microstructure and heterogeneous grain structure, ML can shed light on possible direction, which is not feasible for the trial-and-error process.

3.3.2. *Phase stability in the HEAs*

The importance of the phase in the HEMs is evidenced in Table 8, where the phase prediction is the most frequent research topic [44,102,115,123,126–137]. The phase formation for the functional properties in the HEMs is reviewed in the earlier session. Herein, the review focuses on the mechanical properties in terms of the phase formation and phase stability. Phase formation and the distribution of the microstructural features in the HEMs dramatically change the mechanical properties of the HEMs. For example, Wu et al. investigated the mechanisms of eutectic formation (FCC/L12 + BCC/B2) in the HEAs [137]. Wu et al. discovered that Al is the most critical element while Cr is strongly associated with Al in the Al-Co-Cr-Fe-Ni system. This target-oriented systematic ML design is useful to develop the eutectic HEAs (EHEAs). Wu et al. demonstrated how to untangle the elemental relationships in the complex systems and matched with the microstructures. Wu et al.'s EHEAs has the UTS of ~ 1300 MPa and total elongation of ~ 20 %.

Meanwhile, another critical issue for the HEMs is their phase stability. HEMs do not simply inherit the structures and properties of their constituent elements, as expected with a "linear effect". The high chemical complexity and packing disorder cause severe local lattice distortion, which could further stabilize the HEAs kinetically. Therefore, HEMs might exhibit rich tunable behaviors under high pressures [425,426]. For example, the structural stability of various HEA systems has been explored, using *in-situ* high-pressure synchrotron radiation-based XRD techniques showing a transformation from FCC to HCP phases in

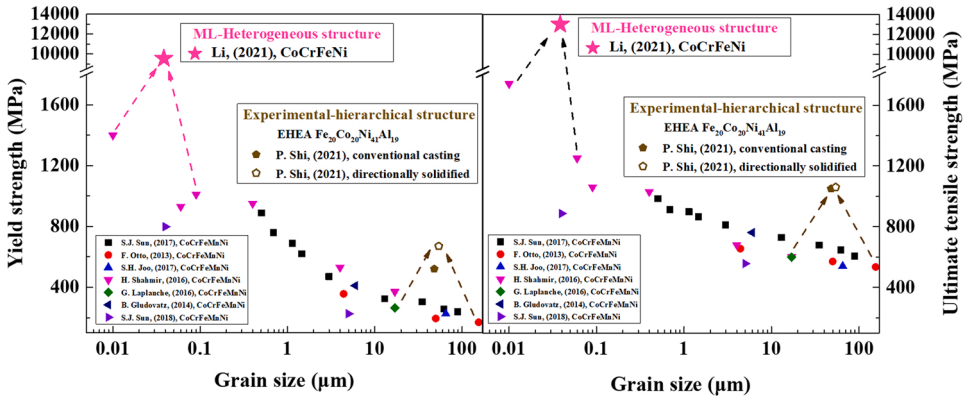

Fig. 26. Grain size effect on (a) yield strength and (b) ultimate tensile strength in the HEAs. (Data taken from ML-designed HEA, marked as the symbol of ★, with heterogeneous grain structures [407] and the others [408–413]).

Table 8
A comparison of elongation and ultimate tensile strength in different types of the as-cast HEAs [137,414–419].

	Yield Strength (MPa)	Ultimate Tensile Strength (MPa)	Elongation (%)	Type	Phase	Ref	Remarks: with ML, without ML, with ML and verified by experiments
$Ni_{30}Co_{30}Fe_{10}Cr_{10}Al_{18}W_2$	–	1,266	20	EHEA	FCC + BCC		With ML and verified by experiment
$Ni_{36}Co_{24}Fe_{10}Cr_{10}Al_{18}W_2$	–	1,316	20	EHEA	FCC + BCC	[137]	With ML and verified by experiment
$Ni_{40}Co_{20}Fe_{10}Cr_{10}Al_{18}W_2$	–	1,344	21	EHEA	FCC + BCC		With ML and verified by experiment
$AlCoCrFeNi_{2.1}$	–	1,100	18	EHEA	FCC + BCC	[414]	Without ML
$AlCrFe_2Ni_2$	780	1,228	17	EHEA	FCC + BCC	[415]	Without ML
$Fe_{20}Co_{20}Ni_{41}Al_{19}$	577	1,103	19	EHEA	FCC + BCC	[416]	Without ML
$CrFeNi_2Al$	774	1,357	6	Primary BCC + FCC	FCC + BCC		Without ML
$CrFeNi_{2.1}Al_{0.9}$	610	1,173	9	Primary BCC + FCC	FCC + BCC		Without ML
$CrFeNi_{2.2}Al_{0.8}$	479	956	13	EHEA	FCC + BCC	[417]	Without ML
$CrFeNi_{2.3}Al_{0.7}$	461	835	30	Primary FCC + BCC	FCC + BCC		Without ML
$CrFeNi_{2.4}Al_{0.6}$	441	757	45	Primary FCC + BCC	FCC + BCC		Without ML
$(FeCoNiCrMn)_{91}Al_9$	332	728	30	Primary FCC + BCC	FCC + BCC		Without ML
$(FeCoNiCrMn)_{90}Al_{10}$	528	1,000	16	Primary FCC + BCC	FCC + BCC	[418]	Without ML
$(FeCoNiCrMn)_{89}Al_{11}$	832	1,174	8	Primary BCC + FCC	FCC + BCC		Without ML
$CoCrFeNiNb_{0.103}$	317	622	19	FCC + Laves	FCC + IM		Without ML
$CoCrFeNiNb_{0.155}$	321	744	21	FCC + Laves	FCC + IM		Without ML
$CoCrFeNiNb_{0.206}$	402	807	9	FCC + Laves	FCC + IM	[419]	Without ML
$CoCrFeNiNb_{0.309}$	478	879	4	FCC + Laves	FCC + IM		Without ML
$CoCrFeNiNb_{0.412}$	637	1,004	1	FCC + Laves	FCC + IM		Without ML
$Al_{10}Hf_{25}Nb_5Sc_{10}Ti_{25}Zr_{25}$	500	900	4.2	Primary BCC + Orthorhombic	Primary BCC + Orthorhombic	[420]	Without ML
$Ni_{40}Fe_{30}Co_{20}Al_{10}$	337	670	49.9	FCC	FCC	[421]	Without ML
$Al_4Mo_4Nb_8Ti_{50}Zr_{34}$	825	825	11.0	BCC	BCC	[422]	Without ML
$Ti_{38}V_{15}Nb_{23}Hf_{24}$	774	792	20.6	Primary BCC + BCT	Primary BCC + BCT	[423]	Without ML
$Ti_{25}V_{25}Nb_{25}Hf_{25}$	1004	–	16.1	–	–		Without ML
$Ti_{60}AlCrVNb$	960	–	28	BCC	BCC	[423]	Without ML
$Fe_{40.2}Ni_{11.3}Mn_{30}Al_{7.5}Cr_{11}$	593		22	BCC + FCC/B2	BCC + FCC/B2	[424]	Without ML
$Cr_{45}Co_{27.5}Ni_{27.5}$	≈340	x	≈50		FCC + SIGMA	[48]	With theoretical model, and verified by experiment

the CoCrFeMnNi HEAs [289–291,427]. A similar FCC-to-HCP phase transformation was demonstrated in ternary and quaternary equiatomic FCC-structured alloys, such as CoCrNi and CoCrFeNi alloys [427]. However, some FCC-structured HEAs did not exhibit phase transition even under extreme high-pressure compression, such as CoCrFeCuNi, NiCoCrFePd, $Al_{0.3}$CoCrFeNi, and AlCoCrCuFeNi alloys [427–430]. Surprisingly, some experiments concluded no phase transformation observed in the CoCrFeMnNi HEA even the compression pressure increasing up to 49 GPa [428,431]. These results implied that the phase-transformation mechanism in these FCC-structured HEAs is not yet known in detail while many polymorphic transitions have been discovered, as summarized by Zhang et al. [426]. There are three possible mechanisms to interpret the differences among these cases [289–291,427–431], and Zhang et al. [432] indicated the hydrostaticity effects of pressure-transmitting media and grain size effects of the inconsistency of the onset pressure-induced phase transformation among high pressure studies [1,35,290,427,432,433]. From Huang et al.'s results, as shown in Fig. 27, another possibility was that the local heterogeneity in the HEMs may induce the temporal shear between the transmitting medium and the HEMs, which induced the shear deformation during deformation.

Similar shear-induced phase transformation was also observed by Niu et al. where Niu et al.'s tensile experiment and MD simulation demonstrated the deformation paths of the stacking faults and twins inducing the subsequent FCC-HCP structure transformation in the CoCrFeMnNi HEA tensile specimen [147]. These reports implied that the phase transformation mechanism in the HEAs and MEAs are strongly correlated to the shear deformation. It is also clear that stacking faults

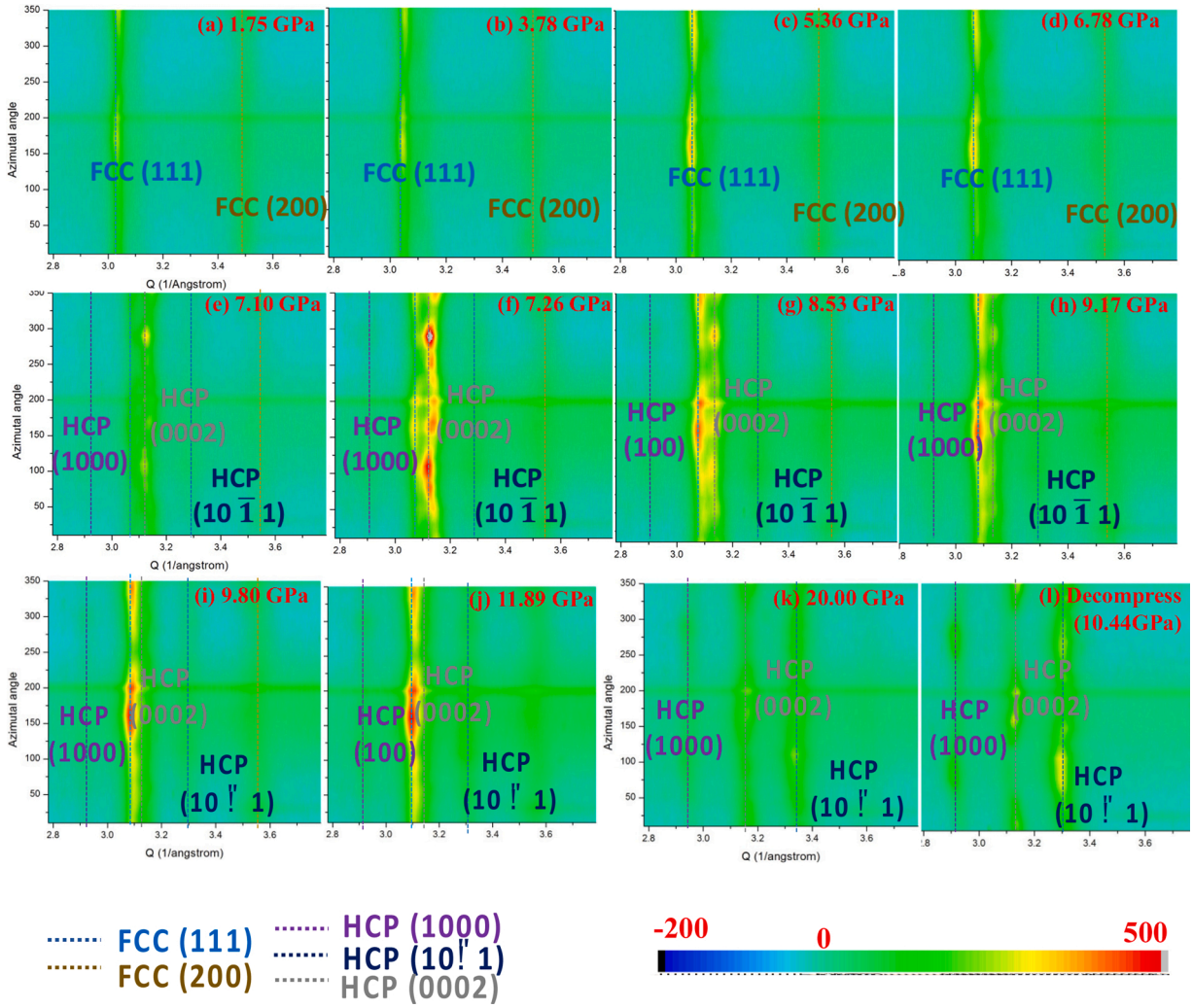

Fig. 27. Diffraction results of the collected system subjected to hydrostatic compression: (a) ~ (k) and (l) after decompression. (Adapted from [291] with permission from Elsevier).

play an important role in the phase stability and phase transformation in the HEMs.

3.3.3. *Stacking-fault effects on the HEAs*

Due to the complex nature of the HEMs, different principal elements have various crystal structures before forming the alloys. The HEMs in certain compositions possess a unique combination of high strength and high ductility. The unique combination is due to the change in the deformation mechanisms from the slip to twinning to transformation-induced plasticity. Recent work has demonstrated that the mechanism changes, resulting from a lower stacking fault energy (SFE) of alloys. Zhang et al. even proposed the negative SFEs and nano-twin formation in the FCC HEAs [143]. The SFE is the energy carried by the interruption of the normal atomic-stacking sequence, as exemplified for the FCC structure [111]. It is known that the SFE determines whether a material reveals transformation-induced plasticity (TRIP) or twinning-induced plasticity (TWIP). Furthermore, a low SFE is known to suppress dislocation climb and cross-slip, thereby modifying the dislocation gliding behavior and possibly decreasing the dislocation mobility. The (intrinsic) SFE, γ_{SF}, for the FCC structure is defined as

$$\gamma_{SF} = \frac{E_{SF} - E_{fcc}}{A_{\text{int}}} \tag{24}$$

where E_{SF} and E_{fcc} represent the energies of the FCC structure with and without a stacking fault, respectively. A_{int} denotes the interface area over which the stacking fault extends in the (111) plane [111]. Ikeda et al. summarized the *Ab initio* works on the SFEs of the HEAs with various methods of theoretical calculations of SFEs [111]. Table 9 outlines the SFEs of the HEMs modified after Ikeda et al. [111].

Besides the simulated SFE summarized in Table 9, Lam et al. applied the Convolutional Multiple Whole Profile (CMWP) modeling to analyze the *in-situ* neutron-diffraction profiles and [279] found the fatigue-induced stacking faults and twinning activities. Woo et al. estimated the SFE of the MEAs using *in-situ* neutron-diffraction experiments [443]. The *in-situ*neutron-diffraction was performed to obtain a number of faulting-embedded diffraction peaks simultaneously from a set of (*h k l*) grains during deformation. The peak profiles diffracted from the imperfect crystal structures were analyzed to correlate the stacking-fault probabilities and mean-square lattice strains to the SFEs. The results disclosed that the averaged SFE was 15.1 mJ/m^{2}in the CrCoNi alloys. Meanwhile, during deformation, the SFE varies from 24 to 11 mJ/m^2 from the initial to stabilized stages. The SFE of atomic configurations includes SRO or segregation-based atomic environments. The transient SFEs are attributed to the deformation activity changes from dislocation slip to twinning as straining. The significant variance of the SFE suggests the critical twinning stress as 790 ± 40 MPa for the CrCoNi MEA.

Gaurav Arora et al. [445] employed the ML-based methodology with a calculated dataset to anticipate the SFEs of the Ni-Fe-Cr system. They reported that the SFEs of multi-elemental alloys can be accurately

Table 9
Collection of experiments and *Ab initio* works on the SF of the HEMs. SF stands for "stacking fault". NM indicates that the Stacking Fault Energy (SFE) calculations are done under the non-magnetic condition modified after Ikeda et al. [111].

Year	Reference	HEAs	Specific calculation methods	Calculation/ Experiments
2013	Zaddach et al. [139]	FeNi, CrFeNi, CoCrFeNi, CoCrFeMnNi, and variations	EMTO-CPA VASP-SQS	*Ab initio* elastic constants + experimental SF probabilities
2015	Huang et al. [140]	CoCrFeMnNi	EMTO-CPA	Explicit SF
2016	Patriarca et al. [141]	CoCrFeMnNi	VASP-SQS	Explicit SF
2016	Wang et al. [434]	$Fe_{40.4}Ni_{11.3}Mn_{34.8}Al_{7.5}Cr_6$, $Fe_{40.4}Ni_{11.3}Mn_{34.8}Al_{7.5}Cr_6$+0.07%C, $Fe_{40\cdot4}Ni_{11.3}Mn_{34.8}Al_{7.5}Cr_6$+1.1%C		Measured via weak-beam imaging of the separation of dislocation partials using transmission electron microscopy (TEM)
	Beyramali Kivy and Asle Zaeem [142]	CoCrFeNi + additions of Cu, Mn, Al, Ti, Mo)	VASP + random supercell	Explicit SF
	Zhang et al. [143]	CoCrNi, CoCrFeNi	VASP-SQS	Explicit SF, Negative SFE
2017	Zhang et al. [143]	CoCrNi	VASP + random supercell	Explicit SF, ANNNI
	Zhao et al. [144]	CoCrFeMnNi, CoCrFeNiPd, and equiatomic subsystems	VASP-SQS	Explicit SF, ANNNI
	Liu et al. [435]	$FeCoNiCrAl_{0.1}$		*In-situ* TEM
	Cai et al. [436]	$FeCoCrNiMo_{2.3}$		*In-situ* neutron diffraction
	Alkan et al. [145]	CoCrFeMnNi	VASP-SQS	Explicit SF
2018	Huang et al. [146]	CoCrNi, CoCrMnNi, CoCrFeNi, CoCrFeMnNi	EMTO-CPA	Explicit SF
	Niu et al. [147]	CoCrNi, CoCrFeMnNi	VASP-SQS	Explicit SF
	Wang et al. [437]	$Al_{0.6}CoCrFeNi$	According to the critical stress theory, SFE of the FCC phase is estimated	Dynamic impact tests
	Agarwal et al. [438]	FeMnNi, FeMnNiCo, FeMnNiCoCu	CALPHAD	Combinatorial approach
	Liu et al. [439]	NiCoCr, FeCoNiCr, FeCoNiCrMn, $(FeCoNiCr)_{94}Mn_6$, $(FeCoNiCr)_{86}Mn_{14}$, $Fe_{20}Co_{15}Ni_{25}Cr_{20}Mn_{20}$		Experimentally measured by weak-beam dark-field using TEM
2018	Huang et al. [290]	CoCrFeMnNi		*In-situ* diffraction peak profile evolutions showing the SFs formation prior to the phase transformation
2018	Niu et al.	CoCrNi	DFT calculations with the Vienna ab initio Simulation Package (VASP), using the projector augmented wave (PAW) method	Scanning transmission electron microscopy (STEM), in high-angle annular dark field (HAADF) mode
2019	Huang et al. [291]	CoCrFeMnNi		Resolving *in-situ* 2D diffraction peak profiles showing the deviatoric deformation-induced SFs
2019	Jiang et al. [440]	$CoFeNi_2V_{0.5}Mo_{0.2}$		Synchrotron X-ray diffraction, TEM
2019	Wu et al. [441]	$CoCrFeNiMo_{0.15}$		Experimentally estimated via measuring the widths of the dissociated dislocations using TEM
2019	Gao et al. [442]	$Cr_{26}Mn_{20}Fe_{20}Co_{20}Ni_{14}$		TEM
2020	Woo et al. [443]	CrCoNi		*In-situ* neutron-diffraction
2020	Frank et al. [444]	$Fe_{40}Mn_{20}Cr_{15}Co_{20}Si_5$		*In-situ* neutron-diffraction
2020	Lam et al. [279]	CoCrFeMnNi	Convolutional Multiple Whole Profile (CMWP) modeling for analyzing the neutron-diffraction profiles	*In-situ* neutron-diffraction showing fatigue-induced SFs evolutions

predicted by the ML model while relying only on the dataset of binary alloys. Once the dataset is produced by the calculation of inter-atomic potentials, which may not agree quantitatively with the DFT or experiment, the present work serves as a proof-of-concept framework. Due to the limitation of calculations, the dataset of the calculated structure did not consider the magnetic, elemental segregation, and SRO structure effects. Although it remains to be a proof-of-concept, it opens a promising possibility for the design of HEAs owning high strength and high ductility if the specific training data can be included in the future. Vilalta et al. also applied ML models to predict the relationship between the yield stress and the SFE landscape in the HEAs [446]. The data for learning in this work were taken from phase-field dislocation dynamics simulations of partial dislocations in the FCC metals. Vilalta et al. adopted three different ways to describe the variations of the SFE landscape as the inputs to the ML models. Vilalta et al.'s best ML model can predict the yield stress to approximately 2% error [446].

4. Environmental resistance properties for the HEM studies

Environmental resistance is a major requirement for structural alloys. Among aqueous corrosion, wear, high-temperature oxidation, and stress-corrosion cracking [33], Raabe et al.'s pointed out that the corrosion protection is on the top priority for structural alloys [63]. Due to the importance of the corrosion applications, there are already successful ML and HT experiments to develop new materials (such as for the metallic glass [240] and alternatives to toxic chromate corrosion inhibitors [447]) and to predict the corrosion behavior of the existing materials. For example, Winkler et al. screened a large library of organic compounds using HT experiments to assess 100 small organic molecules as the potential inhibitors of corrosion in the aerospace Al alloys of AA2024 and AA7075 [447]. Smith et al. designed the computerized optical analysis method as a new, rapid, HT corrosion testing method to quantify the corrosion data [448]. Using ML, Pei et al. forecasted the atmospheric corrosion of a carbon steel [449]. Pei et al.'s results showed that the random forest (RF) models have higher accuracy than ANN and SVR models for corrosion prediction. Liu et al. applied ML for multiple-performance optimization to develop the material with satisfactory resistance to hot-corrosion and oxidation [450]. Liu et al. firstly introduced the phase-classification model trained with the CALPHAD thermodynamic database to filter the potential composition with γ and γ' two-phase microstructures. Multi-regression models with bootstrap sampling were built to predict the γ' solvus temperature, solidus, liquidus, and density based on an experimental dataset assembled from the literature. Multi-performance optimization was adopted to search for

γ′-strengthened Co-based superalloys. The final optimized γ′-strengthened Co-base superalloys were obtained through three rounds of experiment validations and fabricating four alloys each round. The best performer of new alloys is Co-36Ni-12Al-2Ti-4Ta-1W-2Cr, which could be comparable with some advanced Ni-base single-crystal superalloys [450]. Yan et al. analyzed the effect of various parameters on the atmospheric corrosion behavior of low alloy steels and anticipated the corrosion rates using ML [451]. Wen et al. used SVR and BPNN (back propagation neural network) models for the prediction of corrosion rates of a 3C steel under different seawater environments [452]. Kamrunnahar et al. developed supervised BPNN mapping method to forecast the polarization curves in the $Fe_{68}Ni_{14}$-xMo$x$$Si_2B_{16}$ metallic glass, the corrosion rates in the carbon and alloy steels, and the extent of crevice corrosion damage in the grade-2 titanium as a function of changing environment [453]. The pitting corrosion behavior of 316 L stainless steel (SS), in different environment conditions, was studied by Jimeneze-come et al. using the model based on KNN and ANNs. Jimeneze-come et al.'s results exhibited very good precision, which are all above ~93 % [454]. Overall, Fig. 28 presents that ML can be successfully utilized to predict different corrosion properties.

With growing interest in the field of multi-component systems viz. HEMs, it is imperative to forecast their corrosion behaviors under different environmental conditions for their potential applications. Unfortunately, the studies on predicting the corrosion behaviors in the HEMs using ML are scarce. Recently, the U.S. Department of Energy (DOE) awarded more than $45.3 million through its Nuclear Energy University Program (NEUP) to support university-led nuclear energy research and development projects, including "Machine learning on HT databases of irradiation response and corrosion properties of selected compositionally complex alloys for structural nuclear materials." led by the University of Wisconsin-Madison [456].

As the HEAs consist of multiple elements in equiatomic or non-equiatomic ratios, the microstructure and resultant corrosion behavior will depend upon the synergistic effects of all the constituent elements. This trend is in contrast with the conventional alloys, where their properties are dictated by one or mostly two dominant elements. Apart from the composition and microstructure, processing method and type of the electrolyte will also affect the corrosion response of the HEAs. In this section, a comprehensive review on the corrosion behavior of the HEAs is presented.

Table 10 lists the corrosion parameters (E_{corr}, i_{corr}, and E_{pit}, or E_b: as the breakdown potential) for several HEAs and conventional alloys. The relatively lower corrosion potential, current density, and higher pitting/breakdown potentials in the HEAs, as compared to the conventional alloys, indicate that the HEAs can be good candidates as corrosion-resistant alloys in aqueous corrosive media.

An earlier study on the corrosion characteristics of the HEAs was carried out by Chen et al., where the corrosion behaviors of the $Cu_{0.5}$NiAlCoCrFeSi HEA and 304 SS alloy were evaluated and compared in an aqueous solution of H_2SO_4 and NaCl. Anodic polarization suggested that the HEA exhibits better corrosion resistance than the 304 SS alloy in the range of concentration (0.1–1 M) of aqueous solution. However, resistance to pitting corrosion in the Cl^- environment of the HEA was inferior, as compared to the 304 SS because of the observed narrower passive region in the former. The addition of NaCl to 1 N H_2SO_4 solution changes the corrosion characteristics of the HEA. The corrosion resistance decreases up to 0.5 M NaCl and then increases, as shown in Fig. 29 [457].

The effects of Mo on the corrosion behavior of the $CoCrFeNi_2$ HEA in 3.5 wt. % NaCl were studied by Rodriguez et al. [458]. A higher corrosion resistance in the $CoCrFeNi_2Mo_{0.25}$ compared to the $CoCrFeNi_2$ HEA was attributed to the presence of Mo, which stabilized the protective Cr_2O_3 passive layer by the precipitation of MoO_2 on the surface. Using X-ray photoelectron spectroscopy (XPS), Dai et al. [475] concluded that the $CoCrFeNiMo_x$ (x = 0, 0.1, 0.3, and 0.6) HEAs consisted of a bilayer-structured surface film. The outer layer contained a mixed Cr/Fe hydroxides/oxides and MoO_3, whereas the inner layer was rich in Cr(III) species with a higher ratio of Cr(ox) and Cr(hyd) along with MoO_4 and Fe_2O_3. The addition of Mo was found to increase the Cr (ox)/Cr(hyd) and molybdenum oxide in the protective film, thus, increasing the Mo content resulted in an improved corrosion resistance in the H_2SO_4 solution. Dai et al. [475] further suggested that the damage mechanism changes from pitting in the CoCrFeNi and $CoCrFeNiMo_{0.1}$ HEAs to selective dissolution in the $CoCrFeNiMo_x$ (0.3 and 0.6) HEAs due to the change in the microstructure from a single FCC phase to a dual phase [FCC + (Cr, Mo)-rich precipitates] as the Mo content is increased. Shang et al. [459] varied the content of Mo (x = 0.1 – 0.5) in the $CoCrFeNiMo_x$ HEA and elucidated the corrosion behaviors in 3.5 wt. %

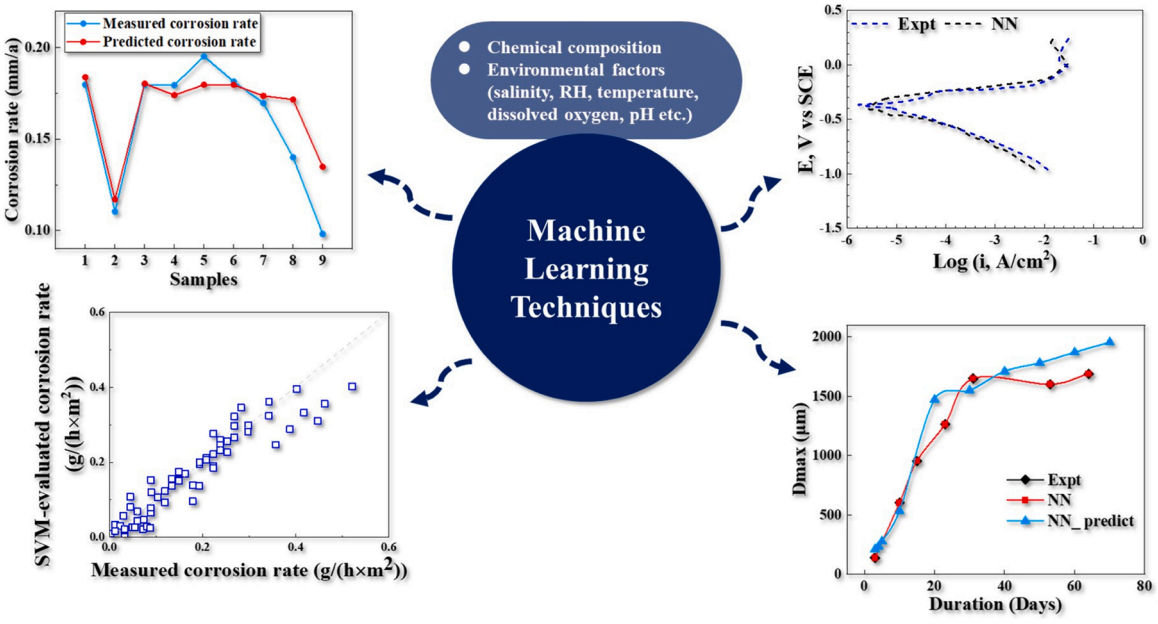

Fig. 28. Evaluation of corrosion properties using machine learning techniques based on the information of materials and environmental factors [451,453,455]. Adapted with permission from Elsevier.

Table 10
Summary of corrosion parameters in the HEAs and conventional alloys from previous studies. The average values of the parameters at room temperature are presented. SCE: saturated calomel electrode, MSE: mercurous sulfate electrode, SHE: standard hydrogen electrode. Reference electrode is SCE unless specified.

HEA System	Electrolyte	E_{corr} (V_{SCE})	i_{corr} ($\mu A/cm^2$)	E_{pit} /E_b (V_{SCE})	Ref.
$Cu_{0.5}NiAlCoCrFeSi$	0.1 M NaCl	0.01	0.178	0.58	[457]
	1 M NaCl	−0.53	3.16	−0.25	
	0.1 N H_2SO_4	−0.06	10.7	0.11	
	1 N H_2SO_4	−0.41	251	0.09	
	1 N H_2SO_4 + 1 M NaCl	−0.45	141	−0.28	
	1 N H_2SO_4 + 0.6 M NaCl	−0.47	1620	−0.23	
	1 N H_2SO_4 + 0.5 M NaCl	−0.48	1950	−0.21	
	1 N H_2SO_4 + 0.4 M NaCl	−0.46	1710	−0.215	
	1 N H_2SO_4 + 0.1 M NaCl	−0.44	316	−0.24	
	1 N H_2SO_4 + 0.01 M NaCl	−0.43	282	−0.22	
304 SS	0.1 M NaCl	−0.25	1.59	0.46	
	1 M NaCl	−0.59	4.37	0.17	
	0.1 N H_2SO_4	−0.05	50.1	1.12	
	1 N H_2SO_4	−0.22	501	1.06	
$CoCrFeNi_2$	3.5 wt. % NaCl	−0.29	0.129	0.32	[458]
$CoCrFeNi_2Mo_{0.25}$		−0.26	0.125	0.91	
Hastelloy C-276		−0.28	0.128	0.74	
316 L		−0.25	0.111	0.27	
$CoCrFeNiMo_{0.1}$	3.5 wt. % NaCl	−0.263	0.381	0.949	[459]
$CoCrFeNiMo_{0.2}$		−0.131	0.072	0.941	
$CoCrFeNiMo_{0.3}$		−0.257	0.766	0.955	
$CoCrFeNiMo_{0.4}$		−0.261	0.082	0.948	
$CoCrFeNiMo_{0.5}$		−0.261	0.738	0.965	
$CoCrFeNiMo_{0.1}$	0.5 M H_2SO_4 (MSE)	−0.688	9.666	0.469	
$CoCrFeNiMo_{0.2}$		−0.682	2.926	0.460	
$CoCrFeNiMo_{0.3}$		−0.694	8.626	0.453	
$CoCrFeNiMo_{0.4}$		−0.663	0.712	0.462	
$CoCrFeNiMo_{0.5}$		−0.632	1.526	0.450	
$Al_{0.1}$ CoCrFeNi	3.5 wt. % NaCl (Ag/AgCl)	−0.0223	0.45	0.917	[460]
SS304		−0.0398	0.76	0.474	
$Al_{0.3}CoCrFeNi$	3.5 wt. % NaCl	−0.195	0.0835	0.460	[461]
$AlC_{0.5}CoCrFeNi$		−0.225	0.252	0.385	
$Al_{0.7}CoCrFeNi$		−0.275	0.429	0.052	
CoCrFeNi	0.5 M H_2SO_4 (SHE)	−0.081	15.8	0.002	[462]
$Al_{0.25}CoCrFeNi$		−0.095	16.7	0.008	
$Al_{0.50}$ CoCrFeNi		−0.084	13.4	0.017	
AlCoCrFeNi		−0.094	13.1	0.010	
SS304		−0.185	45.3	−0.071	
$CrFe_{1.5}MnNi_{0.5}$	0.5 M H_2SO_4 (SHE)	−0.229	686.0	−0.055	
$Al_{0.3}CrFe_{1.5}MnNi_{0.5}$		−0.194	~2390	−0.012	
$Al_{0.5}CrFe_{1.5}MnNi_{0.5}$		−0.206	~5080	0.047	
304 SS		−0.186	74.5	−0.022	
$CrFe_{1.5}MnNi_{0.5}$	0.5 M H_2SO_4 (SHE)	−0.221	686.0	1.172	[463]
	0.5 M H_2SO_4 + 0.10 M NaCl (SHE)	−0.242	~ 2060	1.180	
	0.5 M H_2SO_4 + 0.25 M NaCl (SHE)	−0.238	~ 4600	0.589	
	0.5 M H_2SO_4 + 0.50 M NaCl (SHE)	−0.240	~ 9750	0.475	
$Al_{0.3}CrFe_{1.5}MnNi_{0.5}$	0.5 M H_2SO_4 (SHE)	−0.194	~ 2390	1.164	
	0.5 M H_2SO_4 + 0.10 M NaCl (SHE)	−0.219	~ 2480	1.156	
	0.5 M H_2SO_4 + 0.25 M NaCl (SHE)	−0.231	~ 6050	0.250	
	0.5 M H_2SO_4 + 0.50 M NaCl (SHE)	−0.250	~ 10,400	0.257	
$Al_{0.3}CoCrFeNi$ (As-forged)	3.5 wt. % NaCl	−0.189	0.0632	0.522	[464]
$Al_{0.5}CoCrFeNi$ (As-forged)		−0.261	0.187	0.316	
$Al_{0.7}CoCrFeNi$ (As-forged)		−0.292	0.392	0.118	
$Al_{0.3}CoCrFeNi$ (As-equilibrated)		−0.180	0.0289	0.808	
$Al_{0.5}CoCrFeNi$ (As-equilibrated)		−0.228	0.0714	0.496	
$Al_{0.7}CoCrFeNi$ (As-equilibrated)		−0.258	0.267	0.256	
CoCrFeNi	0.6 M NaCl	−0.248	0.108	0.442	[465]
$Al_{0.3}CoCrFeNi$		−0.252	0.238	0.290	
$Al_{0.6}CoCrFeNi$		−0.179	0.070	0.190	
$Al_{0.9}CoCrFeNi$		−0.216	0.093	0.164	
$Al_{0.9}CoCrFeNiTi_{0.5}$		−0.347	0.310	0.184	
$Al_2CoCrFeNi$	3.5 wt. % NaCl	−0.1934	0.00941	0.1933	[466]
$Al_{1.8}CoCrFeNiTi_{0.2}$		−0.2602	0.02633	0.1894	
$Al_{1.5}CoCrFeNiTi_{0.5}$		−0.2394	0.01644	0.2622	
$Al_{1.2}CoCrFeNiTi_{0.8}$		−0.2588	0.02411	0.3486	
AlCoCrFeNiTi		−0.311	0.03273	0.3694	
$Al_{0.8}CoCrFeNiTi_{1.2}$		−0.426	0.05600	0.3533	
AlCoCrFeNiTi	3.5 wt. % NaCl	−0.27	0.561	–	[467]
$Al_{0.8}CoCrFeNiTi_{0.2}$		−0.69	7.96	–	
$Al_{0.5}CoCrFeNiTi_{0.5}$		−0.32	0.532	–	
AlCoCrFeNi	0.5 M H_2SO_4 (MSE)	−0.41	~ 546	−0.35	
$Al_{0.8}CoCrFeNiTi_{0.2}$		−0.47	~ 117	−0.12	
$Al_{0.5}CoCrFeNiTi_{0.5}$		−0.40	~ 320	−0.21	

(continued on next page)

Table 10 (*continued*)

HEA System	Electrolyte	E_{corr} (V_{SCE})	i_{corr} ($\mu A/cm^2$)	E_{pit} /E_b (V_{SCE})	Ref.
AlCoCuFeNi	0.5 M H_2SO_4	−0.058	7.93	–	[468]
AlCoCuFeNiCr		−0.075	5.09	–	
AlCoCuFeNiTi		−0.253	44.76	–	
AlCoCuFeNiCrTi		−0.256	39.59	–	
$AlCoCrFeNiSi_{0.1}$	0.5 M H_2SO_4	−0.453	304.20	0.925	[469]
304 SWS		−0.438	105.12	0.925	
CoCrFeNi	0.6 M NaCl (Ag/AgCl)	−0.257	–	0.556	[470]
CoCrFeNiAl		−0.322	–	0.297	
CoCrFeNiCu		−0.180	–	−0.069	
CoCrFeNiSn		−0.252	–	1.099	
SS304		−0.246	–	0.199	
SS316		−0.254	–	0.267	
FeCoNiCr	3.5 wt. % NaCl	−0.26	0.0315	0.31	[471]
$FeCoNiCrCu_{0.5}$		−0.29	0.723	0.09	
FeCoNiCrCu		−0.33	1.32	0.08	
304 L SS		−0.25	0.601	0.23	
$Al_{0.5}CoCrCuFeNiB$	1 N H_2SO_4 (SHE)	−0.115	787	0.233	[472]
$Al_{0.5}CoCrCuFeNiB_{0.2}$		−0.121	1025	0.215	
$Al_{0.5}CoCrCuFeNiB_{0.6}$		−0.148	2626	–	
$Al_{0.5}CoCrCuFeNiB$		−0.159	2848	–	
AlCoCrCuFe	0.6 M NaCl	−0.264	0.967	−0.130	[473]
$(TiAl)_{0.7}V_{0.15}Fe_{0.1}Ni_{0.05}$		−0.388	0.037	0.263	
AlTiVCrSi		−0.498	0.168	0.011	
$CoCrFeNiAl_{0.9}$		−0.217	0.093	0.164	
CoCrFeNi (SPS˜)		−0.304	0.610	−0.008	
$Ti_{0.3}(CoCrFeNi)_{0.7}$		−0.273	0.036	1.040	
$TiZr_{0.5}NbCr_{0.5}$	3.5 wt. % NaCl	−0.489	0.00441	1.180	[474]
$TiZr_{0.5}NbCr_{0.5}V$		−0.311	0.00974	1.448	
$TiZr_{0.5}NbCr_{0.5}Mo$		−0.455	0.0940	1.400	
$TiZr_{0.5}NbCr_{0.5}$	0.5 M H_2SO_4	−0.277	0.452	0.968	
$TiZr_{0.5}NbCr_{0.5}V$		−0.087	0.02039	0.998	
$TiZr_{0.5}NbCr_{0.5}Mo$		−0.018	0.0526	0.984	

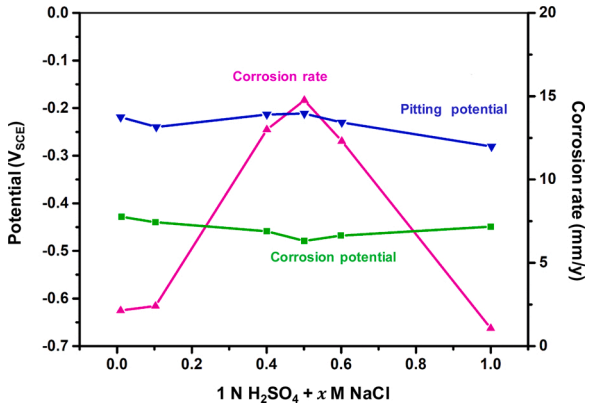

Fig. 29. Variation of corrosion rate, pitting potential, and corrosion potential with the concentration of NaCl in 1 N H_2SO_4. Adapted from [457] with permission from Elsevier.

NaCl and 0.5 M H_2SO_4. The corrosion resistance increased up to x = 0.2 but decreased with further increase in the Mo content due to the precipitation of a secondary σ phase (Cr-Mo rich) in the interdendritic regions [476,477].

Kumar et al. [460] investigated the general and pitting corrosion resistance in the $Al_{0.1}CoCrFeNi$ HEA whose resistance was found to be higher than that in the 304 SS in 3.5 wt. % NaCl. The pit number density was higher in the 304 SS rather than in the HEA. However, the depth of the pits was almost similar. In addition, the pits were elliptical for the 304 SS but circular for HEA. The number distributions of pit sizes for the HEA and 304 SS are shown in Fig. 30 (a) and (b), respectively. Using the lognormal distribution fitting, the average pit size for the HEA and 304 SS was measured to be 142 and 110 μm, respectively. In the case of the HEA, most of the pits were of size less than 100 μm. The better corrosion resistance in the HEA was postulated to be due to its single-phase microstructure, i.e., no micro-galvanic effect and presence of a passive oxide film (Al_2O_3/Cr_2O_3).

The influence of aluminum (Al) content on the pitting-corrosion behaviors of the $Al_xCoCrFeNi$ (x = 0.3, 0.5, and 0.7) in a 3.5 wt. % NaCl solution was also studied by Shi et al. [461]. Increasing the Al content changed the microstructure from a single-phase FCC in the $Al_{0.3}CoCrFeNi$ to FCC + BCC (both ordered and disordered) phase in the $Al_{0.7}CoCrFeNi$. The increased volume fraction of the (Al, Ni)-rich and Cr-depleted BCC phase decreased the corrosion resistance of the HEA due to the increased extent of the selective dissolution of the Cr-depleted BCC phases in the presence of Cl^- ions. Fig. 31(a) shows the formation of sporadic pits in a single-phase FCC $Al_{0.3}CoCrFeNi$. In contrast, localized corrosion is severe in the case of the $Al_{0.7}CoCrFeNi$ HEA [Fig. 31(c)], where a complete BCC phase is attacked. Using an *in-situ* visualization system, Shi et al. [478] later confirmed that the localized corrosion changed from pitting in the $Al_{0.3}CoCrFeNi$ to selective dissolution of BCC phases in the HEAs containing a higher content of Al. Similar selective dissolution of the BCC phase in the FCC matrix was observed when the $Al_{0.5}CoCrFeNi$ [(Fig. 31(b)] was exposed to the 3.5 wt. % NaCl solution after aging in a temperature range of 350–950 °C [479].

Kao et al. [462] evaluated the corrosion behaviors of the $Al_xCoCrFeNi$ HEAs (x = 0, 0.25, 0.50, and 1.0) by immersing them in a corrosive solution (0.25 M, 0.5 M and 1.0 M NaCl in the 0.5 M H_2SO_4 solution) and performing polarization tests. Interestingly, increasing the Al content did not bring a significant change in the corrosion potential (E_{corr}) and corrosion current density (i_{corr}) values, and no obvious trend was observed in the polarization tests. The passive region was observed between 0–1.2 V_{SHE} in 0.5 M H_2SO_4, and pitting potential (E_{pit}) of the studied alloys decreased with the addition of Cl^- ions. Furthermore, the corrosion rates, measured from the weight loss in the immersion tests (8–15 days), were reported to be much higher in the alloys containing a higher Al content ($Al_{0.5}CoCrFeNi$ and AlCoCrFeNi) than in the remaining two alloys. This feature was also postulated to be due to the selective dissolution of a (Al, Ni)-rich phase in the HEAs with a higher Al content.

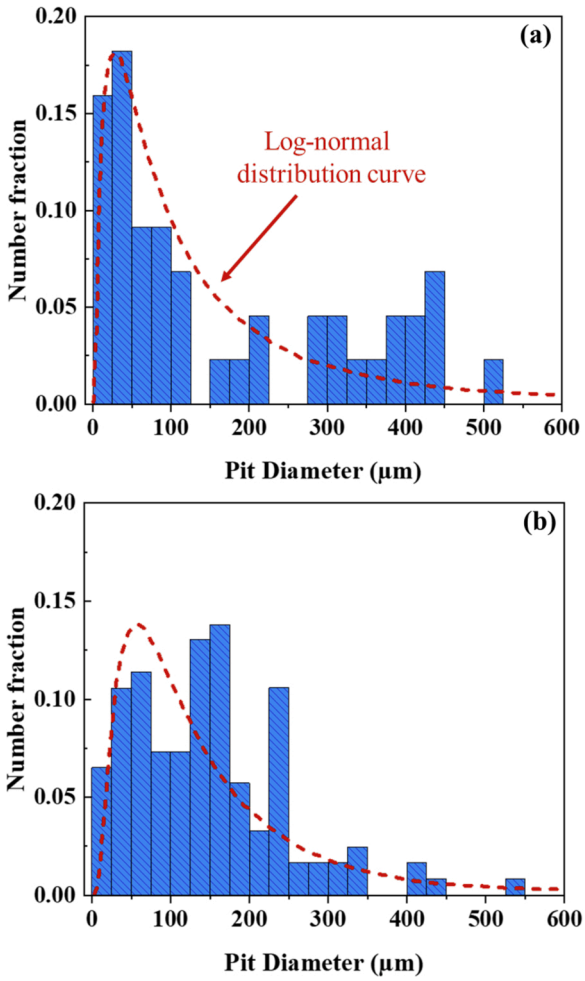

Fig. 30. Distribution of pit size in the (a) $Al_{0.1}CoCrFeNi$ HEA, and (b) 304 SS. Adapted from [460] with permission from Elsevier.

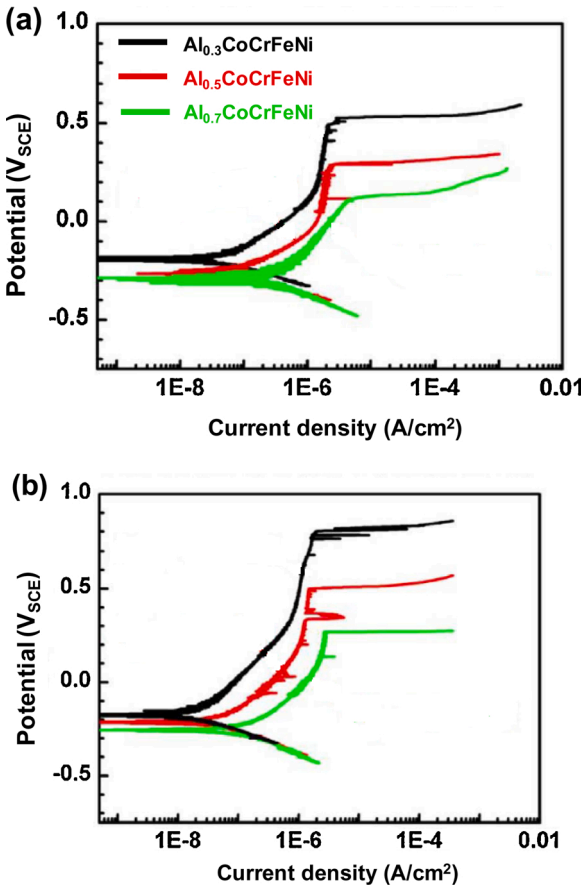

Fig. 32. Polarization curves in the $Al_xCoCrFeNi$ in a 3.5 wt. % NaCl solution for (a) as-forged and (b) as-equilibrated conditions. Adapted from [464] with permission from Elsevier.

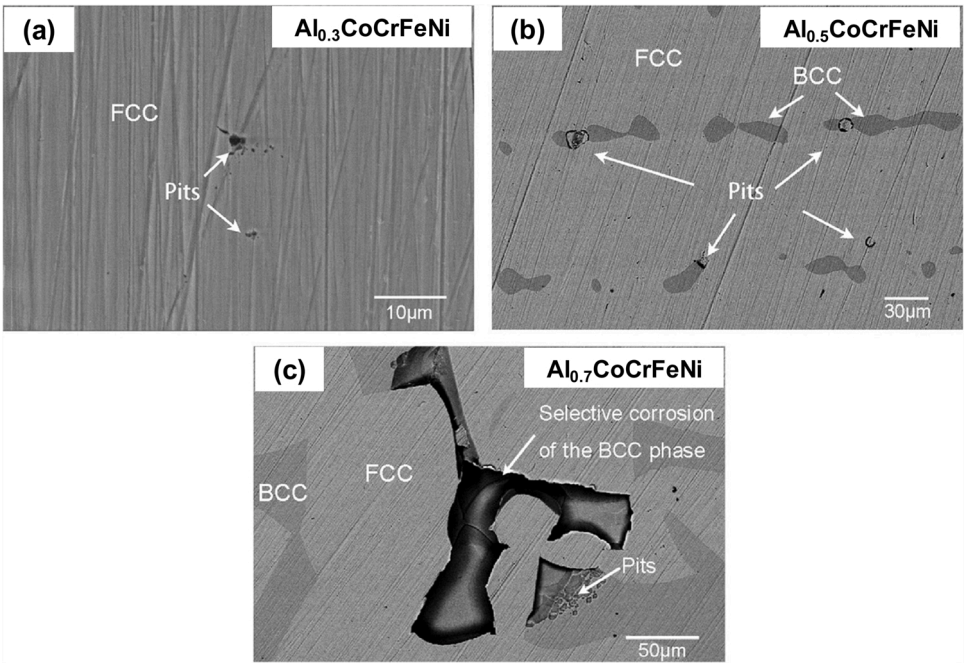

Fig. 31. SEM micrographs showing the pits after a potentiodynamic polarization test for (a) $Al_{0.3}CoCrFeNi$, (b) $Al_{0.5}CoCrFeNi$, and (c) $Al_{0.7}CoCrFeNi$. Adapted from [461] with permission from Elsevier.

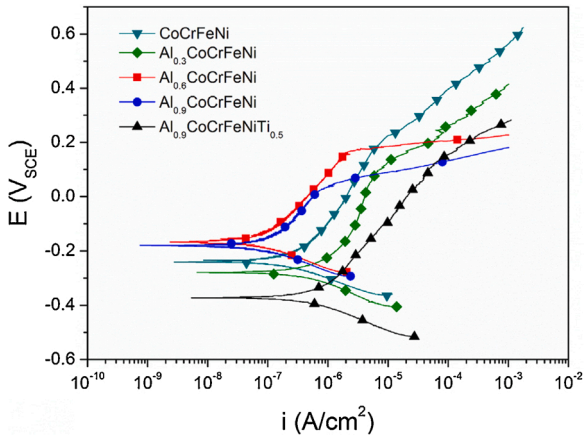

Fig. 33. Potentiodynamic-polarization curves for the $Al_xCoCrFeNiTi_y$ HEAs in a 0.6 M NaCl solution. Adapted from [465] with permission from Elsevier.

In another study, an increase in the Al content was also observed to increase the i_{corr} values and decrease the E_{pit} values of the $Al_xCrFe_{1.5}MnNi_{0.5}$ (x = 0, 0.3, and 0.5) HEAs in 1 M NaCl and 0.5 M H_2SO_4 solutions [463]. Shi et al. [464] further investigated the effect of homogenization at 1250 °C on the corrosion response of the $Al_xCoCrFeNi$ (x = 0.3, 0.5, and 0.7) HEAs in a 3.5 wt. % NaCl solution using a potentiodynamic polarization test. The alloys were first forged at 1250 °C for 50 % reduction (as-forged condition), followed by annealing at 1250 °C for 1000 h (as-equilibrated condition). Increasing the Al content resulted in a change in the microstructure from (Co, Cr, Fe)-rich single-phase FCC in $Al_{0.3}CoCrFeNi$ to a multi-phase (FCC + BCC) microstructure in $Al_{0.7}CoCrFeNi$, where BCC phases were (Al, Ni)-rich and (Co, Cr, Fe)-rich. Fig. 32 presents the polarization curves for both as-forged and as-equilibrated conditions, where a decrease in the E_{corr} and an increase in the i_{corr} can be observed with increasing Al content, suggesting an improved general corrosion resistance at a lower Al concentration. Furthermore, a decrease in the E_{pit} with increasing Al content indicated a weakened localized corrosion resistance at higher Al contents. The observed trend was again ascribed to the multi-phase microstructure at higher Al contents. Nevertheless, homogenization resulted in an improved corrosion resistance in all the alloys due to the reduced elemental segregation, which resulted in a decreased variation of the work function, measured by scanning Kelvin probe force microscopy (SKPFM).

Qui et al. [465] investigated the role of Al along with an addition of titanium (Ti) on the corrosion behavior of the as-cast CoCrFeNi HEA in a 0.6 M NaCl solution. In contrast to the observation made by Shi et al. [461], this study concluded an increased general corrosion resistance with increasing Al content from 0.3 to 0.9, as i_{corr} values decreased (Fig. 33). This trend was supposedly attributed to the increased fraction of Al_2O_3 in the passive film with an increase in the Al content. The

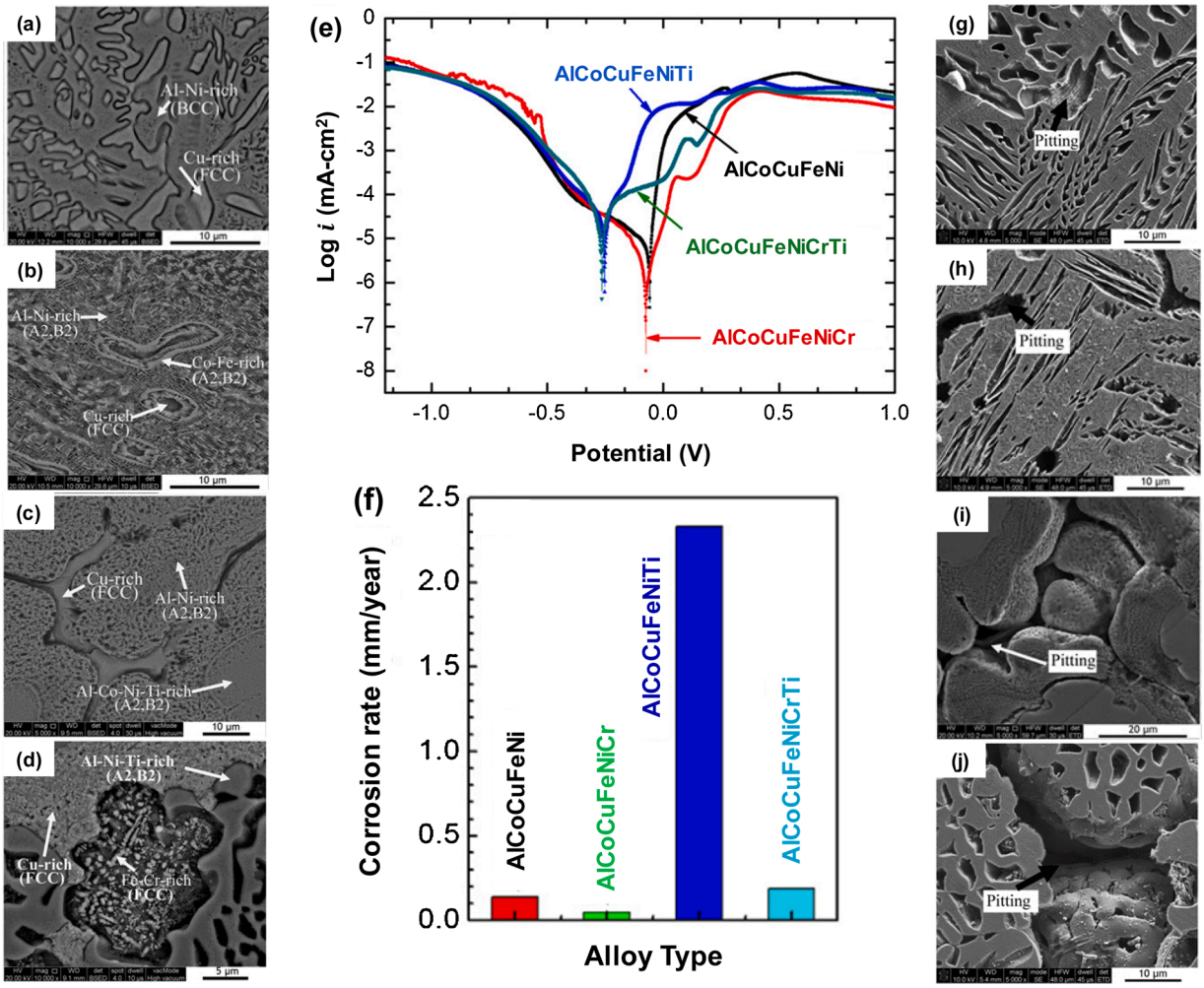

Fig. 34. SEM micrographs before and after corrosion for (a, g) AlCoCuFeNi, (b, h) AlCoCuFeNiCr, (c, i) AlCoCuFeNiTi, (d, j) AlCoCuFeNiCrTi. (e) Potentiodynamic-polarization curves and (f) corrosion rates measured from the immersion test in a 0.5 M H_2SO_4 solution. Adapted from [468] with permission from Elsevier.

microstructure changed from a single-phase FCC (0 and 0.3 Al) to FCC + BCC + B_2 (0.6 and 0.9 Al) phase. The addition of Ti ($Al_{0.9}CoCrFeNiTi_{0.5}$) resulted in a dramatic decrease in the corrosion resistance. In fact, the i_{corr} value of this HEA was the highest (Fig. 33), which was ascribed to the formation of a Fe-Cr-type sigma phase leading to the depletion of Cr from the matrix.

Zhao et al. [466] also elucidated the role of Ti/Al ratio on the corrosion-resistance behaviors of the $Al_{2-x}CoCrFeNiTi_x$ HEAs (x = 0, 0.2, 0.5, 0.8, 1.0, and 1.2) in a 3.5 wt. % NaCl solution. The microstructure changes from $BCC_1 + B_2$ and $BCC_1 + BCC_2 + B_2$ to $BCC_1 + BCC_2$ + Laves phases with increasing Ti content, where BCC_1 is characterized as the (Fe-Cr)-rich phase, and BCC_2 is the (Al, Ni)-rich phase (similar to the B_2-NiAl phase). Among all the studied Ti-containing alloys, $Al_{1.5}CoCrFeNiTi_{0.5}$ exhibited the best general corrosion properties. The lower corrosion resistance at a higher Ti content was due to the negative effect of the multi-phase structures and decreased the protection level by the passive film. However, it should be noted that all of the Ti-containing alloys exhibit higher E_{pit} with a wide passive region, which suggested that Ti addition improves pitting corrosion resistance. Jiang et al. [467] studied the corrosion behaviour of the $Al_xCoCrFeNiTi_{1-x}$ (x = 0.5, 0.8, and 1.0) in a 3.5 wt. % NaCl solution. The highest and lowest corrosion resistance was observed for Ti-free and $Al_{0.8}CoCrFeNiTi_{0.2}$ HEAs, respectively. The authors mentioned that although Ti itself is resistant to Cl^- ions, the elemental segregation and dual-phase structure (FCC + BCC phases) with Ti addition negate its beneficial effect in the case of $Al_{0.8}CoCrFeNiTi_{0.2}$. In the $Al_{0.5}CoCrFeNiTi_{0.5}$ HEA, a higher content of Ti was probably able to counter the aforementioned weakening effect and thereby increased the corrosion resistance.

Xiao et al. [468] carried out both immersion and potentiodynamic-polarization tests in 0.5 M H_2SO_4 and observed that an addition of Cr to AlCoCuFeNi improved the corrosion resistance, whereas the Ti addition deteriorated the corrosion resistance. Both i_{corr} from polarization curves and corrosion rates from immersion tests showed the following corrosion-resistance trend: AlCoCuFeNiCr > AlCoCuFeNi > AlCoCuFeNiCrTi > AlCoCuFeNiTi [Fig. 34 (e, f)]. This behavior can be attributed to the distribution of phases in the alloys. All four alloys consist of the FCC phase, ordered BCC (B_2) phase, and disordered BCC (A_2) phase, as presented in Fig. 34 (a–d). Increasing the Cr content increased the fraction of the BCC (B_2/A_2) phase while the Ti addition increased the fraction of the FCC phase. The authors reported that as the FCC phase is more anodic, as compared to the BCC phase, the former dissolves, leading to the formation of pits, as shown in Fig. 34 (g–j). Therefore, since the fraction of the FCC phase increases with the Ti addition, the corrosion resistance also decreases with an increase in the Ti content.

The addition of 0.1 Si to the AlCoCrFeNi was not observed to induce a significant change in the microstructure of the HEA [469]. In the presence of the corrosive medium (3.5 wt. % NaCl), the alloys exhibit pseudo-passive behavior, where the pits are formed at the dendrites due to their lower Cr content and formation of micro-galvanic coupling with interdendrites. In contrast, active-passive behavior was observed in a 0.5 M H_2SO_4 solution. The corrosion-resistance behaviors of the $CoCrFeNiW_x$ (x = 0, 0.2, and 0.5) HEAs was evaluated by Niu et al. [480]. The medium was seawater, which was prepared by the distilled water and artificial sea salt in the ratio of 30:1 (mass ratio). The $CoCrFeNiW_{0.5}$ exhibited the highest pitting resistance and easy passivation behavior, which was attributed to the increase in the stability of the chromium-oxide passive film by the addition of tungsten. Muangtong et al. [470] investigated the role of Sn, Cu, and Al additions on the corrosion susceptibility of the CoCrFeNi HEA in a 0.6 M NaCl solution. Among all the alloys, CoCrFeNiSn performed the best corrosion resistance due to the largest passive region and the highest pitting potential, indicating that the alloy's passive film has a good stability for pitting corrosion resistance. This behavior was assigned to the presence of both Cr_2O_3 and SnO_2 in the surface film, making it resistant to the attack. The CoCrFeNiCu was observed to exhibit the lowest corrosion resistance.

Hsu et al. [471] explored the effect of Cu on the corrosion properties of the $CoCrFeNiCu_x$ (x = 0, 0.5, and 1.0) HEAs in a 0.6 M NaCl solution. With increasing Cu content, the corrosion resistance of the HEA was observed to decrease, which was ascribed to the dissolution of Cu-rich regions. It was postulated that due to the weak binding force with other elements, Cu segregates as Cu-rich and Cu-depleted regions. In the presence of the corrosive solution, Cu-rich regions preferentially corrode due to the micro-galvanic effect. Luo et al. [481] examined the corrosion resistance of the CoCrFeNiMn HEA in a 0.1 M H_2SO_4 solution and compared with the 304 L SS. The HEA exhibited lower corrosion resistance than the 304 L SS. Although both HEA and 304 L SS had good passive layer forming capability, the lower Cr content in the passive layer of the HEA and no obvious selective dissolution of other elements were the plausible reasons for the observed lower corrosion resistance. Later, Sarraf et al. [482] also revealed that the presence of Mn degraded the pitting-corrosion resistances of the CoCrFeNi HEA in 0.1 M NaCl and in the temperature range of 25 °C–75 °C. The pits in the CoCrFeNiMn HEA were much deeper than that in the CoCrFeNi HEA, the extent of which increased with increasing temperature. This trend was attributed to the adverse effect of Mn in the matrix, lower concentration of Cr in the film, and more defective oxide film in the CoCrFeNiMn HEA, which make it easy for the film to breakdown. Similarly, Yang et al. [483] also observed that increasing the Mn content increased the susceptibility to corrosion of the CoCrFeNiMn in a 0.1 M H_2SO_4 solution as it suppressed the passivation process and increased the dissolution rate of the passive film. Sahu et al. investigated the localized corrosion behavior of a series of single phase $Ni_{38}Fe_{20}Cr_xMn_{21-0.5x}Co_{21-0.5x}$ (x = 6, 10, 14, and 22) HEAs in a 0.6 M NaCl solution. While E_{corr} was observed to be independent of Cr content, pitting resistance increased with increasing Cr content, i.e., $Ni_{38}Fe_{20}Cr_{22}Mn_{10}Co_{10}$ exhibited the highest resistance to pitting. The passivation behavior of $Ni_{38}Fe_{20}Cr_{22}Mn_{10}Co_{10}$ was further explored by Gerard et al., where the passive film was predominantly enriched in Cr with a small amount of Fe, Ni, Mn, and Co [484].

The effects of boron on the corrosion behavior of the $Al_{0.5}CoCrCuFeNiB_x$ (x = 0, 0.2, 0.6, and 1.0) HEAs in aqueous 1 N H_2SO_4 were studied by Lee et al. [472] and were compared with SS 304 steel. Increasing the boron content increased the corrosion potential and

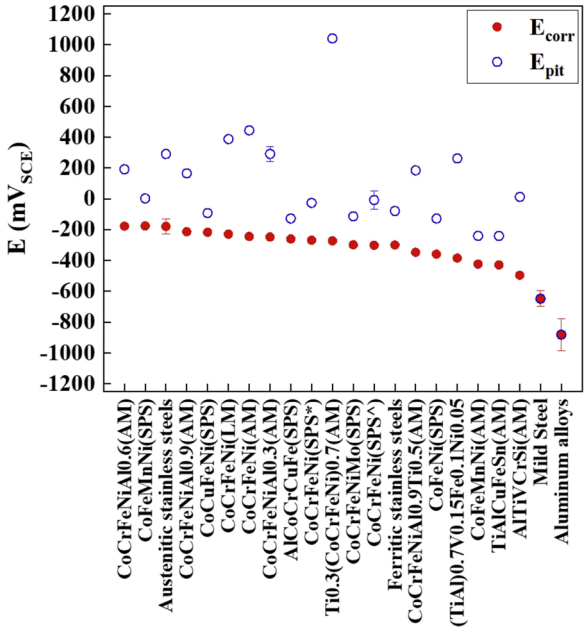

Fig. 35. Summary of corrosion potential and pitting potential for the listed HEAs in the 0.6 M NaCl solution. Adapted from [473] with permission from Taylor & Francis Ltd.

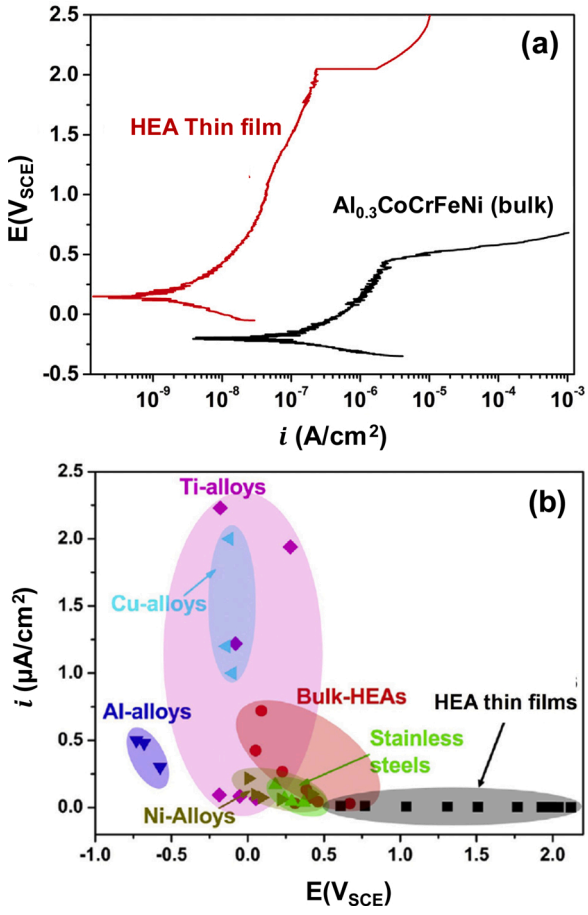

Fig. 36. (a) Potentiodynamic-polarization curves for the thin-film and bulk HEAs having approximately the same composition and (b) Comparison of the pitting potential and corrosion current among the conventional alloys, bulk and thin-film HEAs in the 3.5 wt. % NaCl solution. Adapted from [485] with permission from Elsevier.

current density from − 0.115 V_{SHE} to − 0.159 V_{SHE} and 0.787 × 10^{-6} A/cm^2 to 2.848 × 10^{-6} A/cm^2, respectively. This feature suggests that the corrosion resistance decreased with the addition of boron, which was attributed to the formation of precipitates of Cr, Fe, and Co-borides, resulting in the formation of the micro-galvanic effect and preferential corrosion of inter-dendritic regions. Nevertheless, the HEAs have better corrosion resistant than the SS 304 steel, which exhibited corrosion potential and current density of − 0.165 V_{SHE} and 3.318 × 10^{-5} A/cm^2, respectively.

Other than casting (with and without rolling), the HEAs have been also synthesized, using other methods, such as laser melting, ball milling followed by sintering, sputtering, etc. Qui et al. [473] performed potentiodynamic-polarization testing of about twenty HEAs in a 0.6 M NaCl solution. The E_{corr} and E_{pit} values of these HEAs along with steels and aluminum alloys are listed in Fig. 35. The E_{corr} values of the studied HEAs are in the range of ~ − 498 mV_{SCE} to − 180 mV_{SCE} and are higher than those of the mild steel and aluminum alloys, suggesting that the studied HEAs are much nobler than both the mild steel and aluminum alloys. E_{corr} values for several HEAs lie between ferritic stainless steels and austenitic stainless steels, whereas a couple of HEAs ($CoCrFeNiAl_{0.6}$ and CoFeMnNi) were even nobler than the austenitic stainless steels. For most of the HEAs, E_{pit} values are more positive than those of the ferritic stainless steels with some of them exhibiting even higher than the austenitic stainless steels, e.g., CoCrFeNi (LM, AM), $Ti_{0.3}(CoCrFeNi)_{0.7}$, etc. From Fig. 35, it is clear that processing methods can lead to the changes in the corrosion properties of the same HEA. For example, the E_{pit} value of the CoCrFeNi fabricated by arc melting is 442 mV_{SCE}. In contrast, the same HEA, fabricated by spark plasma sintering (SPS), exhibits lower E_{pit} values of − 28 mV_{SCE} and − 8 mV_{SCE}.

A HT synthesis of nanocrystalline $Al_x(CoCrFeNi)_{100-x}$ (x = 4.5–40 at. %) was carried out by Shi et al. [485] using a combinatorial thin-film magnetron sputtering technique, followed by the evaluation of their corrosion responses in 3.5 wt. % NaCl, using electrochemical tests. With an increase in the Al content, the microstructure changed from a single-phase FCC to single-phase BCC in the as-deposited thin films, relative to the observed transition from a single-phase FCC to multi-phase (FCC + BCC) microstructure in the bulk HEAs [461]. The polarization curves showed a decrease in both general and pitting corrosion resistances with increasing Al content, which was similar to the trend observed in the $Al_xCoCrFeNi$ bulk HEAs [461]. However, the as-deposited HEA disclosed higher corrosion resistance than the bulk HEA, as shown in the polarization curves (Fig. 36(a)) of the HEAs containing 7 at. % Al in both as-deposited and bulk conditions. Fig. 36(b) presents the comparison of corrosion parameters in the conventional alloys, thin-film HEAs, and bulk HEAs, which clearly demonstrates that the thin-films HEAs exhibit better corrosion resistance than the bulk alloys.

5. Summary of the environmental resistance properties for the HEMs

The corrosion-resistance behaviors of the HEAs have been extensively reviewed. Overall, the corrosion behavior of the HEAs predominantly depends on three factors, namely, compositions and microstructures of the alloys, type of electrolyte and processing routes (parameters). A comparison of the corrosion-resistance behaviors in the conventional alloys and HEAs (Table 10) clearly shows that the HEAs, in general, could be good candidates for corrosion-resistant alloys in aqueous media. Most of the studies on the corrosion behavior of the HEAs are limited to the transition metal family, and other families are largely still uncovered. In addition, most of the studies have been carried out in a particular environment. As the HEAs contain at least four ~ five elements (equiatomic or non-equiatomic), synthesizing all HEAs by traditional metallurgical process and then evaluating their corrosion properties are both expensive and highly time- consuming. Therefore, the ML-assisted design and HT studies are needed for the analysis of the whole domain in an optimized way. ML can analyze a vast amount of data to understand the complex inter-relation between multiple variables and their impacts on the output. Deriving insights from the existing corrosion data in the HEAs (Table 10), ML may help predict an optimized composition along with the best process conditions and parameters to synthesize a HEA for the maximum corrosion resistance through multi-dimensional optimization. It can also incorporate any potential boundary conditions, including limits to a particular elemental composition or a process parameter during the optimization process.

6. Future work

Before Jeff Bezos' Blue Origin's flight to the space on July 20th and Sir Richard Branson reached the edge of space on July 11th, Elon Musk's reusable rocket, designed and manufactured by SpaceX, has transported payloads into Earth orbit and beyond. Meanwhile, a Mars rover, Perseverance, is traveling across Mars accompanied by a robotic helicopter, Ingenuity [486]. However, the colony will depend largely on self-sufficient, even with the latest Atlas rocket it takes unmanned spacecraft around 200 days to Mars [487]. For the space missions, Ghidini has outlined the materials properties needed in engineering design [64]. With the available sun energy, additive manufacturing is the key for the on-planet manufacturing using local Mars resources, such as the regolith and the soil [488]. As a result, traveling to and building on Mars are not a quaint sci-fi concept as it used to be. Building on Mars is actual scientific possible.

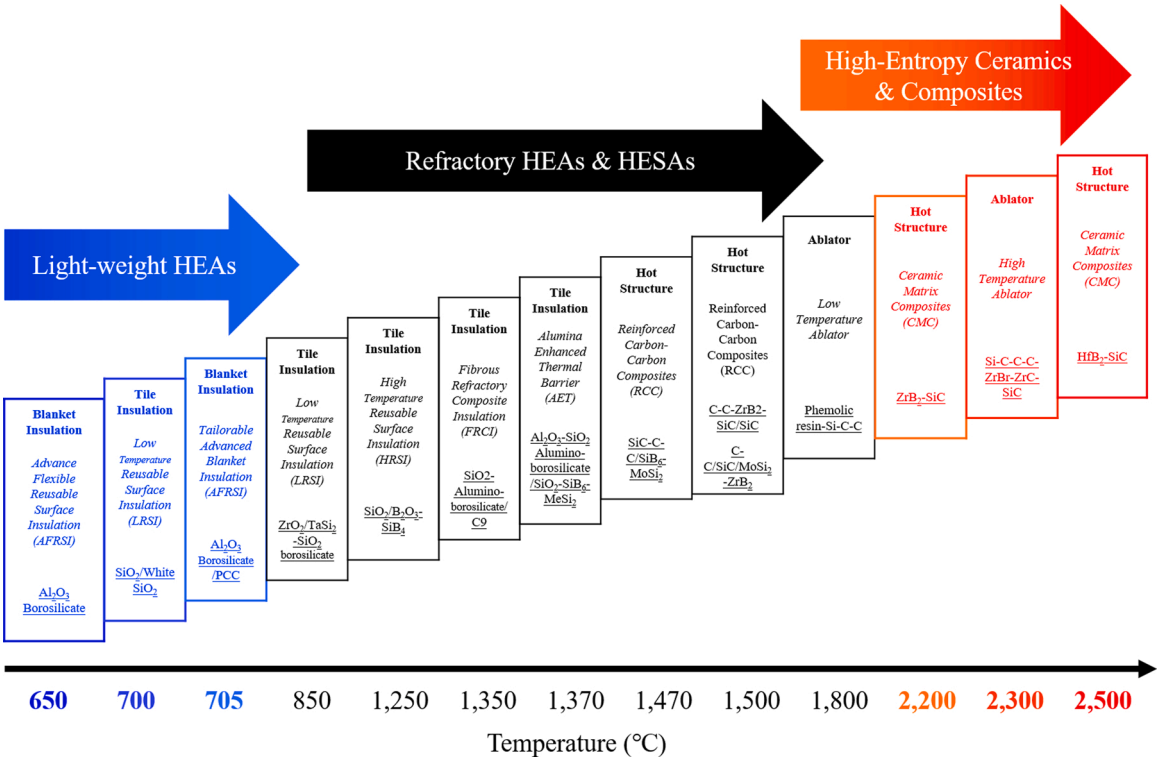

Fig. 37. The materials of different types of TPC and maximum working temperature.

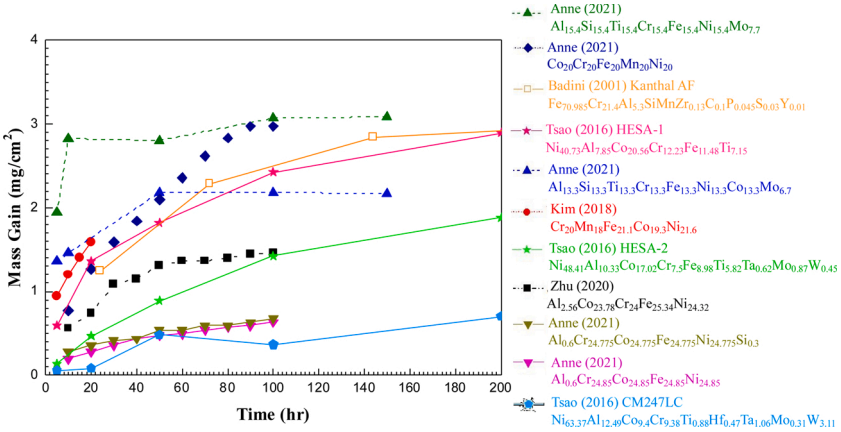

Fig. 38. The oxidation kinetics curves of different HEAs and few traditional materials during oxidation at 900 °C for 100 h and beyond (Data taken from [495, 497,504–507]).

However, choosing the best materials on Mars to build the future of humanity are yet not conclusive. Hence, the accumulated knowledge of the HEMs, which are beyond traditional metallurgy based on the Earth, will play an important role. It would also be important to apply the HT examinations to speed up the materials recognition and selections on Mars. The applications of ML are expected to optimize the fabrication procedures to adapt the manufacturing conditions on Mars. The potential applications of the HEMs for the settlements on Mars bring a fundamental change in approach because the atmospheres and the abundance of the elements are different from the Earth. It is expected to be a new paradigm shift. Although there will be unlimited new possibilities for the HEMs on Mars, in this session, only the high-temperature applications and the oxidation are selected for discussion as the future direction.

Many different materials are suitable for high-temperature applications. Some conventional materials for thermal protection system (TPC) are listed below as benchmark [489,490]. The devices of the TPC can be the blanket insulation, tile insulation, ablator, and hot structure for the rockets to Mars. These devices are listed in italics in Fig. 37. The maximum working temperature is shown in the bottom. The benchmark materials of different TPCs are displayed in underlining in Fig. 37. The potential HEMs for different temperatures ranging from medium to ultra-high temperatures are indicated in Fig. 37, which are the light-weight HEAs [491], RHEAs [423,492], High-Entropy Superalloys (HESAs) [493,494], HECs [326], and High-Entropy Composites [46].

Meanwhile, on the Earth, oxidation is critical for the metals. For example, the engines of the flight are exposed to high temperature air and when the metals are poured into a mould during the casting process [495]. Typically, the engineers consider the operating temperature range below the maximum temperature (T_{max}) at which the materials can reasonably be used without oxidation, chemical change or excessive creep. On the other hand, the capability of oxide layer can prevent

oxidation, such as the chromium oxide as the oxidation resistance layer. For the oxide dispersion strengthening, high strength at high temperatures can be obtained with fine oxide dispersions in a metal matrix, such as the fine dispersions of thoria (ThO_2).

For the HEMs, the oxidation effects on different elements within various dimensions and hierarchical microstructures are expected to be much more complicated [495–507]. Moreover, the environment of Mars is different to that of the Earth, where Mars' atmosphere is 95 % carbon dioxide (CO_2), 3 % nitrogen (N_2), 1.6 % argon (Ar); and it has traces of oxygen (O_2), carbon monoxide (CO), water (H_2O), methane (Ch_4), halogen gas (HCl), other gases, and dusts [508]. However, the experiences and the approaches on the oxidation research of the HEMs on the Earth is critical for similar perspectives to examine how would the HEMs be subjected to high-temperature fabrication and operations on Mars. Hence, in the end, some HEMs oxidation results are summarized [495, 497,504–507] in Fig. 38, which could lead the way to mimic the high-temperature research on Mars.

7. Conclusions

In this manuscript, we review "ML" and "HT examinations" for the HEAs discovery. In a HT manner, the integration of computational and experimental data becomes a crucial topic. Combinatorial experiments can validate theoretical predictions based on modeling, particularly in a wide compositional range. On the other hand, experimental data generated from the libraries can then be used to augment or optimize the theoretical models. Since the HEAs give a vast number of new alloy bases, material informatics employing statistical models, ML, computer vision, and numerical optimization provides an efficient pathway to discover new materials and even reaches the destination for extracting PSPP relationships. Up to now, there are still many challenges in data-centric approach for the HEAs: 1. Most of the studies still focus on the forward prediction model of properties with an optimization strategy to inversely discover novel compositions. The development of more efficient and advanced generative network models is a challenge and remains to be developed. 2. The database of HEMs is still limited to certain dimensions; uncertainty quantification is important for revealing the bias of prediction. 3. Most of the ML HEAs research centralize in the mechanical properties at room temperature and phases with casting process. 4. Metadata associated with physical phenomena, such as deformation mechanism, the creep mechanism, or the fatigue properties, are not generally taken into account.

Comparing the numbers of published works between "ML" and "ML + HEAs", the trends reveal that the rate of using ML on the HEMs research catches up with the applications of ML. From the reviews, there are already improved computational and ML tools for predicting multi-component phase diagrams and transport coefficients of the HEMs. There are also improved experimental and theoretical tools to study the short-range ordering effects of the HEMs. It is expected that ML can accelerate the development of cost-effective HEMs. While using ML can optimize and discover new HEMs for better performance, there are still some discrepancies to extend the ML results, such as the uncertainty and the reproducibility. Hence, complementary HT examinations for archival data to final model predictions to be validated and verified are important to establish the interpretability and trust for the ML results. As demonstrated by AFLOW, it is also important to collect and publish open reference data online. Especially, when exploring the huge composition and multi-scale spaces of the HEMs, the development and adoption of the common benchmark datasets are the key to position the new simulation and measurement results. Comparing the performance indicators will also enhance the on-the-fly examination to check the methodological progress.

As algorithms for automating the HT synthesis, characterization, and modeling will become more and more mature, the decision-making and organized experimental schemes will be the new tasks for the HEMs research using ML and HT methods. This feature means that the advances in autonomous experimental systems with AI are the key for the future. It is also necessary for the materials society to reform the higher education for this trend. Meanwhile, in the other fields, such as the International Union of Crystallography and National Institute of Standards and Technology, there are calibration standards to assess dataset and source bias through round-robin type studies to establish reproducible results. It is also important for the HEMs research community to create atmosphere in accepting the benchmarks for fusing experimental and computational data with uncertainty and applicability propagation through the model training, testing, and interpretation pipeline.

In summary, the HEMs developed with or without ML and HT methods are positioned on several property maps. We summarize the reports of corrosion research in the HEMs. Among the reviewed approaches in this manuscript, the applications of ML and HT to develop the hierarchical microstructure with the heterogeneous grain sizes are the most promising directions for better development of the HEMs.

In view of the future of the HEMs above and beyond the Earths, there are still plenty of space.

Author contribution

EWH, WJL, and SSS contributed equally to the present work and are joint first authors. EWH and PKL: Conceptualization; EWH, WJL and CYL: HT & ML data curation; SSS and PK: Corrosion data curation; TNL and HHC: HEAs data curation; BHL and TNL: Advanced photon source data curation; EWH, WJL, and SSS: Formal analysis; EWH, WJL, SSS, and PKL: Funding acquisition; EWH, WJL, and SSS: Investigation; EWH, WJL, and SSS: Methodology; EWH and PKL: Project administration; EWH, WJL, SSS, and PKL: Resources; TNL, HHC, CYL, PK and BHL: Software; EWH and PKL: Supervision; EWH and PKL: Validation; EWH, WJL, and SSS: Roles/Writing-original draft; EWH, WJL, SSS, TNL, and PKL: Writing - review & editing.

Declaration of Competing Interest

The authors declare that they have no known competing financial interests or personal relationships that could have appeared to influence the work reported in this paper.

Acknowledgements

We thank the Ministry of Science and Technology (MOST) Programs of 107-2221-E-492-011-MY3, 108-2221-E-009-131-MY4, 110-2221-E-492-012, and MOST 110-2224-E-007-001. The authors sincerely appreciate the help from the High Entropy Materials Center of the National Tsing Hua University from The Featured Areas Research Center Program within the framework of the Higher Education Sprout Project by the Ministry of Education (MOE) in Taiwan for their support. EW.H. thanks the National Synchrotron Radiation Research Center (NSRRC) for Neutron Cultivation Program, Taiwan Photon Source (TPS) Beamlines 09A, 21A, and 23A in providing the (facility/instrument/expertise) used for the HEAs research. This work was supported by the Higher Education Sprout Project of the National Yang Ming Chiao Tung University and Ministry of Education (MOE), Taiwan. P. K. L. very much appreciates the supports from (1) the National Science Foundation (DMR-1611180 and1809640) with program directors, Drs. J. Yang, G. Shiflet, and D. Farkas and (2) the US Army Research Office (W911NF-13-1-0438 and)[with program managers, Drs. M.P. Bakas, S.N. Mathaudhu, and D.M. Stepp. The authors gratefully acknowledge the use of "High-performance low temperature and multi-function X-ray diffractometer" belonging to the Core Facility Center of National Yang Ming Chiao Tung University.

References

[1] D.B. Miracle, O.N. Senkov, Acta Mater. 122 (2017) 448–511.
[2] S. Gorsse, J.-P. Couzinié, D.B. Miracle, C. R. Phys. 19 (2018) 721–736.
[3] B. Cantor, Prog. Mater. Sci. (2020), 100754.
[4] J.-W. Yeh, S.-K. Chen, S.-J. Lin, J.-Y. Gan, T.-S. Chin, T.-T. Shun, C.-H. Tsau, S.-Y. Chang, Adv. Eng. Mater. 6 (2004) 299–303.
[5] J.L. Braun, C.M. Rost, M. Lim, A. Giri, D.H. Olson, G.N. Kotsonis, G. Stan, D. W. Brenner, J.P. Maria, P.E. Hopkins, Adv. Mater. 30 (2018), 1805004.
[6] A.J. Wright, J. Luo, J. Mater. Sci. (2020) 1–16.
[7] B.L. Musicó, D. Gilbert, T.Z. Ward, K. Page, E. George, J. Yan, D. Mandrus, V. Keppens, APL Mater. 8 (2020), 040912.
[8] X. Chen, Y. Wu, J. Am. Ceram. Soc. 103 (2020) 750–756.
[9] A. Sarkar, C. Loho, L. Velasco, T. Thomas, S.S. Bhattacharya, H. Hahn, R. Djenadic, Dalton Trans. 46 (2017) 12167–12176.
[10] J. Zhang, X. Zhang, Y. Li, Q. Du, X. Liu, X. Qi, Mater. Lett. 244 (2019) 167–170.
[11] R. Djenadic, A. Sarkar, O. Clemens, C. Loho, M. Botros, V.S. Chakravadhanula, C. Kübel, S.S. Bhattacharya, A.S. Gandhi, H. Hahn, Mater. Res. Lett. 5 (2017) 102–109.
[12] X. Zhang, J. Yao, B. Liu, J. Yan, L. Lu, Y. Li, H. Gao, X. Li, Nano Lett. 18 (2018) 4247–4256.
[13] Z. Zhang, K. Song, R. Li, Q. Xue, S. Wu, D. Yan, X. Li, B. Song, B. Sarac, J.T. Kim, Materials 12 (2019) 590.
[14] R. Wei, H. Sun, C. Chen, J. Tao, F. Li, J. Magn. Magn. Mater. 449 (2018) 63–67.
[15] H. Zhang, C. Chen, Y. Fan, Y. Yang, L. Liu, R. Wei, T. Wang, W. Zhao, F. Li, J. Magn. Magn. Mater. (2020), 166875.
[16] S. Wei, F. He, C. Tasan, J. Mater. Res. (2018) 1–14.
[17] A.M. Virshup, J. Contreras-García, P. Wipf, W. Yang, D.N. Beratan, J. Am. Chem. Soc. 135 (2013) 7296–7303.
[18] J. Schmidt, M.R.G. Marques, S. Botti, M.A.L. Marques, Npj Comput. Mater. 5 (2019) 83.
[19] D. Silver, A. Huang, C.J. Maddison, A. Guez, L. Sifre, G. van den Driessche, J. Schrittwieser, I. Antonoglou, V. Panneershelvam, M. Lanctot, S. Dieleman, D. Grewe, J. Nham, N. Kalchbrenner, I. Sutskever, T. Lillicrap, M. Leach, K. Kavukcuoglu, T. Graepel, D. Hassabis, Nature 529 (2016) 484–489.
[20] M. Bojarski, D. Dworakowski Davide, B. Firner, B. Flepp, P. Goyal, M. Monfort Lawrence, U. Muller, J. Zhang, X. Zhang, J. Zhao, K. Zieba, arXiv pre-print server, 2016.
[21] A. Agrawal, A. Choudhary, APL Mater. 4 (2016), 053208.
[22] T. Lookman, P.V. Balachandran, D. Xue, R. Yuan, Npj Comput. Mater. 5 (2019) 21.
[23] T. Lookman, F.J. Alexander, A.R. Bishop, APL Mater. 4 (2016), 053501.
[24] M. Prince, J. Eng. Educ. 93 (2004) 223–231.
[25] T.D. Huan, R. Batra, J. Chapman, S. Krishnan, L. Chen, R. Ramprasad, Npj Comput. Mater. 3 (2017) 37.
[26] R. Kobayashi, D. Giofré, T. Junge, M. Ceriotti, W.A. Curtin, Phys. Rev. Mater. 1 (2017), 053604.
[27] H. Zong, G. Pilania, X. Ding, G.J. Ackland, T. Lookman, Npj Comput. Mater. 4 (2018) 48.
[28] E.V. Podryabinkin, A.V. Shapeev, Comput. Mater. Sci. 140 (2017) 171–180.
[29] K. Gubaev, E.V. Podryabinkin, G.L.W. Hart, A.V. Shapeev, Comput. Mater. Sci. 156 (2019) 148–156.
[30] J. Allison, B. Cowles, J. DeLoach, T. Pollock, G. Spanos, Implementing Integrated Computational Materials Engineering (ICME) in the Aerospace, Automotive, and Maritime Industries, Warrendale, PA 15086, 2013.
[31] J. Allison, M. Li, C. Wolverton, X. Su, JOM 58 (2006) 28–35.
[32] M. Li, J. Gazquez, A. Borisevich, R. Mishra, K.M. Flores, Intermetallics 95 (2018) 110–118.
[33] D. Miracle, B. Majumdar, K. Wertz, S. Gorsse, Scr. Mater. 127 (2016).
[34] B. Cantor, I.T.H. Chang, P. Knight, A.J.B. Vincent, Mater. Sci. Eng. A 375-377 (2004) 213–218.
[35] Y. Zhang, T.T. Zuo, Z. Tang, M.C. Gao, K.A. Dahmen, P.K. Liaw, Z.P. Lu, Prog. Mater. Sci. 61 (2014) 1–93.
[36] J.J. de Pablo, N.E. Jackson, M.A. Webb, L.-Q. Chen, J.E. Moore, D. Morgan, R. Jacobs, T. Pollock, D.G. Schlom, E.S. Toberer, J. Analytis, I. Dabo, D. M. DeLongchamp, G.A. Fiete, G.M. Grason, G. Hautier, Y. Mo, K. Rajan, E.J. Reed, E. Rodriguez, V. Stevanovic, J. Suntivich, K. Thornton, J.-C. Zhao, Npj Comput. Mater. 5 (2019) 41.
[37] K. Kaufmann, D. Maryanovsky, W.M. Mellor, C. Zhu, A.S. Rosengarten, T. J. Harrington, C. Oses, C. Toher, S. Curtarolo, K.S. Vecchio, Npj Comput. Mater. 6 (2020) 42.
[38] R. Singh, A. Sharma, P. Singh, G. Balasubramanian, D.D. Johnson, Nat. Comput. Sci. 1 (2021) 54–61.
[39] J.M. Rickman, H.M. Chan, M.P. Harmer, J.A. Smeltzer, C.J. Marvel, A. Roy, G. Balasubramanian, Nat. Commun. 10 (2019) 2618.
[40] B.D. Conduit, N.G. Jones, H.J. Stone, G.J. Conduit, Scr. Mater. 146 (2018) 82–86.
[41] B. Steingrimsson, X. Fan, X. Yang, M. C. Gao, Y. Zhang, P. K. Liaw, Predicting temperature-dependent ultimate strengths ofbody-centered-cubic (BCC) high-entropy alloys, npj Computational Materials 7 (2021), 152, https://doi.org/10.1038/s41524-021-00623-4.
[42] Baldur Andrew Steingrimsson, Peter K. Liaw, Xuesong Fan, Anand A. Kulkami, Machine Learning to Accelerate Alloy Design, United States Patent Application 20200257933 (2020).
[43] L.J. Santodonato, P.K. Liaw, R.R. Unocic, H. Bei, J.R. Morris, Nat. Commun. 9 (2018) 4520.
[44] Z. Zhou, Y. Zhou, Q. He, Z. Ding, F. Li, Y. Yang, Npj Comput. Mater. 5 (2019) 128.
[45] J. Qi, A.M. Cheung, S.J. Poon, Sci. Rep. 9 (2019) 15501.
[46] E.P. George, D. Raabe, R.O. Ritchie, Nat. Rev. Mater. 4 (2019) 515–534.
[47] Z. Pei, J. Yin, J.A. Hawk, D.E. Alman, M.C. Gao, Npj Comput. Mater. 6 (2020) 50.
[48] F.G. Coury, K.D. Clarke, C.S. Kiminami, M.J. Kaufman, A.J. Clarke, Sci. Rep. 8 (2018) 8600.
[49] P. Sarker, T. Harrington, C. Toher, C. Oses, M. Samiee, J.-P. Maria, D.W. Brenner, K.S. Vecchio, S. Curtarolo, Nat. Commun. 9 (2018) 4980.
[50] V. Tshitoyan, J. Dagdelen, L. Weston, A. Dunn, Z. Rong, O. Kononova, K. A. Persson, G. Ceder, A. Jain, Nature 571 (2019) 95–98.
[51] A. Ludwig, Npj Comput. Mater. 5 (2019) 70.
[52] J. Zhong, L. Chen, L. Zhang, Npj Comput. Mater. 7 (2021) 35.
[53] F. Oviedo, Z. Ren, S. Sun, C. Settens, Z. Liu, N.T.P. Hartono, S. Ramasamy, B. L. DeCost, S.I.P. Tian, G. Romano, A. Gilad Kusne, T. Buonassisi, Npj Comput. Mater. 5 (2019) 60.
[60] D. Hicks, C. Oses, E. Gossett, G. Gomez, R.H. Taylor, C. Toher, M.J. Mehl, O. Levy, S. Curtarolo, Acta Crystall. Sec. A 74 (2018) 184–203.
[61] B. DeCost, J. Hattrick-Simpers, Z. Trautt, A. Kusne, E. Campo, M. Green, Mach. Learn. Sci. Technol. 1 (2020).
[62] Z. Lipton, Commun. ACM 61 (2016).
[63] D. Raabe, C.C. Tasan, E.A. Olivetti, Nature 575 (2019) 64–74.
[64] T. Ghidini, Nat. Mater. 17 (2018) 846–850.
[65] B. Meredig, Chem. Mater. 31 (2019) 9579–9581.
[66] F. Häse, L.M. Roch, A. Aspuru-Guzik, Chem. Sci. 9 (2018) 7642–7655.
[67] J.P. Janet, C. Duan, T. Yang, A. Nandy, H.J. Kulik, Chem. Sci. 10 (2019) 7913–7922.
[68] J. Ling, M. Hutchinson, E. Antono, S. Paradiso, B. Meredig, Integr. Mater. Manuf. Innov. 6 (2017) 207–217.
[69] G.I. Taylor. Proceedings of the Royal Society of London. Series A, Containing Papers of a Mathematical and Physical Character 145, 1934, pp. 362–387.
[70] R. Hill, J.R. Rice, J. Mech. Phys. Solids 20 (1972) 401–413.
[71] D. Peirce, R.J. Asaro, A. Needleman, Acta Metall. 30 (1982) 1087–1119.
[72] A.S. Khan, J. Liu, J.W. Yoon, R. Nambori, Int. J. Plast. 67 (2015) 39–52.
[73] U. Ali, W. Muhammad, A. Brahme, O. Skiba, K. Inal, Int. J. Plast. 120 (2019) 205–219.
[74] D. Montes de Oca Zapiain, J.A. Stewart, R. Dingreville, Npj Comput. Mater. 7 (2021) 3.
[75] T.J. Gao, D. Zhao, T.W. Zhang, T. Jin, S.G. Ma, Z.H. Wang, J. Alloys. Compd. 845 (2020), 155911.
[76] A.R. Denton, N.W. Ashcroft, Phys. Rev. A 43 (1991) 3161–3164.
[77] E.W. Huang, D. Yu, J.-W. Yeh, C. Lee, K. An, S.-Y. Tu, Scr. Mater. 101 (2015) 32–35.
[78] G. Kim, H. Diao, C. Lee, A.T. Samaei, T. Phan, M. de Jong, K. An, D. Ma, P. K. Liaw, W. Chen, Acta Mater. 181 (2019) 124–138.
[79] A. Roy, G. Balasubramanian, Comput. Mater. Sci. 193 (2021), 110381.
[80] A. Jain, S.P. Ong, G. Hautier, W. Chen, W.D. Richards, S. Dacek, S. Cholia, D. Gunter, D. Skinner, G. Ceder, K.A. Persson, APL Mater. 1 (2013), 011002.
[81] Z. Chen, N. Andrejevic, N.C. Drucker, T. Nguyen, R.P. Xian, T. Smidt, Y. Wang, R. Ernstorfer, D.A. Tennant, M. Chan, M. Li, Chem. Phys. Rev. 2 (2021), 031301.
[82] A. Natekin, A. Knoll, Front. Neurorobot. 7 (2013).
[83] L. Breiman, Mach. Learn. 45 (2001) 5–32.
[84] C.A.F. Salvador, B.F. Zornio, C.R. Miranda, ACS Appl. Mater. Interfaces 12 (2020) 56850–56861.
[85] D.T. Ahneman, J.G. Estrada, S. Lin, S.D. Dreher, A.G. Doyle, Science 360 (2018) 186.
[86] B. Gludovatz, A. Hohenwarter, K.V.S. Thurston, H. Bei, Z. Wu, E.P. George, R. O. Ritchie, Nat. Commun. 7 (2016) 10602.
[87] Sq. Xia, Z. Wang, Tf. Yang, Y. Zhang, J. Iron Steel Res. Int. 22 (2015) 879–884. Gangtie Yanjiu Xuebao.
[88] C.-J. Tong, M.-R. Chen, J.-W. Yeh, S.-J. Lin, S.-K. Chen, T.-T. Shun, S.-Y. Chang, Metall. Mater. Trans. A 36 (2005) 1263–1271.
[89] X.F. Wang, Y. Zhang, Y. Qiao, G.L. Chen, Intermetallics 15 (2007) 357–362.
[90] C.-C. Tung, J.-W. Yeh, T.-t. Shun, S.-K. Chen, Y.-S. Huang, H.-C. Chen, Mater. Lett. 61 (2007) 1–5.
[91] J.Y. He, W.H. Liu, H. Wang, Y. Wu, X.J. Liu, T.G. Nieh, Z.P. Lu, Acta Mater. 62 (2014) 105–113.
[92] Y. LeCun, Y. Bengio, G. Hinton, Nature 521 (2015) 436–444.
[93] R.K. Vasudevan, K. Choudhary, A. Mehta, R. Smith, G. Kusne, F. Tavazza, L. Vlcek, M. Ziatdinov, S.V. Kalinin, J. Hattrick-Simpers, MRS Commun. 9 (2019) 821–838.
[94] M.K. Tripathi, R. Kumar, R. Tripathi, Mater. Today Proc. 26 (2020) 1245–1249.
[95] Q. Hu, S. Guo, J.M. Wang, Y.H. Yan, S.S. Chen, D.P. Lu, K.M. Liu, J.Z. Zou, X. R. Zeng, Sci. Rep. 7 (2017) 39917.
[96] B.S. Murty, J.W. Yeh, S. Ranganathan, Phase Selection in High-Entropy Alloys, High Entropy Alloys, Elsevier, 2014, pp. 37–56.
[97] S. Guo, C. Ng, J. Lu, C.T. Liu, J. Appl. Phys. 109 (2011), 103505.
[98] X. Yang, Y. Zhang, Mater. Chem. Phys. 132 (2012) 233–238.
[99] L. Xie, P. Brault, A.-L. Thomann, X. Yang, Y. Zhang, G. Shang, Intermetallics 68 (2016) 78–86.
[100] Z. Wang, S. Guo, C.T. Liu, JOM 66 (2014) 1966–1972.
[101] D.J.M. King, S.C. Middleburgh, A.G. McGregor, M.B. Cortie, Acta Mater. 104 (2016) 172–179.
[102] N. Qu, Y. Chen, Z. Lai, Y. Liu, J. Zhu, Procedia Manuf. 37 (2019) 299–305.
[103] C. Zhang, M.C. Gao, CALPHAD Modeling of High-Entropy Alloys, High-Entropy Alloys, Springer International Publishing, Cham, 2016, pp. 399–444.
[104] J.E. Saal, I.S. Berglund, J.T. Sebastian, P.K. Liaw, G.B. Olson, Scr. Mater. 146 (2018) 5–8.

[105] O.N. Senkov, J.D. Miller, D.B. Miracle, C. Woodward, Nat. Commun. 6 (2015) 1–10.
[106] J. Li, Q. Fang, B. Liu, Y. Liu, Y. Liu, RSC Adv. 6 (2016) 76409–76419.
[107] R. Feng, P.K. Liaw, M.C. Gao, M. Widom, Npj Comput. Mater. 3 (2017) 50.
[108] B. Yin, W.A. Curtin, Npj Comput. Mater. 5 (2019) 14.
[109] C. Niu, A.J. Zaddach, C.C. Koch, D.L. Irving, J. Alloys. Compd. 672 (2016) 510–520.
[110] B. Grabowski, Y. Ikeda, P. Srinivasan, F. Kormann, C. Freysoldt, A.I. Duff, A. Shapeev, J. Neugebauer, Npj Comput. Mater. 5 (2019) 6.
[111] Y. Ikeda, B. Grabowski, F. Körmann, Mater. Charact. 147 (2019) 464–511.
[112] F.-Z. Dai, B. Wen, Y. Sun, H. Xiang, Y. Zhou, J. Mater. Sci. Technol. 43 (2020) 168–174.
[113] F.-Z. Dai, Y. Sun, B. Wen, H. Xiang, Y. Zhou, J. Mater. Sci. Technol. 72 (2021) 8–15.
[114] D.G. Sangiovanni, F. Tasnádi, T. Harrington, M. Odén, K.S. Vecchio, I. A. Abrikosov, Mater. Des. 204 (2021), 109634.
[115] J. Xiong, S.Q. Shi, T.Y. Zhang, Mater. Des. 187 (2020).
[116] Y. Li, W.L. Guo, Phys. Rev. Mater. 3 (2019).
[117] Z.R. Pei, J.Q. Yin, J.A. Hawk, D.E. Alman, M.C. Gao, Npj Comput. Mater. 6 (2020).
[118] L. Li, B.B. Xie, Q.H. Fang, J. Li, Metall. Mater. Trans. Phys. Metall. Mater. Sci. 52 (2021) 439–448.
[119] X.G. Li, C. Chen, H. Zheng, Y.X. Zuo, S.Y.P. Ong, Npj Comput. Mater. 6 (2020).
[120] G. Kim, H.Y. Diao, C. Lee, A.T. Samaei, T. Phan, M. de Jong, K. An, D. Ma, P. K. Liaw, W. Chen, Acta Mater. 181 (2019) 124–138.
[121] C. Lee, G. Kim, Y. Chou, B.L. Musico, M.C. Gao, K. An, G. Song, Y.C. Chou, V. Keppens, W. Chen, P.K. Liaw, Sci. Adv. 6 (2020).
[122] M. Jafary-Zadeh, K.H. Khoo, R. Laskowski, P.S. Branicio, A.V. Shapeev, J. Alloys. Compd. 803 (2019) 1054–1062.
[123] A. Roy, T. Babuska, B. Krick, G. Balasubramanian, Scr. Mater. 185 (2020) 152–158.
[124] N. Filipoiu, G.A. Nemnes, Metals 10 (2020) 10.
[125] S. Uporov, S.K. Estemirova, V.A. Bykov, D.A. Zamyatin, R.E. Ryltsev, Intermetallics 122 (2020), 106802.
[126] M.C. Troparevsky, J.R. Morris, P.R.C. Kent, A.R. Lupini, G.M. Stocks, Phys. Rev. X 5 (2015), 011041.
[127] N. Islam, W. Huang, H.L. Zhuang, Comput. Mater. Sci. 150 (2018) 230–235.
[128] W. Huang, P. Martin, H.L. Zhuang, Acta Mater. 169 (2019) 225–236.
[129] Y. Li, W. Guo, Phys. Rev. Mater. 3 (2019), 095005.
[130] Y. Lederer, C. Toher, K.S. Vecchio, S. Curtarolo, Acta Mater. 159 (2018) 364–383.
[131] T. Kostiuchenko, F. Körmann, J. Neugebauer, A. Shapeev, Npj Comput. Mater. 5 (2019) 55.
[132] E. Menou, F. Tancret, I. Toda-Caraballo, G. Ramstein, P. Castany, E. Bertrand, N. Gautier, P.E.J. Rivera Díaz-Del-Castillo, Scr. Mater. 156 (2018) 120–123.
[133] S. Dixit, V. Singhal, A. Agarwal, A.K. Prasada Rao, Mater. Lett. 268 (2020), 127606.
[134] S.Y. Lee, S. Byeon, H.S. Kim, H. Jin, S. Lee, Mater. Des. 197 (2021), 109260.
[135] R. Machaka, Comput. Mater. Sci. 188 (2020) 1–15.
[136] D. Dai, T. Xu, X. Wei, G. Ding, Y. Xu, J. Zhang, H. Zhang, Comput. Mater. Sci. 175 (2020), 109618.
[137] Q. Wu, Z. Wang, X. Hu, T. Zheng, Z. Yang, F. He, J. Li, J. Wang, Acta Mater. 182 (2020) 278–286.
[138] A. Marshal, K.G. Pradeep, D. Music, L. Wang, O. Petracic, J.M. Schneider, Sci. Rep. 9 (2019) 7864.
[139] A.J. Zaddach, C. Niu, C.C. Koch, D.L. Irving, JOM 65 (2013) 1780–1789.
[140] S. Huang, W. Li, S. Lu, F. Tian, J. Shen, E. Holmström, L. Vitos, Scr. Mater. 108 (2015) 44–47.
[141] L. Patriarca, A. Ojha, H. Sehitoglu, Y.I. Chumlyakov, Scr. Mater. 112 (2016) 54–57.
[142] M. Beyramali Kivy, M. Asle Zaeem, Scr. Mater. 139 (2017) 83–86.
[143] Z. Zhang, H. Sheng, Z. Wang, B. Gludovatz, Z. Zhang, E.P. George, Q. Yu, S. X. Mao, R.O. Ritchie, Nat. Commun. 8 (2017) 14390.
[144] S. Zhao, G.M. Stocks, Y. Zhang, Acta Mater. 134 (2017) 334–345.
[145] S. Alkan, A. Ojha, H. Sehitoglu, Acta Mater. 147 (2018) 149–164.
[146] H. Huang, X. Li, Z. Dong, W. Li, S. Huang, D. Meng, X. Lai, T. Liu, S. Zhu, L. Vitos, Acta Mater. 149 (2018) 388–396.
[147] C. Niu, C.R. LaRosa, J. Miao, M.J. Mills, M. Ghazisaeidi, Nat. Commun. 9 (2018) 1363.
[148] R. Ramprasad, R. Batra, G. Pilania, A. Mannodi-Kanakkithodi, C. Kim, Npj Comput. Mater. 3 (2017) 54.
[149] K. Rajan, Annu. Rev. Mater. Res. 45 (2015) 153–169.
[150] K. Rajan, Materials Informatics, Informatics for Materials Science and Engineering, Elsevier, 2013, pp. 1–16.
[151] S. Kang, K. Cho, J. Chem. Inf. Model. 59 (2019) 43–52.
[152] H. Nguyen, S.-i. Maeda, K. Oono, Preprint at arXiv:1711.10168, 2017.
[153] R. Vasudevan, G. Pilania, P.V. Balachandran, J. Appl. Phys. 129 (2021), 070401.
[154] B.N. Janmenjoy Nayak, H.S. Behera, Int. J. Database Theory Appl. 8 (2015) 169–186.
[155] M. Seeger, Int. J. Neural Syst. 14 (2004) 69–106.
[156] N.S. Johnson, P.S. Vulimiri, A.C. To, X. Zhang, C.A. Brice, B.B. Kappes, A. P. Stebner, Addit. Manuf. 36 (2020), 101641.
[157] S. Liu, B.B. Kappes, B. Amin-ahmadi, O. Benafan, X. Zhang, A.P. Stebner, Appl. Mater. Today 22 (2021), 100898.
[158] F. Leclercq, Phys. Rev. D 98 (2018), 063511.
[159] D.E. Hilt, D.W. Seegrist, Ridge: a Computer Program for Calculating Ridge Regression Estimates, 1977.
[160] C. Shen, Y. Ding, J. Tang, F. Guo, Front. Genet. 9 (2019).
[161] N.S. Altman, Am. Stat. 46 (1992) 175–185.
[162] L. Cayton. Fast Nearest Neighbor Retrieval for Bregman Divergences, ICML' 08: Proceedings of the 25th International Conference on Machine Learning, 2008, pp. 112–119.
[163] D.M. Atallah, M. Badawy, A. El-Sayed, SN Appl. Sci. 1 (2019) 1297.
[164] L. Rokach, O. Maimon, Data Mining and Knowledge Discovery Handbook, Springer, Boston, MA, 2005.
[165] D.J.C. MacKay, Information Theory, Inference, and Learning Algorithms, Cambridge University Press, 40 W. 20 St. New York, NY; United States, 2002.
[166] L. Rabiner, B. Juang, IEEE Assp Mag. 3 (1986) 4–16.
[167] I. Goodfellow, Y. Bengio, A. Courville, Deep Learning, MIT Press, 2016, pp. 200–220. ISBN 9780262035613.
[168] J.T. Page, Z.S. Liechty, M.D. Huynh, J.A. Udall, BMC Res. Notes 7 (2014) 829.
[169] S.C. Johnson, Psychometrika 32 (1967) 241–254.
[170] S. Fujii, T. Yokoi, C.A.J. Fisher, H. Moriwake, M. Yoshiya, Nat. Commun. 11 (2020) 1854.
[171] J.M. Torralba, P. Alvaredo, A. García-Junceda, Powder Metall. 62 (2019) 84–114.
[172] C.K.I. Williams, C.E. Rasmussen, in: D.S. Touretzky, M.C. Mozer, M.E. Hasselmo (Eds.), Advances in Neural Information Processing Systems 8. Cambridge: A Bradford Book, 1996, pp. 514–520.
[173] M. Ehteshamullah, J. Math. Sci. Comput. Math. 1 (2019) 50–54.
[174] D. Basak, D. Basak, S. Pal, D. Ch, R. Patranabis, Neural Inform. Proc. Lett. Rev. (2007) 203.
[175] S.R. Safavian, D. Landgrebe, IEEE Trans. Syst. Man Cybern. 21 (1991) 660–674.
[176] V. Svetnik, A. Liaw, C. Tong, J. Christopher Culberson, R.P. Sheridan, B. P. Feuston, J. Chem. Inf. Comput. Sci. 43 (2003) 1947–1958.
[177] J.K. Pedersen, T.A.A. Batchelor, A. Bagger, J. Rossmeisl, ACS Catal. 10 (2020) 2169–2176.
[178] Y. Li, B. Holmedal, B. Liu, H. Li, L. Zhuang, J. Zhang, Q. Du, J. Xie, Calphad 72 (2021), 102231.
[179] Y.-J. Chang, C.-Y. Jui, W.-J. Lee, A.-C. Yeh, JOM 71 (2019) 3433–3442.
[180] C. Wen, Y. Zhang, C. Wang, D. Xue, Y. Bai, S. Antonov, L. Dai, T. Lookman, Y. Su, Acta Mater. 170 (2019) 109–117.
[181] Arindam Debnath, Adam M. Krajewski, Hui Sun, Shuang Lin, Marcia Ahn, Wenjie Li, Shanshank Priya, Jogender Singh, Shunli Shang, Allison M. Beese, Zi-Kui Liu, Wesley F. Reinhart, Generative deep learning as a tool for inverse designof high entropy refractory alloys, Journal of Materials Informatics 1:3 (2021), https://doi.org/10.20517/jmi.2021.05.
[182] Y. Dan, Y. Zhao, X. Li, S. Li, M. Hu, J. Hu, Npj Comput. Mater. 6 (2020) 1–7.
[183] J. Noh, J. Kim, H.S. Stein, B. Sanchez-Lengeling, J.M. Gregoire, A. Aspuru-Guzik, Y. Jung, Matter 1 (2019) 1370–1384.
[184] V.T. Witusiewicz, I. Arpshofen, H.J. Seifert, F. Sommer, F. Aldinger, J. Alloys. Compd. 305 (2000) 157–171.
[185] V. Buranich, V. Rogoz, B. Postolnyi, A. Pogrebnjak, Predicting the Properties of the Refractory High-Entropy Alloys for Additive Manufacturing-Based Fabrication and Mechatronic Applications, 2020 IEEE 10th International Conference Nanomaterials: Applications & Properties (NAP) (2020) 1–5.
[186] A. Choudhury, T. Konnur, P.P. Chattopadhyay, S. Pal, Eng. Comput. 37 (2019) 1003–1022.
[187] Y.V. Krishna, U.K. Jaiswal, R.M. R, Scr. Mater. 197 (2021), 113804.
[188] E. Menou, I. Toda-Caraballo, P.E.J. Rivera-Diaz-del-Castillo, C. Pineau, E. Bertrand, G. Ramstein, F. Tancret, Mater. Des. 143 (2018) 185–195.
[189] F. Tancret, I. Toda-Caraballo, E. Menou, P. Diaz-Del-Castillo, Mater. Des. 115 (2017) 486–497.
[190] Q.K. Zhao, H.Y. Yang, J.B. Liu, H.F. Zhou, H.T. Wang, W. Yang, Mater. Des. 197 (2021) 11.
[191] Y.J. Chang, C.Y. Jui, W.J. Lee, A.C. Yeh, Jom 71 (2019) 3433–3442.
[192] S.K. Dewangan, S. Samal, V. Kumar, J. Alloys. Compd. 823 (2020) 8.
[193] W.J. Huang, P. Martin, H.L.L. Zhuang, Acta Mater. 169 (2019) 225–236.
[194] R. Jain, S.K. Dewangan, V. Kumar, S. Samal, Mater. Sci. Eng. Struct. Mater. Prop. Microstruct. Proc. 797 (2020) 8.
[195] Z.S. Nong, H.Y. Li, J.J. Wang, Rare Met. Mater. Eng. 47 (2018) 191–196.
[196] A.A. Siddiqui, A.K. Dubey, Lasers Eng. 49 (2021) 145–154.
[197] R. Machaka, Comput. Mater. Sci. 188 (2021) 9.
[198] L. Zhang, H.M. Chen, X.M. Tao, H.G. Cai, J.N. Liu, Y.F. Ouyang, Q. Peng, Y. Du, Mater. Des. 193 (2020) 10.
[199] K. Kaufmann, K.S. Vecchio, Acta Mater. 198 (2020) 178–222.
[200] L. Lin, Mater. Perform. Charact. 4 (2015) 148–169.
[201] AFLOWLIB, 2021. http://aflowlib.org/.
[202] S. Curtarolo, W. Setyawan, S. Wang, J. Xue, K. Yang, R.H. Taylor, L.J. Nelson, G.L. W. Hart, S. Sanvito, M. Buongiorno-Nardelli, N. Mingo, O. Levy, Comput. Mater. Sci. 58 (2012) 227–235.
[203] Materials Project, Materials Project, 2021. https://materialsproject.org.
[204] E. Cyr, H. Asgari, S. Shamsdini, M. Purdy, K. Hosseinkhani, M. Mohammadi, Mater. Lett. 212 (2018) 174–177.
[205] A. Jain, S.P. Ong, G. Hautier, W. Chen, W.D. Richards, S. Dacek, S. Cholia, D. Gunter, D. Skinner, G. Ceder, K.A. Persson, Commentary: The Materials Project: A Materials Genome Approach to Accelerating Materials Innovation, APL Materials, Vol. 1, American Institute of Physics Inc., 2013, p. 011002.
[206] A. Jain, S.P. Ong, W. Chen, B. Medasani, X. Qu, M. Kocher, M. Brafman, G. Petretto, G.-M. Rignanese, G. Hautier, D. Gunter, K.A. Persson, Concurr. Comput. Pract. Exp. 27 (2015) 5037–5059.
[207] K. Mathew, J.H. Montoya, A. Faghaninia, S. Dwarakanath, M. Aykol, H. Tang, Ih. Chu, T. Smidt, B. Bocklund, M. Horton, J. Dagdelen, B. Wood, Z.K. Liu, J. Neaton, S.P. Ong, K. Persson, A. Jain, Comput. Mater. Sci. 139 (2017) 140–152.

[208] E. Huang, B. Clausen, Y. Wang, H. Choo, P. Liaw, M. Benson, L. Pike, D. Klarstrom, Int. J. Fatigue 29 (2007) 1812–1819.
[209] G. Pizzi, A. Cepellotti, R. Sabatini, N. Marzari, B. Kozinsky, Comput. Mater. Sci. 111 (2016) 218–230.
[210] L.E. Murr, S.M. Gaytan, D.A. Ramirez, E. Martinez, J. Hernandez, K.N. Amato, P. W. Shindo, F.R. Medina, R.B. Wicker, J. Mater. Sci. Technol. 28 (2012) 1–14.
[211] T. Mayeshiba, H. Wu, T. Angsten, A. Kaczmarowski, Z. Song, G. Jenness, W. Xie, D. Morgan, Comput. Mater. Sci. 126 (2017) 90–102.
[212] MAterials Simulation Toolkit (MAST) Manual — MAST 2.0.0 Documentation, MAST, 2021 (Accessed at 2021-02-10), https://pythonhosted.org/MAST.
[213] Pychemia's Documentation — Pychemia 0.1.2 Documentation, Pychemia, 2021 (Accessed at 2021-02-10), https://pythonhosted.org/pychemia.
[214] OQMD, OQMD, 2021. http://www.oqmd.org.
[215] J. Behler, M. Parrinello, Phys. Rev. Lett. 98 (2007), 146401.
[216] A.V. Shapeev, Multiscale Model. Simul. 14 (2016) 1153–1173.
[217] A.P. Thompson, L.P. Swiler, C.R. Trott, S.M. Foiles, G.J. Tucker, J. Comput. Phys. 285 (2015) 316–330.
[218] J.S. Smith, O. Isayev, A.E. Roitberg, Chem. Sci. 8 (2017) 3192–3203.
[219] A.P. Bartók, M.C. Payne, R. Kondor, G. Csányi, Phys. Rev. Lett. 104 (2010), 136403.
[220] PANDAT™ – expresslab, Pandat™, 2021. http://expresslab.co.kr/pandat.
[221] MatCalc, MatCalc, 2021. https://www.matcalc.at/start.
[222] Computational Materials Engineering | Thermo-Calc Software, ThermoCalc, 2021 (Accessed at 2021-02-10), https://thermocalc.com/.
[223] R. Otis, Z.-K. Liu, J. Open Res. Softw. 5 (2017).
[224] B. Bocklund, R. Otis, A. Egorov, A. Obaied, I. Roslyakova, Z.K. Liu, MRS Commun. 9 (2019) 618–627.
[225] N.P.Gurao Tazuddin, K. Biswas, J. Alloys. Compd. 697 (2017) 434–442.
[226] B. Zhang, M.C. Gao, Y. Zhang, S.M. Guo, Calphad 51 (2015) 193–201.
[227] M. Wu, S. Wang, H. Huang, D. Shu, B. Sun, Mater. Lett. 262 (2020), 127175.
[228] R. Schmid-Fetzer, F. Zhang, Calphad 61 (2018) 246–263.
[229] C. Zhang, X. Jiang, R. Zhang, X. Wang, H. Yin, X. Qu, Z.-K. Liu, Comput. Mater. Sci. 167 (2019) 19–24.
[230] N.Y. Yurchenko, N.D. Stepanov, A.O. Gridneva, M.V. Mishunin, G.A. Salishchev, S.V. Zherebtsov, J. Alloys. Compd. 757 (2018) 403–414.
[231] R. Feng, M. Gao, C. Lee, M. Mathes, T. Zuo, S. Chen, J. Hawk, Y. Zhang, P. Liaw, Entropy 18 (2016) 333.
[232] TCS High Entropy Alloys Database (TCHEA4), TCS High Entropy Alloys Database (TCHEA4), 2021 (Accessed at 2021/2/10), https://thermocalc.com/content/uploads/Documentation/Databases/Thermodynamic/tchea4-technical-info.pdf.
[233] PanHEA, PanHEA, 2021. https://computherm.com/docs/pandat-database-manual/molar-volume-database-manual/molar-volume-database-of-high-entropy-alloys-heas.
[234] Z.K. Liu, J. Phase Equilibria Diffus. 30 (2009) 517–534.
[235] A. van de Walle, R. Sun, Q.J. Hong, S. Kadkhodaei, Calphad 58 (2017) 70–81.
[236] Alloy Theoretic Automated Toolkit (ATAT) Home Page, ATAT, 2021 (Accessed at 2021/2/10), https://www.brown.edu/Departments/Engineering/Labs/avdw/atat.
[237] K. Kennedy, T. Stefansky, G. Davy, V.F. Zackay, E.R. Parker, J. Appl. Phys. 36 (1965) 3808–3810.
[238] F.G. Coury, P. Wilson, K.D. Clarke, M.J. Kaufman, A.J. Clarke, Acta Mater. 167 (2019) 1–11.
[239] S.A. Kube, S. Sohn, D. Uhl, A. Datye, A. Mehta, J. Schroers, Acta Mater. 166 (2019) 677–686.
[240] F. Ren, L. Ward, T. Williams, K.J. Laws, C. Wolverton, J. Hattrick-Simpers, A. Mehta, Sci. Adv. 4 (2018) eaaq1566.
[241] S.V. Kalinin, B.G. Sumpter, R.K. Archibald, Nat. Mater. 14 (2015) 973–980.
[242] E.W. Huang, H.-S. Chou, K.N. Tu, W.-S. Hung, T.-N. Lam, C.-W. Tsai, C.-Y. Chiang, B.-H. Lin, A.-C. Yeh, S.-H. Chang, Y.-J. Chang, J.-J. Yang, X.-Y. Li, C.-S. Ku, K. An, Y.-W. Chang, Y.-L. Jao, Sci. Rep. 9 (2019) 14788.
[243] HTEM, HTEM, 2021 (Accessed at 2021/2/10), https://htem.nrel.gov.
[244] The Materials Data Facility (MDF), MDF, 2021 (Accessed at 2021/2/10), https://materialsdatafacility.org.
[245] R. Chard, K.C. Z. Li, L. Ward, Y. Babuji, A. Woodard, S. Tuecke, B. Blaiszik, M.J. Franklin, I. Foster, http://arxiv.org/abs/1811.11213 (Accessed March 8, 2019) (2018).
[246] L. Himanen, A. Geurts, A.S. Foster, P. Rinke, Adv. Sci. 6 (2019), 1900808.
[247] C.K.H. Borg, C. Frey, J. Moh, T.M. Pollock, S. Gorsse, D.B. Miracle, O.N. Senkov, B. Meredig, J.E. Saal, Sci. Data 7 (2020) 6.
[248] Schrödinger | Schrödinger Is the Scientific Leader in Developing State-of-the-art Chemical Simulation Software for Use in Pharmaceutical, Biotechnology, and Materials Research, Schrödinger, 2021 (Accessed at 2021-02-10), https://www.schrodinger.com.
[249] T. Nagase, M. Todai, T. Nakano, Crystals 10 (2020) 19.
[250] T. Nagase, M. Todai, T. Nakano, Mater. Trans. 61 (2020) 567–576.
[251] T. Nagase, M. Todai, T. Nakano, Scr. Mater. 186 (2020) 242–246.
[252] Z.H. Zhang, M. Li, K. Flores, R. Mishra, J. Appl. Phys. 128 (2020) 11.
[253] Center for Hierarchical Materials Design (CHiMaD), 2021 (accessed 17 November 2021).
[254] National Renewable Energy Laboratory (NREL MatDB), 2021 (accessed 17 November 2021).
[255] NIMS Materials Database (MatNavi), 2021 (accessed 17 November 2021).
[256] Novel Material Discovery Repository (NoMaD), 2021 (accessed 17 November 2021).
[257] Computational Materials Data Network (CMD Network), 2021 (accessed 17 November 2021).
[258] Polymer genome, 2021 (accessed 17 November 2021).
[259] Matmatch, 2021 (accessed 17 November 2021).
[260] R. Li, L. Xie, W.Y. Wang, P.K. Liaw, Y. Zhang, Front. Mater. 7 (2020) 1–12.
[261] X.H. Yan, J.S. Li, W.R. Zhang, Y. Zhang, Mater. Chem. Phys. 210 (2017) 12–19.
[262] W.-M. Choi, Y.H. Jo, S.S. Sohn, S. Lee, B.-J. Lee, Npj Comput. Mater. 4 (2018) 1.
[263] D. Farkas, A. Caro, J. Mater. Res. 33 (2018) 3218–3225.
[264] Materials Data Curation System, 2021 (Accessed at 2011/2/10), https://www.nist.gov/programs-projects/materials-data-curation-system.
[265] S. Xiao, R. Hu, Z. Li, S. Attarian, K.-M. Björk, A. Lendasse, Neural Comput. Appl. 32 (2020) 14359–14373.
[266] J.-C. Zhao, Chinese Sci. Bull. 59 (2014) 1652–1661.
[267] M. Li, K.M. Flores, J. Alloys. Compd. 825 (2020), 154025.
[268] C. Haase, F. Tang, M.B. Wilms, A. Weisheit, B. Hallstedt, Mater. Sci. Eng. A 688 (2017) 180–189.
[269] M. Moorehead, K. Bertsch, M. Niezgoda, C. Parkin, M. Elbakhshwan, K. Sridharan, C. Zhang, D. Thoma, A. Couet, Mater. Des. 187 (2020), 108358.
[270] M. Moorehead, P. Nelaturu, M. Elbakhshwan, C. Parkin, C. Zhang, K. Sridharan, D.J. Thoma, A. Couet, J. Nucl. Mater. 547 (2021), 152782.
[271] Y. Xu, Y. Bu, J. Liu, H. Wang, Scr. Mater. 160 (2019) 44–47.
[272] E.W. Huang, P.K. Liaw, MRS Bull. 44 (2019) 847–853.
[273] C.-C. Yen, G.-R. Huang, Y.-C. Tan, H.-W. Yeh, D.-J. Luo, K.-T. Hsieh, E.W. Huang, J.-W. Yeh, S.-J. Lin, C.-C. Wang, C.-L. Kuo, S.-Y. Chang, Y.-C. Lo, J. Alloys. Compd. 818 (2020), 152876.
[274] K. An, VDRIVE-Data Reduction and Interactive Visualization Software for Event Mode Neutron Diffraction, 2012.
[275] W. Guo, W. Dmowski, J.-Y. Noh, P. Rack, P.K. Liaw, T. Egami, Metall. Mater. Trans. A 44 (2013) 1994–1997.
[276] Y. Wu, W.H. Liu, X.L. Wang, D. Ma, A.D. Stoica, T.G. Nieh, Z.B. He, Z.P. Lu, Appl. Phys. Lett. 104 (2014), 051910.
[277] S. Harjo, T. Ito, K. Aizawa, H. Arima, J. Abe, A. Moriai, T. Iwahashi, T. Kamiyama, Mater. Sci. Forum 681 (2011) 443–448.
[278] T.-N. Lam, Y.-S. Chou, Y.-J. Chang, T.-R. Sui, A.-C. Yeh, S. Harjo, S.Y. Lee, J. Jain, B.-H. Lai, E.-W. Huang, Crystals 9 (2019) 420.
[279] T.-N. Lam, S.Y. Lee, N.-T. Tsou, H.-S. Chou, B.-H. Lai, Y.-J. Chang, R. Feng, T. Kawasaki, S. Harjo, P.K. Liaw, Acta Mater. 201 (2020) 412–424.
[280] M. Naeem, H. He, F. Zhang, H. Huang, S. Harjo, T. Kawasaki, B. Wang, S. Lan, Z. Wu, F. Wang, Y. Wu, Z. Lu, Z. Zhang, C.T. Liu, X.-L. Wang, Sci. Adv. 6 (2020) eaax4002.
[281] M.A.M. Bourke, D.C. Dunand, E. Ustundag, Appl. Phys. A 74 (2002) s1707–s1709.
[282] J.R. Santisteban, M.R. Daymond, J.A. James, L. Edwards, J. Appl. Crystallogr. 39 (2006) 812–825.
[283] E.W. Huang, R.I. Barabash, B. Clausen, Y.-L. Liu, J.-J. Kai, G.E. Ice, K.P. Woods, P. K. Liaw, Int. J. Plast. 26 (2010) 1124–1137.
[284] E.W. Huang, R.I. Barabash, B. Clausen, P.K. Liaw, Metall. Mater. Trans. A 43 (2012) 1454–1461.
[285] E.-W. Huang, C.-K. Chang, P.K. Liaw, T.-R. Suei, Fatigue Fract. Eng. Mater. Struct. 39 (2016) 675–685.
[286] W. Woo, E.W. Huang, J.-W. Yeh, H. Choo, C. Lee, S.-Y. Tu, Intermetallics 62 (2015) 1–6.
[287] L. Wang, F. Zhang, Z. Nie, F. Wang, B. Wang, S. Zhou, Y. Xue, B. Cheng, H. Lou, X. Chen, Y. Ren, D.E. Brown, V. Prakapenka, E. Greenberg, Z. Zeng, Q.S. Zeng, Mater. Today Phys. 8 (2019) 1–9.
[288] F. Zhang, Y. Wu, H. Lou, Z. Zeng, V.B. Prakapenka, E. Greenberg, Y. Ren, J. Yan, J.S. Okasinski, X. Liu, Y. Liu, Q. Zeng, Z. Lu, Nat. Commun. 8 (2017) 15687.
[289] C.L. Tracy, S. Park, D.R. Rittman, S.J. Zinkle, H. Bei, M. Lang, R.C. Ewing, W. L. Mao, Nat. Commun. 8 (2017) 15634.
[290] E.W. Huang, C.-M. Lin, J. Jain, S.R. Shieh, C.-P. Wang, Y.-C. Chuang, Y.-F. Liao, D.-Z. Zhang, T. Huang, T.-N. Lam, W. Woo, S.Y. Lee, Mater. Today Commun. 14 (2018) 10–14.
[291] E.W. Huang, C.-M. Lin, J.-Y. Juang, Y.-J. Chang, Y.-W. Chang, C.-S. Wu, C.-W. Tsai, A.-C. Yeh, S.R. Shieh, C.-P. Wang, Y.-C. Chuang, Y.-F. Liao, D. Zhang, T. Huang, T.-N. Lam, Y.-H. Chen, J. Alloys. Compd. 792 (2019) 116–121.
[292] Y.-C. Liu, C.H. Chen, J.Y. Chen, M.-S. Chiu, P.J. Chou, C.S. Huang, S. Fann, C. C. Kuo, T.Y. Lee, C.C. Liang, G.H. Luo, H.J. Tsai, F.H. Tseng, J. Phys. Conf. Ser. 874 (2017), 012020.
[293] Y.-W. Tsai, Y.-Y. Chang, Y.-H. Wu, K.-Y. Lee, S.-L. Liu, S.-L. Chang, Opt. Express 24 (2016) 30360–30367.
[294] C.-C. Huang, T.-N. Lam, L. Amalia, K.-H. Chen, K.-Y. Yang, M.R. Muslih, S. S. Singh, P.-I. Tsai, Y.-T. Lee, J. Jain, S.Y. Lee, H.-J. Lai, W.-C. Huang, S.-Y. Chen, E.W. Huang, Sci. Rep. 11 (2021) 9610.
[295] S. Calder, K. An, R. Boehler, C.R.D. Cruz, M.D. Frontzek, M. Guthrie, B. Haberl, A. Huq, S.A.J. Kimber, J. Liu, J.J. Molaison, J. Neuefeind, K. Page, A.Md. Santos, K.M. Taddei, C. Tulk, M.G. Tucker, Rev. Sci. Instrum. 89 (2018), 092701.
[296] C. Lee, G. Kim, Y. Chou, B.L. Musicó, M.C. Gao, K. An, G. Song, Y.-C. Chou, V. Keppens, W. Chen, P.K. Liaw, Sci. Adv. 6 (2020) eaaz4748.
[297] W. Dai, H. Wang, Q. Guan, D. Li, Y. Peng, C.N. Tomé, Acta Mater. 214 (2021), 117006.
[298] Bi-Hsuan Lin, Yu-Hao Wu, Xiao-Yun Li, Hsu-Cheng Hsu, Yu-Cheng Chiu, Chien-Yu Lee, Bo-Yi Chen, Gung-Chian Yin, Shao-Chin Tseng, Shih-Hung Chang, Mau-Tsu Tang, Wen-Feng Hsieh, Capabilities of time-resolved X-ray excited optical luminescence of the Taiwan Photon Source 23A X-ray nanoprobe beamline, JOURNAL OF SYNCHROTRON RADIATION 27 (2020) 217–221, https://doi.org/10.1107/S1600577519013675.
[299] Bi-Hsuan Lin, Xiao-Yun Li, Dai-Jie Lin, Bo-Lun Jian, Hsu-Cheng Hsu, Huang-Yen Chen, Shao-Chin Tseng, Chien-Yu Lee, Bo-Yi Chen, Gung-Chian Yin, Ming-Ying Hsu, Shih-Hung Chang, Mau-Tsu Tang, Wen-Feng Hsieh, Investigation of Cavity

Enhanced XEOL of a Single ZnO Microrod by Using Multifunctional Hard X-ray Nanoprobe, Scientific Reports 7 (2019), 207, https://doi.org/10.1038/s41598-018-36764-8.
[300] TU-NGOC LAM, CHE-WEI TSAI, BO-KAI CHEN, BO-HONG LAI, HUNG-CHIH LIU, TAKURO KAWASAKI, STEFANUS HARJO, BI-HSUAN LIN, E-WEN HUANG, Element Effects of Mn and Ge on the Tuningof Mechanical Properties of High-Entropy Alloys, METALLURGICAL AND MATERIALS TRANSACTIONS A (2020), https://doi.org/10.1007/s11661-020-05932-9.
[301] M. de Jong, W. Chen, R. Notestine, K. Persson, G. Ceder, A. Jain, M. Asta, A. Gamst, Sci. Rep. 6 (2016) 34256.
[302] G. Laplanche, P. Gadaud, C. Bärsch, K. Demtröder, C. Reinhart, J. Schreuer, E. P. George, J. Alloys. Compd. 746 (2018) 244–255.
[303] G. Laplanche, P. Gadaud, O. Horst, F. Otto, G. Eggeler, E.P. George, J. Alloys. Compd. 623 (2015) 348–353.
[304] H. Ge, H. Song, J. Shen, F. Tian, Mater. Chem. Phys. 210 (2018) 320–326.
[305] F. Yang, Z. Li, Q. Wang, B. Jiang, B. Yan, P. Zhang, W. Xu, C. Dong, P.K. Liaw, Npj Comput. Mater. 6 (2020) 101.
[306] C.-T. Wu, H.-T. Chang, C.-Y. Wu, S.-W. Chen, S.-Y. Huang, M. Huang, Y.-T. Pan, P. Bradbury, J. Chou, H.-W. Yen, Mater. Today 34 (2020) 41–50.
[307] K. An, Y. Chen, A.D. Stoica, MRS Bull. 44 (2019) 878–885.
[308] B. Toby, J. Expgui, Appl. Cryst. J. 34 (2001) 210–213.
[309] K. An, H. Skorpenske, A. Stoica, D. Ma, X.-L. Wang, E. Cakmak, Metall. Mater. Trans. A 42 (2011) 95–99.
[310] S.R. Agnew, C.N. Tomé, D.W. Brown, T.M. Holden, S.C. Vogel, Scr. Mater. 48 (2003) 1003–1008.
[311] X.L. Wang, T.M. Holden, G.Q. Rennich, A.D. Stoica, P.K. Liaw, H. Choo, C. R. Hubbard, Phys. B Condens. Matter 385–386 (2006) 673–675.
[312] K. An, H.D. Skorpenske, A.D. Stoica, D. Ma, X.-L. Wang, E. Cakmak, Metall. Mater. Trans. A 42 (2011) 95–99.
[313] E.W. Huang, S.Y. Lee, H. Wang, J. Jain, P.K. Liaw, W.-C. Yang, H.-H. Chin, Y.-T. Yi, S.-Y. Tu, Mechanical Behavior of High-entropy Alloys Focusing on Tensors: an in Situ Neutron Diffraction Investigation From Room to Elevated Temperature, Reference Module in Materials Science and Materials Engineering, Elsevier, 2022, pp. 454–462.
[314] S.-m. Zheng, W.-q. Feng, S. Wang, Comput. Mater. Sci. 142 (2018) 332–337.
[315] S. Gorsse, M.H. Nguyen, O.N. Senkov, D.B. Miracle, Data Brief 21 (2018) 2664–2678.
[316] S. Gorsse, D.B. Miracle, O.N. Senkov, Acta Mater. 135 (2017) 177–187.
[317] O.N. Senkov, D.B. Miracle, K.J. Chaput, J.-P. Couzinie, J. Mater. Res. 33 (2018) 3092–3128.
[318] S. Shukla, T. Wang, M. Frank, P. Agrawal, S. Sinha, R.A. Mirshams, R.S. Mishra, Mater. Today Commun. 23 (2020), 100869.
[319] M.F. Rose, Phys. Status Solidi (b) 17 (1966) K199–K201.
[320] D.K.C. MacDonald, S.K. Roy, Phys. Rev. 97 (1955) 673–676.
[321] Y. Yang, L. Ma, G.-Y. Gan, W. Wang, B.-Y. Tang, J. Alloys. Compd. 788 (2019) 1076–1083.
[322] S. Uporov, R. Ryltsev, V. Bykov, S.K. Estemirova, D. Zamyatin, J. Alloys. Compd. 820 (2020), 153228.
[323] V. Nilsen, L.T. Pham, M. Hibbard, A. Klager, S.M. Cramer, D. Morgan, Constr. Build. Mater. 220 (2019) 587–595.
[324] S. Bishnoi, R. Ravinder, H.S. Grover, H. Kodamana, N.M.A. Krishnan, Mater. Adv. 2 (2021) 477–487.
[325] Y. Zeng, H. Cao, Q. Ouyang, Q. Qian, Mater. Today Commun. 27 (2021), 102314.
[326] C. Oses, C. Toher, S. Curtarolo, Nat. Rev. Mater. 5 (2020) 295–309.
[327] L.J. Santodonato, Y. Zhang, M. Feygenson, C.M. Parish, M.C. Gao, R.J.K. Weber, J.C. Neuefeind, Z. Tang, P.K. Liaw, Nat. Commun. 6 (2015) 5964.
[328] R.O. Simmons, R.W. Balluffi, Phys. Rev. 117 (1960) 52–61.
[329] A. Zamkovskaya, E. Maksimova, I. Nauhatsky, M. Shapoval, J. Phys. Conf. Ser. 929 (2017), 012030.
[330] G.K. Bichile, R.G. Kulkarni, J. Phys. C Solid State Phys. 8 (1975) 3988.
[331] E.W. Huang, G.-Y. Hung, S.Y. Lee, J. Jain, K.-P. Chang, J.J. Chou, W.-C. Yang, P. K. Liaw, Crystals 10 (2020).
[332] M.-X. Li, S.-F. Zhao, Z. Lu, A. Hirata, P. Wen, H.-Y. Bai, M. Chen, J. Schroers, Y. Liu, W.-H. Wang, Nature 569 (2019) 99–103.
[333] M.L. Green, I. Takeuchi, J.R. Hattrick-Simpers, J. Appl. Phys. 113 (2013), 231101.
[334] R.A. Potyrailo, I. Takeuchi, Meas. Sci. Technol. 16 (2004) 1–4.
[335] R. Potyrailo, K. Rajan, K. Stoewe, I. Takeuchi, B. Chisholm, H. Lam, ACS Comb. Sci. 13 (2011) 579–633.
[336] M.C. Gao, D.B. Miracle, D. Maurice, X. Yan, Y. Zhang, J.A. Hawk, J. Mater. Res. 33 (2018) 3138–3155.
[337] O. Gutfleisch, M.A. Willard, E. Brück, C.H. Chen, S. Sankar, J.P. Liu, Adv. Mater. 23 (2011) 821–842.
[338] V. Chaudhary, V. Soni, B. Gwalani, R.V. Ramanujan, R. Banerjee, Scr. Mater. 182 (2020) 99–103.
[339] K. Sarlar, A. Tekgül, I. Kucuk, Curr. Appl. Phys. 20 (2020) 18–22.
[340] M.J. Yao, K.G. Pradeep, C.C. Tasan, D. Raabe, Scr. Mater. 72-73 (2014) 5–8.
[341] M. Gao, D. Alman, Entropy 15 (2013) 4504–4519.
[342] Z. Song, W. Fang, J. Yan, R. Chang, S. Huang, Y. Shi, T. Zheng, H. Yu, X. Bai, B. Liu, F. Yin, Available at SSRN: https://ssrn.com/abstract=3656145 or https://doi.org/10.2139/ssrn.3656145 (2020).
[343] M.-H. Tsai, R.-C. Tsai, T. Chang, W.-F. Huang, Metals 9 (2019) 247.
[344] X. Yang, Y. Zhou, R. Zhu, S. Xi, C. He, H. Wu, Y. Gao, Acta Metall. Sin. 33 (2020) 1057–1063.
[345] Y. Lu, Y. Dong, S. Guo, L. Jiang, H. Kang, T. Wang, B. Wen, Z. Wang, J. Jie, Z. Cao, H. Ruan, T. Li, Sci. Rep. 4 (2015) 6200.
[346] Y. Lu, Y. Dong, H. Jiang, Z. Wang, Z. Cao, S. Guo, T. Wang, T. Li, P.K. Liaw, Scr. Mater. 187 (2020) 202–209.
[347] Z.H. Cao, Y.J. Ma, Y.P. Cai, G.J. Wang, X.K. Meng, Scr. Mater. 173 (2019) 149–153.
[348] R. Chen, G. Qin, H. Zheng, L. Wang, Y. Su, Y. Chiu, H. Ding, J. Guo, H. Fu, Acta Mater. 144 (2018) 129–137.
[349] Y. Ouyang, X. Zhong, Y. Du, Y. Feng, Y. He, J. Alloys. Compd. 420 (2006) 175–181.
[350] Y. Zhang, C. Wen, C. Wang, S. Antonov, D. Xue, Y. Bai, Y. Su, Acta Mater. 185 (2020) 528–539.
[351] N.C. Frey, M.K. Horton, J.M. Munro, S.M. Griffin, K.A. Persson, V.B. Shenoy, Sci. Adv. 6 (2020) eabd1076.
[352] K. Choudhary, K.F. Garrity, N.J. Ghimire, N. Anand, F. Tavazza, Phys. Rev. B 103 (2021), 155131.
[353] J. Geng, I. Nlebedim, M. Besser, E. Simsek, R. Ott, JOM 68 (2016).
[354] E.-W. Huang, G.-Y. Hung, S.Y. Lee, J. Jain, K.-P. Chang, J.J. Chou, W.-C. Yang, P. K. Liaw, Crystals 10 (2020) 200.
[355] J.M. Rickman, G. Balasubramanian, C.J. Marvel, H.M. Chan, M.T. Burton, J. Appl. Phys. 128 (2020), 221101.
[356] T. Borkar, B. Gwalani, D. Choudhuri, C. Mikler, C. Yannetta, X. Chen, R. Ramanujan, M. Styles, M. Gibson, R. Banerjee, Acta Mater. 116 (2016).
[357] L. Holleis, B.S. Shivaram, P.V. Balachandran, Appl. Phys. Lett. 114 (2019), 222404.
[358] P.Bd. Castro, K. Terashima, T.D. Yamamoto, Z. Hou, S. Iwasaki, R. Matsumoto, S. Adachi, Y. Saito, P. Song, H. Takeya, Y. Takano, NPG Asia Mater. 12 (2020) 35.
[359] Y. Zhang, X. Xu, AIP Adv. 10 (2020), 035220.
[360] A. Perrin, M. Sorescu, M.-T. Burton, D.E. Laughlin, M. McHenry, JOM 69 (2017) 2125–2129.
[361] Y. Yuan, Y. Wu, X. Tong, H. Zhang, H. Wang, X.J. Liu, L. Ma, H.L. Suo, Z.P. Lu, Acta Mater. 125 (2017) 481–489.
[362] J.Y. Law, L.M. Moreno-Ramírez, Á. Díaz-García, A. Martín-Cid, S. Kobayashi, S. Kawaguchi, T. Nakamura, V. Franco, J. Alloys. Compd. 855 (2021), 157424.
[363] J. Huo, L. Huo, J. Li, H. Men, X. Wang, A. Inoue, C. Chang, J.-Q. Wang, R.-W. Li, J. Appl. Phys. 117 (2015), 073902.
[364] W. Sheng, J.-Q. Wang, G. Wang, J. Huo, X. Wang, R.-W. Li, Intermetallics 96 (2018) 79–83.
[365] L. Luo, H. Shen, Y. Bao, H. Yin, S. Jiang, Y. Huang, S. Guo, S. Gao, D. Xing, Z. Li, J. Magn. Magn. Mater. (2020), 166856.
[366] K. Wu, C. Liu, Q. Li, J. Huo, M. Li, C. Chang, Y. Sun, J. Magn. Magn. Mater. 489 (2019), 165404.
[367] C. Pang, L. Chen, H. Xu, W. Guo, Z. Lv, J. Huo, M. Cai, B. Shen, X. Wang, C. Yuan, J. Alloys. Compd. 827 (2020), 154101.
[368] H.-P. Chou, Y.-S. Chang, S.-K. Chen, J.-W. Yeh, Mater. Sci. Eng. B 163 (2009) 184–189.
[369] R. Juneja, G. Yumnam, S. Satsangi, A.K. Singh, Chem. Mater. 31 (2019) 5145–5151.
[370] L. Chen, H. Tran, R. Batra, C. Kim, R. Ramprasad, Comput. Mater. Sci. 170 (2019), 109155.
[371] J. Carrete, W. Li, N. Mingo, S. Wang, S. Curtarolo, Phys. Rev. X 4 (2014), 011019.
[372] A. van Roekeghem, J. Carrete, C. Oses, S. Curtarolo, N. Mingo, Phys. Rev. X 6 (2016), 041061.
[373] K.T. Schütt, H. Glawe, F. Brockherde, A. Sanna, K.R. Müller, E.K.U. Gross, Phys. Rev. B 89 (2014), 205118.
[374] C. Kim, G. Pilania, R. Ramprasad, Chem. Mater. 28 (2016) 1304–1311.
[375] T. Chen, Z. Du, N. Sun, J. Wang, C. Wu, Y. Chen, O. Temam, SIGARCH Comput. Archit. News 42 (2014) 269–284.
[376] R. Islam, H. Li, P.-Y. Chen, W. Wan, H.-Y. Chen, B. Gao, H. Wu, S. Yu, K. Saraswat, H.S. Philip Wong, J. Phys. D Appl. Phys. 52 (2019), 113001.
[377] A.O. Oliynyk, E. Antono, T.D. Sparks, L. Ghadbeigi, M.W. Gaultois, B. Meredig, A. Mar, Chem. Mater. 28 (2016) 7324–7331.
[378] S. Huxtable, D.G. Cahill, V. Fauconnier, J.O. White, J.-C. Zhao, Nat. Mater. 3 (2004) 298–301.
[379] B. Li, L. Pottier, J.P. Roger, D. Fournier, K. Watari, K. Hirao, J. Eur. Ceram. Soc. 19 (1999) 1631–1639.
[380] M.-H. Tsai, Entropy 15 (2013) 5338–5345.
[381] Y.-F. Kao, S.-K. Chen, T.-J. Chen, P.-C. Chu, J.-W. Yeh, S.-J. Lin, J. Alloys. Compd. 509 (2011) 1607–1614.
[382] S. Uporov, S.K. Estemirova, V. Bykov, D. Zamyatin, R. Ryltsev, Intermetallics 122 (2020), 106802.
[383] P.C. Wei, C.N. Liao, H.J. Wu, D. Yang, J. He, G.V. Biesold-McGee, S. Liang, W. T. Yen, X. Tang, J.W. Yeh, Adv. Mater. 32 (2020), 1906457.
[384] Y. Iwasaki, I. Takeuchi, V. Stanev, A.G. Kusne, M. Ishida, A. Kirihara, K. Ihara, R. Sawada, K. Terashima, H. Someya, K.-i. Uchida, E. Saitoh, S. Yorozu, Sci. Rep. 9 (2019) 2751.
[385] L. Hu, Y. Zhang, H. Wu, J. Li, Y. Li, M. Mckenna, J. He, F. Liu, S.J. Pennycook, X. Zeng, Adv. Energy Mater. 8 (2018), 1802116.
[386] K. Han, H. Jiang, T. Huang, M. Wei, Crystals 10 (2020) 762.
[387] J. Yuan, V. Stanev, C. Gao, I. Takeuchi, K. Jin, Supercond. Sci. Technol. 32 (2019), 123001.
[388] V. Stanev, C. Oses, A.G. Kusne, E. Rodriguez, J. Paglione, S. Curtarolo, I. Takeuchi, Npj Comput. Mater. 4 (2018) 29.
[389] K. Matsumoto, T. Horide, Appl. Phys. Express 12 (2019), 073003.
[390] S. Marik, M. Varghese, K. Sajilesh, D. Singh, R. Singh, J. Alloys. Compd. 769 (2018) 1059–1063.
[391] Y. Uemura, L. Le, G. Luke, B. Sternlieb, W. Wu, J. Brewer, T. Riseman, C. Seaman, M. Maple, M. Ishikawa, Phys. Rev. Lett. 66 (1991) 2665.

[392] D.M. Gokhfeld, D.A. Balaev, M.I. Petrov, S.I. Popkov, K.A. Shaykhutdinov, V. V. Val'kov, J. Appl. Phys. 109 (2011), 033904.
[393] Y. Uemura, J. Phys. Condens. Matter 16 (2004) S4515.
[394] E.F. Talantsev, Condens. Matter 4 (2019) 83.
[395] T. Shang, J. Philippe, J.A. Verezhak, Z. Guguchia, J. Zhao, L.-J. Chang, M. Lee, D. Gawryluk, E. Pomjakushina, M. Shi, Phys. Rev. B 99 (2019), 184513.
[396] M.D. Uchic, D.M. Dimiduk, J.N. Florando, W.D. Nix, Science 305 (2004) 986–989.
[397] C. Wen, C. Wang, Y. Zhang, S. Antonov, D. Xue, T. Lookman, Y. Su, Acta Mater. 212 (2021), 116917.
[398] J. Xiong, S.Q. Shi, T.Y. Zhang, arXiv (2020).
[399] J.M. Rickman, Npj Comput. Mater. 4 (2018) 5.
[400] J.M. Rickman, G. Balasubramanian, C.J. Marvel, H.M. Chan, M.-T. Burton, J. Appl. Phys. 128 (2020), 221101.
[401] U. Bhandari, C. Zhang, C. Zeng, S. Guo, A. Adhikari, S. Yang, Crystals 11 (2021) 46.
[402] T. Zheng, X. Hu, F. He, Q. Wu, B. Han, D. Chen, J. Li, Z. Wang, J. Wang, J.-j. Kai, Z. Xia, C.T. Liu, J. Mater. Sci. Technol. 69 (2021) 156–167.
[403] J. Xiong, S.-Q. Shi, T.-Y. Zhang, J. Mater. Sci. Technol. 87 (2021) 133–142.
[404] D.N. Klimenko, N.Y. Yurchenko, N.D. Stepanov, S.V. Zherebtsov, Mater. Today Proc. 38 (2021) 1535–1540.
[405] L. Qiao, A. Bao, Z. Lai, Y. Liu, J. Zhu, Y. Wang, Mater. Sci. Eng. A 805 (2021), 140576.
[406] X.G. Li, C. Chen, H. Zheng, S.P. Ong, Npj Comput. Mater. 6 (2020) 70.
[407] L. Li, B. Xie, Q. Fang, L. Jia, Metall. Mater. Trans. A (2021).
[408] B. Gludovatz, A. Hohenwarter, D. Catoor, E.H. Chang, E.P. George, R.O. Ritchie, Science 345 (2014) 1153–1158.
[409] S.-H. Joo, H. Kato, M. Jang, J. Moon, C. Tsai, J. Yeh, H. Kim, Mater. Sci. Eng. A 689 (2017) 122–133.
[410] F. Otto, A. Dlouhý, C. Somsen, H. Bei, G. Eggeler, E.P. George, Acta Mater. 61 (2013) 5743–5755.
[411] H. Shahmir, J. He, Z. Lu, M. Kawasaki, T.G. Langdon, Mater. Sci. Eng. A 676 (2016) 294–303.
[412] S. Sun, Y. Tian, H. Lin, X. Dong, Y. Wang, Z. Zhang, Z. Zhang, Mater. Des. 133 (2017) 122–127.
[413] P. Shi, R. Li, Y. Li, Y. Wen, Y. Zhong, W. Ren, Z. Shen, T. Zheng, J. Peng, X. Liang, P. Hu, N. Min, Y. Zhang, Y. Ren, P.K. Liaw, D. Raabe, Y.-D. Wang, Science 373 (2021) 912–918.
[414] X. Gao, Y. Lu, B. Zhang, N. Liang, G. Wu, G. Sha, J. Liu, Y. Zhao, Acta Mater. 141 (2017) 59–66.
[415] Y. Dong, X. Gao, Y. Lu, T. Wang, T. Li, Mater. Lett. 169 (2016) 62–64.
[416] X. Jin, Y. Zhou, L. Zhang, X. Du, B. Li, Mater. Lett. 216 (2018) 144–146.
[417] X. Jin, J. Bi, L. Zhang, Y. Zhou, X. Du, Y. Liang, B. Li, J. Alloys. Compd. 770 (2019) 655–661.
[418] J. He, W. Liu, H. Wang, Y. Wu, X. Liu, T. Nieh, Z. Lu, Acta Mater. 62 (2014) 105–113.
[419] W. Liu, J. He, H. Huang, H. Wang, Z. Lu, C. Liu, Intermetallics 60 (2015) 1–8.
[420] L. Rogal, U. Wdowik, M. Szczerba, N. Yurchenko, T. Czeppe, P. Bobrowski, Mater. Sci. Eng. A 802 (2021), 140449.
[421] Z. Niu, Y. Xie, E. Axinte, J. Xu, Y. Wang, J. Alloys. Compd. 846 (2020), 156342.
[422] S. Zherebtsov, N. Yurchenko, E. Panina, A. Tojibaev, M. Tikhonovsky, G. Salishchev, N. Stepanov, J. Alloys. Compd. 842 (2020), 155868.
[423] S. Wei, S.J. Kim, J. Kang, Y. Zhang, Y. Zhang, T. Furuhara, E.S. Park, C.C. Tasan, Nat. Mater. 19 (2020) 1175–1181.
[424] X. Zhang, J. Huang, P. Lin, T. Liu, Y. Wu, W. Li, Y. Wang, Y. Liao, J.S. Jang, J. Alloys. Compd. 831 (2020), 154742.
[425] W. Dong, Z. Zhou, M. Zhang, Y. Ma, P. Yu, P.K. Liaw, G. Li, Metals 9 (2019) 867.
[426] P. Yu, L. Zhang, H. cheng, H. Tang, J. Fan, P.K. Liaw, G. Li, R. Liu, J. Alloys. Compd. 779 (2019) 1–6.
[427] F. Zhang, Y. Wu, H.B. Lou, Z.D. Zeng, V.B. Prakapenka, E. Greenberg, Y. Ren, J. Y. Yan, J.S. Okasinski, X.J. Liu, Y. Liu, Q.S. Zeng, Z.P. Lu, Nat. Commun. 8 (2017).
[428] P.F. Yu, L.J. Zhang, H. Cheng, H. Zhang, M.Z. Ma, Y.C. Li, G. Li, P. K.Liaw, R. P. Liu, Intermetallics 70 (2016) 82–87.
[429] K.V. Yusenko, S. Riva, W.A. Crichton, K. Spektor, E. Bykova, A. Pakhomova, A. Tudball, I. Kupenko, A. Rohrbach, S. Klemme, F. Mazzali, S. Margadonna, N. P. Lavery, S.G.R. Brown, J. Alloys. Compd. 738 (2018) 491–500.
[430] G. Li, D. Xiao, P. Yu, L. Zhang, P.K. Liaw, Y. Li, R. Liu, JOM 67 (2015) 2310–2313.
[431] A.S. Ahmad, Y. Su, S.Y. Liu, K. Ståhl, Y.D. Wu, X.D. Hui, U. Ruett, O. Gutowski, K. Glazyrin, H.P. Liermann, H. Franz, H. Wang, X.D. Wang, Q.P. Cao, D.X. Zhang, J.Z. Jiang, J. Appl. Phys. 121 (2017), 235901.
[432] F. Zhang, H. Lou, C. Songyi, X. Chen, Z. Zeng, J. Yan, W. Zhao, Y. Wu, Z. Lu, Q. S. Zeng, J. Appl. Phys. 124 (2018), 115901.
[433] Z.M. Li, K.G. Pradeep, Y. Deng, D. Raabe, C.C. Tasan, Nature 534 (2016), 227-+.
[434] Z. Wang, I. Baker, Z. Cai, S. Chen, J.D. Poplawsky, W. Guo, Acta Mater. 120 (2016) 228–239.
[435] J. Liu, C. Chen, Y. Xu, S. Wu, G. Wang, H. Wang, Y. Fang, L. Meng, Scr. Mater. 137 (2017) 9–12.
[436] B. Cai, B. Liu, S. Kabra, Y. Wang, K. Yan, P.D. Lee, Y. Liu, Acta Mater. 127 (2017) 471–480.
[437] L. Wang, J.W. Qiao, S.G. Ma, Z.M. Jiao, T.W. Zhang, G. Chen, D. Zhao, Y. Zhang, Z.H. Wang, Mater. Sci. Eng. A 727 (2018) 208–213.
[438] R. Agarwal, R. Sonkusare, S.R. Jha, N.P. Gurao, K. Biswas, N. Nayan, Mater. Des. 157 (2018) 539–550.
[439] S.F. Liu, Y. Wu, H.T. Wang, J.Y. He, J.B. Liu, C.X. Chen, X.J. Liu, H. Wang, Z.P. Lu, Intermetallics 93 (2018) 269–273.
[440] L. Jiang, Y.P. Lu, M. Song, C. Lu, K. Sun, Z.Q. Cao, T.M. Wang, F. Gao, L.M. Wang, Scr. Mater. 165 (2019) 128–133.
[441] W. Wu, L. Guo, B. Guo, Y. Liu, M. Song, Mater. Sci. Eng. A 759 (2019) 574–582.
[442] X. Gao, Y. Lu, J. Liu, J. Wang, T. Wang, Y. Zhao, Materialia 8 (2019), 100485.
[443] W. Woo, J.S. Jeong, D.K. Kim, C.M. Lee, S.H. Choi, J.Y. Suh, S.Y. Lee, S. Harjo, T. Kawasaki, Sci. Rep. 10 (2020) 1350.
[444] M. Frank, Y. Chen, S.S. Nene, S. Sinha, K. Liu, K. An, R.S. Mishra, Mater. Today Commun. 23 (2020), 100858.
[445] G. Arora, D.S. Aidhy, Metals 10 (2020) 1072.
[446] P.C. Vilalta, S. Sheikholeslami, K. Saleme Ruiz, X.C. Yee, M. Kosłowski, J. Eng. Mater. Technol. 143 (2020).
[447] D.A. Winkler, M. Breedon, P. White, A.E. Hughes, E.D. Sapper, I. Cole, Corros. Sci. 106 (2016) 229–235.
[448] P.A. White, G. Smith, T. Harvey, P.A. Corrigan, M.A. Glenn, D. Lau, S. Hardin, J. Mardel, T.A. Markley, T. Muster, Corros. Sci. 58 (2012).
[449] Z. Pei, D. Zhang, Y. Zhi, T. Yang, L. Jin, D. Fu, X. Cheng, H.A. Terryn, J.M.C. Mol, X. Li, Corros. Sci. 170 (2020), 108697.
[450] P. Liu, H. Huang, S. Antonov, C. Wen, D. Xue, H. Chen, L. Li, Q. Feng, T. Omori, Y. Su, Npj Comput. Mater. 6 (2020) 1–9.
[451] Y. Diao, L. Yan, K. Gao, Mater. Des. 198 (2021), 109326.
[452] Y. Wen, C. Cai, X. Liu, J. Pei, X. Zhu, T. Xiao, Corros. Sci. 51 (2009) 349–355.
[453] M. Kamrunnahar, M. Urquidi-Macdonald, Corros. Sci. 52 (2010) 669–677.
[454] M. Jimenez Come, I. Turias, J. Ruiz Aguilar, F. Trujillo, Mater. Corros. 66 (2015).
[455] Q. Liu, N. Li, Y. A, J. Duan, W. Yan, Energies 14 (2021) 1972.
[456] A. Malecek, UW-Madison Engineers Receive $4.8M in DOE Nuclear Research Awards, 2020. https://www.engr.wisc.edu/news/uw-madison-engineers-receive-4-1m-in-doe-nuclear-research-awards/.
[457] Y.Y. Chen, T. Duval, U.D. Hung, J.W. Yeh, H.C. Shih, Corros. Sci. 47 (2005) 2257–2279.
[458] A.A. Rodriguez, J.H. Tylczak, M.C. Gao, P.D. Jablonski, M. Detrois, M. Ziomek-Moroz, J.A. Hawk, Adv. Mater. Sci. Eng. 2018 (2018) 1–11.
[459] X.L. Shang, Z.J. Wang, Q.F. Wu, J.C. Wang, J.J. Li, J.K. Yu, Acta Metall. Sin. 32 (2019) 41–51.
[460] N. Kumar, M. Fusco, M. Komarasamy, R.S. Mishra, M. Bourham, K.L. Murty, J. Nucl. Mater. 495 (2017) 154–163.
[461] Y. Shi, B. Yang, X. Xie, J. Brechtl, K.A. Dahmen, P.K. Liaw, Corros. Sci. 119 (2017) 33–45.
[462] Y.F. Kao, T.D. Lee, S.K. Chen, Y.S. Chang, Corros. Sci. 52 (2010) 1026–1034.
[463] C.P. Lee, C.C. Chang, Y.Y. Chen, J.W. Yeh, H.C. Shih, Corros. Sci. 50 (2008) 2053–2060.
[464] Y. Shi, L. Collins, R. Feng, C. Zhang, N. Balke, P.K. Liaw, B. Yang, Corros. Sci. 133 (2018) 120–131.
[465] Y. Qiu, S. Thomas, D. Fabijanic, A.J. Barlow, H.L. Fraser, N. Birbilis, Mater. Des. 170 (2019).
[466] Y. Zhao, M. Wang, H. Cui, Y. Zhao, X. Song, Y. Zeng, X. Gao, F. Lu, C. Wang, Q. Song, J. Alloys. Compd. 805 (2019) 585–596.
[467] S. Jiang, Z. Lin, H. Xu, Y. Sun, J. Alloys. Compd. 741 (2018) 826–833.
[468] D.H. Xiao, P.F. Zhou, W.Q. Wu, H.Y. Diao, M.C. Gao, M. Song, P.K. Liaw, Mater. Des. 116 (2017) 438–447.
[469] C. Xiang, Z.M. Zhang, H.M. Fu, E. Han, H.F. Zhang, J.Q. Wang, Intermetallics 114 (2019).
[470] P. Muangtong, A. Rodchanarowan, D. Chaysuwan, N. Chanlek, R. Goodall, Corros. Sci. 172 (2020).
[471] Y.J. Hsu, W.C. Chiang, J.K. Wu, Mater. Chem. Phys. 92 (2005) 112–117.
[472] C.P. Lee, Y.Y. Chen, C.Y. Hsu, J.W. Yeh, H.C. Shih, J. Electrochem. Soc. 154 (2007) C424.
[473] Y. Qiu, M.A. Gibson, H.L. Fraser, N. Birbilis, Mater. Sci. Technol. (United Kingdom) 31 (2015) 1235–1243.
[474] J. Li, X. Yang, R. Zhu, Y. Zhang, Metals 4 (2014) 597–608.
[475] C. Dai, H. Luo, J. Li, C. Du, Z. Liu, J. Yao, Appl. Surf. Sci. 499 (2020).
[476] T.T. Shun, L.Y. Chang, M.H. Shiu, Mater. Charact. 70 (2012) 63–67.
[477] W.H. Liu, Z.P. Lu, J.Y. He, J.H. Luan, Z.J. Wang, B. Liu, Y. Liu, M.W. Chen, C. T. Liu, Acta Mater. 116 (2016) 332–342.
[478] Y. Shi, J. Mo, F.Y. Zhang, B. Yang, P.K. Liaw, Y. Zhao, J. Alloys. Compd. 844 (2020).
[479] C.M. Lin, H.L. Tsai, Intermetallics 19 (2011) 288–294.
[480] Z. Niu, J. Xu, T. Wang, N. Wang, Z. Han, Y. Wang, Intermetallics 112 (2019) 106550.
[481] H. Luo, Z. Li, A.M. Mingers, D. Raabe, Corros. Sci. 134 (2018) 131–139.
[482] H. Torbati-Sarraf, M. Shabani, P.D. Jablonski, G.J. Pataky, A. Poursaee, Mater. Des. 184 (2019) 108170.
[483] J. Yang, J. Wu, C.Y. Zhang, S.D. Zhang, B.J. Yang, W. Emori, J.Q. Wang, J. Alloys. Compd. 819 (2020).
[484] S. Sahu, O.J. Swanson, T. Li, A.Y. Gerard, J.R. Scully, G.S. Frankel, Electrochim. Acta 354 (2020), 136749.
[485] Y. Shi, B. Yang, P.D. Rack, S. Guo, P.K. Liaw, Y. Zhao, Mater. Des. 195 (2020).
[486] J. Balaram, M. Aung, M.P. Golombek, Space Sci. Rev. 217 (2021) 56.
[487] J.B.P. Filho, J. Aerosp. Technol. Manag. 13 (2021) 1–12.
[488] C. Buchner, R.H. Pawelke, T. Schlauf, A. Reissner, A. Makaya, Acta Astronaut. 143 (2018) 272–284.
[489] H.K.M. Al-Jothery, T.M.B. Albarody, P.S.M. Yusoff, M.A. Abdullah, A.R. Hussein, IOP Conference Series: Materials Science and Engineering, 863, 2020, 012003.
[490] D. Mitrica, I.C. Badea, B.A. Serban, M.T. Olaru, D. Vonica, M. Burada, R.-R. Piticescu, V.V. Popov, Materials 14 (2021) 1197.
[491] R. Feng, C. Zhang, M.C. Gao, Z. Pei, F. Zhang, Y. Chen, D. Ma, K. An, J. D. Poplawsky, L. Ouyang, Y. Ren, J.A. Hawk, M. Widom, P.K. Liaw, Nat. Commun. 12 (2021) 4329.

[492] O.N. Senkov, G.B. Wilks, D.B. Miracle, C.P. Chuang, P.K. Liaw, Intermetallics 18 (2010) 1758–1765.
[493] D.B. Miracle, M.-H. Tsai, O.N. Senkov, V. Soni, R. Banerjee, Scr. Mater. 187 (2020) 445–452.
[494] A.-C. Yeh, T.-K. Tsao, Y.-J. Chang, K.C. Chang, J.-W. Yeh, M.S. Chiou, S.-R. Jian, C.-M. Kuo, W.R. Wang, H. Murakami, J. Metall. Mater. Eng. 1 (2015).
[495] J. Zhu, S. Lu, Y. Jin, L. Xu, X. Xu, C. Yin, Y. Jia, Oxid. Met. 94 (2020) 265–281.
[496] K.-C. Lo, H. Murakami, J.-W. Yeh, A.-C. Yeh, Intermetallics 119 (2020), 106711.
[497] B.R. Anne, S. Shaik, M. Tanaka, A. Basu, SN Appl. Sci. 3 (2021) 366.
[498] S. Veselkov, O. Samoilova, N. Shaburova, E. Trofimov, Materials 14 (2021).
[499] J. Chen, X. Zhou, W. Wang, B. Liu, Y. Lv, W. Yang, D. Xu, Y. Liu, J. Alloys. Compd. 760 (2018) 15–30.
[500] W. Kai, C.C. Li, F.P. Cheng, K.P. Chu, R.T. Huang, L.W. Tsay, J.J. Kai, Corros. Sci. 121 (2017) 116–125.
[501] C.M. Liu, H.M. Wang, S.Q. Zhang, H.B. Tang, A.L. Zhang, J. Alloys. Compd. 583 (2014) 162–169.
[502] T.M. Butler, M.L. Weaver, J. Alloys. Compd. 674 (2016) 229–244.
[503] G.R. Holcomb, J. Tylczak, C. Carney, JOM 67 (2015) 2326–2339.
[504] G. Laplanche, U.F. Volkert, G. Eggeler, E.P. George, Oxid. Met. 85 (2016) 629–645.
[505] Y.-K. Kim, Y.-A. Joo, H.S. Kim, K.-A. Lee, Intermetallics 98 (2018) 45–53.
[506] T.-K. Tsao, A.-C. Yeh, C.-M. Kuo, H. Murakami, Entropy 18 (2016).
[507] C. Badini, F. Laurella, Surf. Coat. Technol. (2000).
[508] O. Korablev, K.S. Olsen, A. Trokhimovskiy, F. Lefèvre, F. Montmessin, A. A. Fedorova, M.J. Toplis, J. Alday, D.A. Belyaev, A. Patrakeev, N.I. Ignatiev, A. V. Shakun, A.V. Grigoriev, L. Baggio, I. Abdenour, G. Lacombe, Y.S. Ivanov, S. Aoki, I.R. Thomas, F. Daerden, B. Ristic, J.T. Erwin, M. Patel, G. Bellucci, J.-J. Lopez-Moreno, A.C. Vandaele, Sci. Adv. 7 (2021) eabe4386.

Further reading

[54] Y.W. Chen , J.J. Ruan , J.M. Ting , Y.H. Su , K.S. Chang . Ceram. Int. 2021; 47: 11451-11458

[55] W. Xiong , H.F. Zhang , S.Y. Cao , F. Gao , P. Svec , J. Dusza , M.J. Reece , H.X. Yan . J. Eur. Ceram. Soc. 2021; 41: 2979-2985

[56] M. Zhang , X.Z. Xu , Y.J. Yue , M. Palma , M.J. Reece , H.X. Yan . Mater. Des. 2021; 200:

[57] K.N. Zhao , X. Li , D. Su . Acta Phys.-Chim. Sin. 2021; 37:

[58] V. Soare , M. Burada , I. Constantin , D. Mitrica , V. Badilita , A. Caragea , M. Tarcolea . Appl. Surf. Sci. 2015; 358: 533-539

[59] Z.A. Kudyshev , V.M. Shalaev , A. Boltasseva . ACS Photonics 2021; 8: 34-46

E-Wen Huang is a professor in the Department of Materials Science and Engineering and achieved HEA Fellowship (FHEA) at the National Yang Ming Chiao Tung University, Taiwan. He obtained his PhD degree from the University of Tennessee. He is a recipient of the Ludo Frevel Crystallography Scholarship Award from the International Centre for Diffraction Data in 2009, Young Leaders Professional Development Award, from TMS in 2016, and Ta-You Wu Memorial Award in 2017, respectively. He is an editorial board member of *Scientific Reports*. Huang can be reached by email at ewhuang@g2.nctu.edu.tw. His research interests include the use of additive manufacturing, high entropy alloys and advanced photon source. Detailed can be found at: https://www.researchgate.net/profile/E-Wen-Huang.

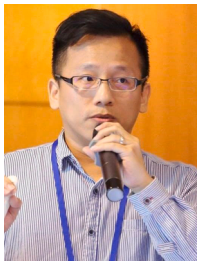

Wen-Jay Lee is a researcher in the National Center for High Performance Computing at the National Applied Research Laboratories and the joint-appointment associate professor in Department of Physics at the National Chung Hsing University, Taiwan. He received his PhD degree from the National Sun-yat sen University. His research interests includes the fundamental theory and informatics technology. His main research interests include the machine learning assisted material discovery and experimentation application, as well as computer modeling and simulation for materials, nanostructure, and semiconductor device. Lee can be reached by email at wjlee@narlabs.org.tw.

Sudhanshu Shekhar Singh is an assistant professor in the Department of Materials Science and Engineering at Indian Institute of Technology Kanpur. He obtained his PhD degree from Arizona State University. He is a recipient of NASI-Young Scientist Platinum Jubilee Awards 2020 by The National Academy of Sciences (India), 2018SMD JOM Best Paper Award by The Minerals, Metals & Materials Society (TMS), Young Metallurgist of the Year Award 2017 by Ministry of Steel & Mines (India) and IEI Young Engineers Award 2017–2018 by The Institution of Engineers (India).

Poresh Kumar is a PhD student in the Department of Materials Science and Engineering at Indian Institute of Technology Kanpur. He received his M. Tech degree in the Department of Metallurgy and Materials Engineering from Indian Institute of Engineering Science and Technology Shibpur. His research interests include high entropy alloys and additive manufacturing.

Chih-Yu Lee is a research assistant in National Center for High-performance Computing under Dr. Wen-Jay Lee's supervision. She obtained her Bachelor degree in Materials Science and Engineering from National Tsing Hua University. Her research interest is developing novel combinatorial approaches and applied them in materials design and discovery. She has focused in several areas such as high entropy alloys and semiconductors. As Lee is starting her PhD in University of Maryland, she can be reached by email at cylee01@umd.edu.

Tu-Ngoc Lam achieved her PhD degree in 2015 at the National Chiao Tung University in Taiwan. At present, she is a postdoctoral researcher at the Department of Materials Science and Engineering of the National Yang Ming Chiao Tung University, Taiwan. Her research focuses on the characterization and analysis of a wide variety of materials, such as metals and alloys, polymers, and semiconductors by employing synchrotron-based techniques. Detailed can be found at: https://www.researchgate.net/profile/Tu-Ngoc-Lam.

Hsu-Hsuan Chin is the first-year Master student of the department of Materials Science And Engineering at the National Yang Ming Chiao Tung University, Taiwan. He graduated from the Undergraduate Honors Program of Nano Science and Engineering, National Yang Ming Chiao Tung University Chin can be reached by email at ryan3169.pn05@nctu.edu.tw.

Bi-Hsuan Lin is an associate research scientist in the Experimental Facility Division at the National Synchrotron Radiation Research Center, Taiwan. He obtained his PhD degree from the National Yang Ming Chiao Tung University. He is scientist in charge at the Taiwan Photon Source (TPS) 23A X-ray nanoprobe (XNP) beamline. Lin can be reached by email at bihsuan@nsrrc.org.tw.

Peter K. Liaw obtained his B.S. in Physics from the National Tsing Hua University, Taiwan, and his Ph.D. in Materials Science and Engineering from Northwestern University in 1980. After working at the Westinghouse Research and Development (R&D) Center for thirteen years, he joined the faculty and became an Endowed Ivan Racheff Chair of Excellence in the Department of Materials Science and Engineering at The University of Tennessee (UT), Knoxville in March 1993. He has worked in the areas of fatigue, fracture, nondestructive evaluation, and life-prediction methodologies of structural alloys and composites. Since joining UT, his research interests include mechanical behavior, neutron and synchrotron diffraction, bulk-metallic glasses, high-entropy alloys, and processing of high-temperature alloys and ceramic-matrix composites and coatings, with the kind help of his team members and colleagues at UT and Oak Ridge National Laboratory, and throughout the world. He has published over one thousand journal papers, edited and written fifty seven books and book chapters, and presented numerous plenary, keynote, and invited talks at various national and international conferences. He was awarded the Royal E. Cabell Fellowship at Northwestern University. He is the recipient of numerous "Outstanding Performance" awards from the Westinghouse R&D Center. He was the Chairman of The Minerals, Metals and Materials Society (TMS) "Mechanical Metallurgy" Committee, and Chairman of the American Society for Metals (ASM) "Flow and Fracture" Committee. He has been the Chairman and Member of the TMS Award Committee on "Application to Practice, Educator, and Leadership Awards." He is a fellow of ASM and TMS. He has been given the Outstanding Teacher Award, the Moses E. and Mayme Brooks Distinguished Professor Award, the Engineering Research Fellow Awards, the National Alumni Association Distinguished Service Professor Award, the L. R. Hesler Award, and the John Fisher Professorship at UT, the TMS Distinguished Service Award, and a 2020 TMS Symposium dedicated to him. He has been the Director of the National Science Foundation (NSF) Integrative Graduate Education and Research Training (IGERT) Program, the Director of the NSF International Materials Institutes (IMI) Program, and the Director of the NSF Major Research Instrumentation (MRI) Program at UT. Several of his graduate students have been given awards for their research, papers, and presentations at various professional societies and conferences. Moreover, his students teach and conduct research at universities, industries, and government laboratories.